Nonlinear flexural-gravity free-surface flows and related gravity-capillary flows

by

Tao Gao MSc

A thesis submitted in conformity with the requirements

for the degree of Doctor of Philosophy

Department of Mathematics

Faculty of Mathematical & Physical Sciences

University College London

June, 2016

Disclaimer

I, Tao Gao, confirm that the work presented in this thesis is my own. Where information has been derived from other sources, I confirm that this has been indicated in the thesis.

Signature _____

Date _____

Abstract

The thesis is mainly concerned with linear and nonlinear water waves travelling beneath an elastic sheet. Such waves are known as flexural-gravity waves. The basic mathematical formulation is introduced in Chapter 2. Several numerical methods are presented in Chapter 3. Related problems involving gravity-capillary waves are also considered. Nonlinear periodic waves are studied in Chapter 4 by analytical and numerical methods. The extension to generalised solitary waves is also presented in that chapter. The problem of two-dimensional flexural-gravity waves generated by a moving disturbance is considered in Chapter 5. Solitary waves in deep water are computed in Chapter 6. A new kind of asymmetric solitary waves is presented. We carry out a numerical study of the dynamics and the stability of the free-surface flows in Chapter 7. The problem of gravity-capillary waves is revisited in Section 4.5 and Chapter 8 and new non-symmetric periodic waves are discovered.

This thesis was completed under the supervision of **Professor Jean-Marc Vanden-Broeck**.

Acknowledgments

Firstly I would like to thank Professor Jean-Marc Vanden-Broeck for his fantastic supervision.

Secondly I would like to thank Professor Zhan Wang for his brilliant academic help.

Thirdly I would like to thank all the supporting staff at the Department of Mathematics, UCL.

Finally I would like to thank my parents for their continuous support.

<div align="right">Tao Gao, University College London, June 2016</div>

To my beloved wife Junlei, and Yuki and Penny.

The genius of Laplace was a perfect sledge hammer in bursting purely mathematical obstacles; but, like that useful instrument, it gave neither finish nor beauty to the results. In truth, in truism if the reader please, Laplace was neither Lagrange nor Euler, as every student is made to feel. The second is power and symmetry, the third power and simplicity; the first is power without either symmetry or simplicity. But, nevertheless, Laplace never attempted investigation of a subject without leaving upon it the marks of difficulties conquered: sometimes clumsily, sometimes indirectly, always without minuteness of design or arrangement of detail; but still, his end is obtained and the difficulty is conquered.

—Augustus De Morgan

Contents

List of Tables

List of Figures

Chapter 1

Introduction

Hydroelasticity, a name adapted from aeroelasticity, is concerned with the motion and distortion of deformable bodies responding to hydrodynamic excitations, and the associated reactions on the motion of the environmental fluid. Hydroelastic waves enjoy wide usages in marine structures and sea transport. Modern applications of hydroelastic waves abound: very large floating structures usable as fully functional airport runways (Megafloat project in Japan); large fast merchant ships and container vessels which are relatively more flexible (see [52]); flexible risers to transport hydrocarbon (mainly refers to oil) from the seabed to shore or offshore facilities (see [23]); safe use of lake and ocean ice for roadways and landing strips (see [42, 44, 55]). Due to these physical and industrial significance, in-depth knowledge of the characteristics of hydroelastic waves is therefore important.

The present work considers the irrotational motion of a two-dimensional inviscid and incompressible fluid, with the top surface being in contact with a frictionless thin elastic sheet. Since there are two restoring forces across the free surface (the gravity and the flexural rigidity due to the elastic bending) the hydroelastic waves propagating through the elastic cover are also called flexural-gravity (F-G) waves in the literature. This problem has been proposed as an ideal model for the dynamics of a large body of waves covered by a floating ice sheet in polar regions, and has been

studied extensively mostly in the linear setting since the pioneering work by [17] (the reader is referred to the monograph by [41] which describes in detail the research based on the linear theory prior to 1996).

The linear theory is a good approximation when the deformations of the elastic cover are relatively small, but becomes unreliable as the amplitude of the waves grows (the reader is referred to the reports of intense-in-ice events by [28] which highlight the limitations of the linear theory). In particular, the linear theory fails for the problem of a concentrated line load moving steadily over an ice sheet floating on a fluid when the velocity of the load is at the minimum of the phase speed (denoted by $c_{\min}$). In order to resolve this problem, [34] examined the nonlinear effects as the speed of the load is close to the critical value $c_{\min}$. They conducted a normal form analysis which leads to a forced nonlinear Schödinger equation (NLS) with the mean depth of the fluid being a parameter. Their results show that for a large enough water depth, bounded responses in the form of hydroelastic solitary waves can exist for speeds up to $c_{\min}$, while there is a range of forcing speed below $c_{\min}$ for which there are no steady solutions when the fluid is relatively shallow. Direct numerical simulations for the unsteady problem using truncated models together with high-order spectral method were carried out by [2]. They confirmed the predictions of [34] in the appropriate regime. [30] revisited the same fully nonlinear problem and successfully computed the hydroelastic solitary waves in deep water in the absence of moving loads, even though the weakly nonlinear analysis shows that the associated cubic NLS is of defocussing type at the minimum of the phase speed. However these solitary waves are unusual, since they can only exist with finite amplitudes. In other words, they bifurcate neither from infinitesimal periodic waves like the gravity-capillary solitary waves in deep water (see, e.g., [49, 53]), nor from infinitesimal long waves like the sech-square solitons of the Korteweg-de Vries (KdV) equation. Furthermore, the unsteady simulations in the same paper reveal

that these solitary waves may arise naturally from the moving load problem subject to the moderate-amplitude near-critical forcing. This fact indicates that the existence and the stability of free solitary waves are crucial to the forced problem.

All the results mentioned in the last paragraph are based on the Kirchhoff-Love model which uses $\partial_{xx}\kappa$ to formulate the pressure exerted by the bending of the elastic sheet, where κ is the curvature of the surface and x is the coordinate in the direction of the wave propagation. The Kirchhoff-Love elastic model has also been used on other occasions in the absence of moving loads, which include, but are not limited to, the studies of periodic hydroelastic waves (see [11,12]), the computations of generalised solitary waves in flexural-gravity waves (see [51]) and the unsteady interaction between a fluid-loaded elastic plate and a mean flow (see [35]). Although the Kirchhoff-Love model is widely used in the literature it has some limitations. In particular, it does not appear to have an elastic potential. More recently, Toland [45, 46] proposed a novel nonlinear elastic model using the Cosserat theory of hyperelastic shells satisfying Kirchhoff's hypotheses, which has a clear variational structure. From then on, the analytical and numerical investigations of this new model have been gradually carried out. Of note is the work of [46] who rigorously proved the existence of periodic hydroelastic waves, [18] who discovered both elevation and depression branches which exist below the minimum of phase speed at finite amplitude in deep water, [54] who extended elevation solitary waves to the highly nonlinear regime with the wave profiles featuring multi-packet structure and computed the periodic waves with overhanging structure as well, [13] who investigated the generalised solitary waves extensively, and [33] who considered nonlinear hydroelastic hydraulic falls past a submerged bottom obstruction.

The Plotnikov-Toland model will be used intensively in this thesis. It will enable us to discover new types of waves and to perform careful studies of fully nonlinear waves.

There are relatively few studies on unsteady hydroelastic waves based on Plotnikov-Toland model. It is worth mentioning that Guyenne & Părău performed direct numerical simulations for unsteady hydroelastic solitary waves in deep water (see [18]) and shallow water (see [19]) scenarios, and compared the results with those predicted by the forced NLS and the fifth-order KdV equation respectively. Their numerics were based on reduced models with the truncated Dirichlet-Neumann operator which cannot be used to study highly nonlinear waves, such as overhanging waves. To our knowledge, there have been no computations of the dynamics of hydroelastic solitary waves using the full Euler equations based on Plotnikov-Toland model. This is achieved in this work.

On the experimental side, a number of early measurements including the waves resulting from constant-moving load, aircraft take-offs and aircraft landings were reported by [55]. More refined experiments were carried out in 1980s by [44] in Lake Saroma corresponding to the shallow water case and by [42] at McMurdofor for deep water. Typical physical parameters for ice in two cases are respectively: 17 cm thick sheet over water 6.8 m deep in Lake Saroma, Hokkaido, giving a minimal-speed wavelength of approximately 20 m; and 1.6 m sheet over water 350 m deep at McMurdo Sound, giving a typical wavelength of approximately 160 m.

The thesis is structured as the following. In Chapter 2, a detailed mathematical formulation to the problem is introduced. The linear theory is developed. In Chapter 3, we present several different numerical schemes which are to be used for solving the nonlinear steady solutions and also the time-dependent solutions. In Chapter 4, we restrict our attention to periodic waves. Their extension to the generalised solitary waves is considered. In Chapter 5, we work on the problem of surface waves generated due to a moving disturbance by using the linear theory and the nonlinear theory. In Chapter 6, the symmetric solitary waves in deep water are investigated by using two different numerical schemes. A comparsion of the results is given.

A new kind of non-symmetric solitary waves is discovered. The whole bifurcation diagram is then worked out. In Chapter 7, we study the problem of the dynamics and of the stability of the waves. Numerical experiments of collisions and excitations are carried out. These results suggest new physical experiments in laboratory. In Chapter 8, the problem of non-symmetric gravity-capillary waves is revisited by using the numerical method presented in Section 3.1. In Appendix B, a full derivation of the time-dependent numerical scheme is provided. Some of the results presented in this thesis have already been written in the form of papers (see references [13–16]).

Chapter 2

Mathematical Formulation

2.1   Equations of motion

We assume an incompressible and inviscid fluid. In the presence of gravity, the Euler's equations are written by

$$\frac{D\mathbf{u}}{Dt} = -\frac{1}{\rho}\nabla p + \mathbf{g}. \tag{2.1}$$

where $\mathbf{g}$ is the acceleration due to gravity, p is the pressure, $\mathbf{u}$ is the fluid velocity and $\frac{D\mathbf{u}}{Dt} = \frac{\partial \mathbf{u}}{\partial t} + \mathbf{u}\nabla.\mathbf{u}$ is the material derivative of $\mathbf{u}$. By further assuming that the fluid is irrotational, we integrate the Euler's equations to get Bernoulli equation

$$\frac{\partial \phi}{\partial t} + \frac{p}{\rho} + \frac{1}{2}\mathbf{u}^2 + \Omega = B, \tag{2.2}$$

where B is the Bernoulli constant and Ω is a potential of the gravitational force field. In the next section, we formulate the problem in two dimension.
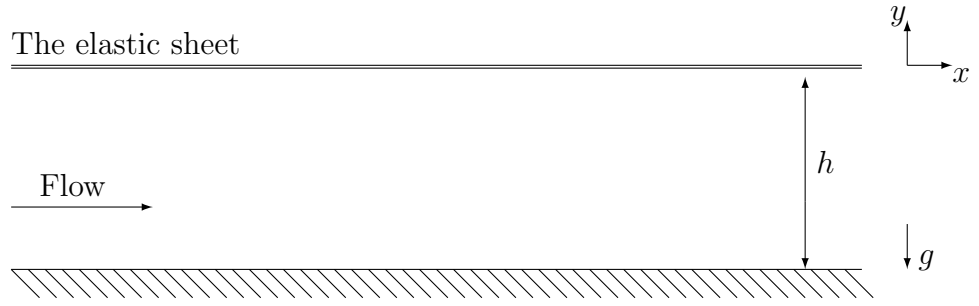
Figure 2.1: The two-dimensional problem of waves beneath an elastic sheet.
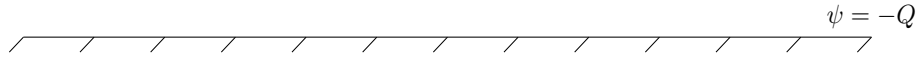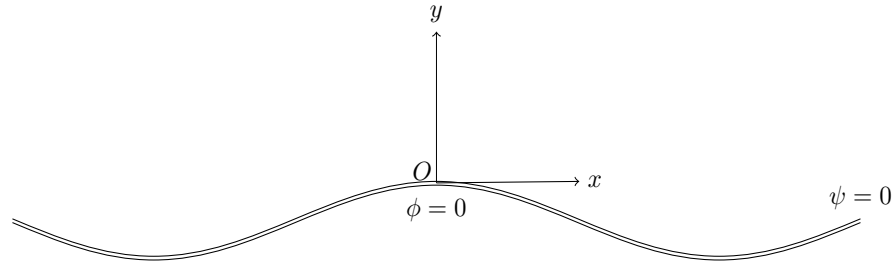
Figure 2.2: The mathematical configuration of the problem.

2.2 Two-dimensional problem

We consider a two-dimensional irrotational flow of an inviscid and incompressible fluid with constant depth h covered by an elastic layer (see Figure 2.1). The surface is deformed by a train of waves travelling with a constant velocity c. A two-dimensional cartesian system with the y-axis pointing upwards is introduced. Gravity follows the negative y-direction. We denote by $y = \eta(x,t)$ the equation of the unknown free-surface. The level of the bottom is set to be $y = -h$. A frame of reference moving with the waves is chosen so that the flow is steady.

We introduce the potential function ϕ and the streamfunction ψ. $\psi = 0$ is chosen

on the surface and $\phi = 0$ at the crest where $x = 0$. We denote by $-Q$ the value of the streamfunction ψ on the bottom. The configuration is shown in Figure 2.2. The governing equations are

$$\nabla^2 \phi = 0, \qquad\qquad -h < y < \eta(x), \qquad\qquad (2.3)$$

$$\phi_y = \phi_x \eta_x, \qquad\qquad \text{on } y = \eta(x), \qquad\qquad (2.4)$$

$$\frac{1}{2}(\phi_x^2 + \phi_y^2) + gy + \frac{p}{\rho} = B, \qquad\qquad \text{on } y = \eta(x), \qquad\qquad (2.5)$$

$$\phi_y = 0, \qquad\qquad \text{on } y = -h, \qquad\qquad (2.6)$$

Equation (2.4) and (2.6) are the kinematic boundary conditions on the free-surface and at the bottom respectively. Equation (2.5) is the Bernoulli equation on the free-surface or, in other words, the dynamic boundary condition in which p is the pressure exerted by the elastic sheet. We shall present three different models for the pressure term.

We look for periodic waves by imposing conditions

$$\nabla \phi(x + \lambda, y) = \nabla \phi(x, y), \qquad\qquad (2.7)$$

$$\eta(x + \lambda) = \eta(x). \qquad\qquad (2.8)$$

where λ is the wavelength. The average level of the surface is chosen to be zero, i.e.

$$\int_0^\lambda \eta(x)dx = 0. \qquad\qquad (2.9)$$

The phase velocity equals c is defined by

$$\frac{1}{\lambda} \int_0^\lambda \phi_x(x, y_0)dx = c, \qquad\qquad (2.10)$$

where y_0 is a constant. In the first part of the work we assume that the waves are

symmetric, i.e.

$$\eta(-x) = \eta(x), \tag{2.11}$$

$$\phi(-x, y) = -\phi(x, y). \tag{2.12}$$

Non-symmetric waves will be considered in Chapter 8.

The curvature of a graph is defined by

$$\kappa = \frac{\partial \theta}{\partial s}, \tag{2.13}$$

where s is the arclength and θ is the angle between the tangent to the curve and the horizontal axis. The free surface is described as $y = \eta(x)$. By using the chain rule, (2.13) turns out to be

$$\kappa = \frac{\partial \theta}{\partial x} \frac{\partial x}{\partial s} = \frac{\theta_x}{\sqrt{1 + \eta_x^2}}. \tag{2.14}$$

By definition, we have

$$\tan \theta = \eta_x. \tag{2.15}$$

Hence the derivative of θ with respect to x can be easily found to be

$$\theta_x = \frac{\eta_{xx}}{1 + \eta_x^2}. \tag{2.16}$$

Combining (2.14) and (2.16), we have an expression for the curvature

$$\kappa = \frac{\eta_{xx}}{(1 + \eta_x^2)^{\frac{3}{2}}}. \tag{2.17}$$

We now list the various models that we shall use to model the plate.

Kirchhoff-Love model

$$p = D\kappa_{xx}, \tag{2.18}$$

where D is the flexural rigidity defined as

$$D = Eh^3/12(1 - \nu^2) \tag{2.19}$$

with E the Young's modulus, ν the Poisson ration and h the thickness of ice. κ_{xx} is the second derivative of the curvature with respect to x. This simplified model was first presented in [11] and [12] for large amplitude waves under an elastic sheet.

Plotnikov-Toland model

$$p = D(\kappa_{ss} + \frac{1}{2}\kappa^3), \tag{2.20}$$

where s is the arclength. This nonlinear model is usually preferable to the previous one since it consists of purely geometric terms and conserves the elastic potential energy. It is a new nonlinear elastic sheet model recently introduced by [36] by using the special Cosserat theory of hyperelatic shells with Kirchhoff's hypotheses and irrotational flow theory. By using the chain rule, it can be written as

$$p = D\Big[\frac{1}{\sqrt{1 + \eta_x^2}}\partial_x\big(\frac{1}{\sqrt{1 + \eta_x^2}}\partial_x\kappa\big) + \frac{1}{2}\kappa^3\Big]. \tag{2.21}$$

Linear model

$$p = D\eta_{xxxx}. \tag{2.22}$$

This is the simplest linear model which can be obtained by linearising the Kirchhoff-Love model or the Plotnikov-Toland model.

Related gravity-capillary problem

For gravity-capillary problem, p is the pressure due to surface tension, which can be written

$$p = -T\kappa, \tag{2.23}$$

where T is the surface tension.

In the next section, we will get a first insight in the flexural-gravity waves by using linear theory and (2.22).

2.3 Linear waves

We first note that there is a trivial solution of the system (2.3)-(2.6), which is the uniform flow travelling with a constant velocity c,

$$\eta(x) = 0, \ \ \phi = cx, \ \ B = \frac{1}{2}c^2. \tag{2.24}$$

Now we add a small perturbation to this exact solution,

$$\phi(x, y) = cx + \varphi(x, y), \tag{2.25}$$

$$\eta(x) = 0 + \widetilde{\eta}(x, y), \tag{2.26}$$

with $|\varphi(x, y)|$ and $|\widetilde{\eta}(x, y)|$ being very small. Substituting (2.25) and (2.26) into the system (2.3)-(2.6) and eliminating the nonlinear terms, we obtain

$$\nabla^2 \varphi = 0, \qquad\qquad -h < y < 0, \qquad (2.27)$$

$$\varphi_y = c\widetilde{\eta}_x, \qquad\qquad y = 0, \qquad (2.28)$$

$$c\varphi_x + g\widetilde{\eta} + \frac{D}{\rho}\widetilde{\eta}_{xxxx} = 0, \qquad\qquad y = 0, \qquad (2.29)$$

$$\varphi_y = 0, \qquad\qquad y = -h. \qquad (2.30)$$

The periodic conditions (2.7), (2.8) become

$$\varphi(x + \lambda, y) = \varphi(x, y), \qquad (2.31)$$

$$\widetilde{\eta}(x + \lambda, y) = \widetilde{\eta}(x, y). \qquad (2.32)$$

We solve the Laplace equation (2.27) by separating variables

$$\varphi(x, y) = F(x)G(y). \qquad (2.33)$$

Then it gives

$$\frac{F''(x)}{F(x)} = -\frac{G''(y)}{G(y)} = -\alpha^2, \qquad (2.34)$$

where α is a constant. We choose a minus sign in front of α^2 so that $F(x)$ is a periodic function. The boundary condition from (2.30) becomes

$$G'(-h) = 0. \qquad (2.35)$$

We obtain first solutions for $F(x)$ and $G(y)$ which can be written as

$$F(x) = \sin \alpha x, \qquad (2.36)$$

$$G(y) = \cosh \alpha(y + h). \qquad (2.37)$$

Here we have used the symmetry condition (2.12). The periodic condition (2.31) gives $\alpha\lambda = 2n\pi$ for $n \in \mathbb{N}$ or

$$\alpha = nk, \tag{2.38}$$

where k is the wavenumber. We can get different solutions for different n. A linear combination of the solutions is still a solution due to the linearity of the system. Hence the general solution can be written as

$$\varphi(x,y) = \sum_{n=1}^{\infty} B_n \sin(nkx) \cosh nk(y+h), \tag{2.39}$$

where B_n are constants.

As $\widetilde{\eta}(x)$ is periodic and symmetric (see (2.11)), it can be represented as a Fourier series,

$$\widetilde{\eta}(x) = \sum_{n=0}^{\infty} A_n \cos(nkx), \tag{2.40}$$

where A_n are the Fourier coefficients. Fixing the average level of the surface by using (2.9) gives $A_0 = 0$. Substituting (2.39) and (2.40) into the kinematic boundary condition (2.28) and collecting the coefficients of $\sin(nkx)$ yields

$$B_n = \frac{-cA_n}{\sinh(nkh)}. \tag{2.41}$$

Then we combine (2.39) and (2.40) with the dynamic boundary condition (2.29). The coefficients of $\cos(nkx)$ have to be all zero. It yields

$$(g - \frac{c^2 nk}{\tanh nkh} + \frac{D}{\rho}n^4 k^4)A_n = 0, \quad n = 1,2,3... \tag{2.42}$$

For a non-trivial solution, the amplitude from the leading order cannot be zero.

Therefore the coefficient of A_1 must be zero, which gives

$$c^2 = (\frac{g}{k} + \frac{D}{\rho}k^3) \tanh kh. \tag{2.43}$$

This is the linear dispersion relation for the flexural-gravity problem. If

$$g - \frac{c^2 nk}{\tanh nkh} + \frac{D}{\rho}n^4 k^4 \neq 0, \tag{2.44}$$

for all $n > 1$, then A_n must be all zero for $n > 1$. The solution of the linear problem is then

$$\phi(x, y) = cx - \frac{cA_1}{\sinh kh} \sin kx \cosh k(y + h) \tag{2.45}$$

$$\eta(x) = A_1 \cos kx. \tag{2.46}$$

It is a sinusoidal travelling wave. If (2.44) is not satisfied for some integer m, more terms come into the solution. This case will have to be considered when studying nonlinear waves Chapter 4.

Now we pay more attention to the dispersion relation (2.43). It describes the relation between the phase speed and the wavenumber.

In the case of infinite depth, (2.43) becomes

$$c^2 = \frac{g}{k} + \frac{D}{\rho}k^3, \tag{2.47}$$

which admits a minimum phase speed $c_{\min}$. This will be discussed further in the later work.

In the case of finite depth, the dispersion relation (2.43) can be rewritten as

$$F^2 = \left(\frac{1}{kh} + \sigma(kh)^3\right) \tanh kh, \tag{2.48}$$

where

$$F = \frac{c}{\sqrt{gh}} \tag{2.49}$$

is the Froude number and

$$\sigma = \frac{D}{\rho g h^4}. \tag{2.50}$$

For the related gravity-capillary problem (see [48] for a review), the linear dispersion relation is given by

$$F^2 = \left(\frac{1}{kh} + \tau kh\right) \tanh kh, \tag{2.51}$$

where $\tau = T/(\rho g h^2)$ is the Bond number. Unlike the gravity-capillary problem, (2.48) always admits a minimum. Two typical graphs of F^2 versus $1/(kh)$ are shown in Figure 2.3.
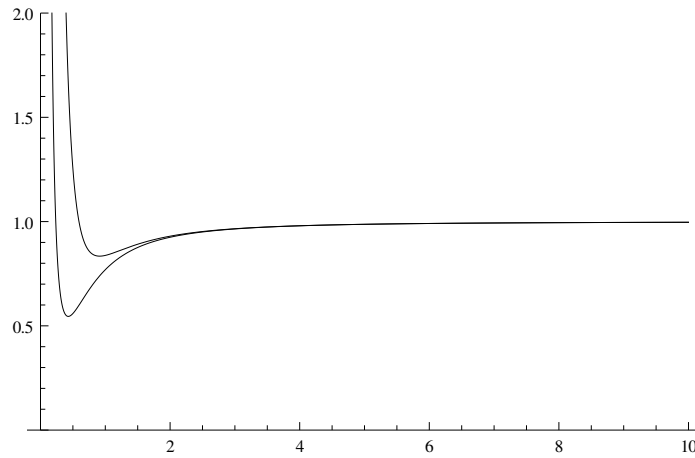
Figure 2.3: The values of F^2 versus $1/(kh)$ for $\sigma = 0.01$ (below) and $\sigma = 0.1$ (above).

2.4 Korteweg-de Vries equation

There is a big research interest involving long waves because the horizontal length scale is usually much greater than the vertical in the oceans. By assuming that the ratio of the depth over the wavelength is very small, the governing equations are

simplified as

$$\eta_t + c_0\eta_x + \frac{3}{2}\frac{c_0}{h}\eta\eta_x + \frac{c_0 h^2}{6}(1 - 3\tau)\eta_{xxx} + \frac{c_0 h^4}{360}(19 - 30\tau - 45\tau^2)\eta_{xxxxx} = 0 \quad (2.52)$$

for the gravity-capillary problem and

$$\eta_t + c_0\eta_x + \frac{3}{2}\frac{c_0}{h}\eta\eta_x + \frac{c_0 h^2}{6}\eta_{xxx} + (\frac{19}{360} + \frac{\sigma}{2})c_0 h^4\eta_{xxxxx} = 0 \quad (2.53)$$

for the flexural-gravity problem, where η is the displacement as usual and

$$c_0 = \sqrt{gh}, \qquad \tau = \frac{T}{\rho g h^2}, \qquad \sigma = \frac{D}{\rho g h^4}. \quad (2.54)$$

We note that (2.52) is called the fifth order Korteweg-de Vries (KdV) equation for the gravity-capillary problem which is valid for the Bond number τ being close to 1/3. It was first derived by [21] for travelling waves and by [20] in the unsteady case. Meanwhile, for τ being away from 1/3, the fifth order term can be eliminated so that (2.53) becomes the famous Korteweg-de Vries equation first introduced by [25] which is integrable and allows cnoidal waves and solitons of sech square type as its solutions. For the flexural-gravity problem, the flexural term only appears in the fifth order or more higher order terms. Only fifth order KdV equation is available. To balance the last three terms in (2.53), the coefficient σ is required to be of $O(l^2/h^2)$ (more details can be found in appendix A.2). We note that since σ is large, the term 19/360 appearing in (2.53) can be neglected. The system is not integrable which causes less interest since one may better investigate numerically the full Euler equations instead of this approximated model. As highlighted in [22], the model of an ideal incompressible fluid of finite depth beneath an initially stressed ice sheet is a generalisation of the model of an ideal incompressible fluid of finite depth with capillary effects. The types of solitary waves solutions of the two models are similar

in many respects. However, the gravity-capillary wave model is of purely theoretical interest since the scales on which the capillary forces are significantly small. In particular, the depth of the fluid (and therefore the amplitude) is of the order of a few millimeters. For such depths it is important to include viscosity effects therefore the inviscid fluid model is not valid. Consequently, for gravity-capillary waves it is meaningless to compare the theoretical results obtained within the framework of the ideal fluid model with experiment. For flexural-gravity waves there are no such restrictions on the depth of the fluid. The wave amplitude may have fairly large values even for a small deviation of the wave velocity from the phase velocity for infinitely long waves.

The dispersive terms from (2.52) and (2.53) can be predicted from the linear dispersion relations

$$\omega = \sqrt{\frac{c_0}{h}\Big(1 + \tau(kh)^2\Big)kh\tanh kh} \tag{2.55}$$

for the gravity-capillary problem and

$$\omega = \sqrt{\frac{c_0}{h}\Big(1 + \sigma(kh)^4\Big)kh\tanh kh} \tag{2.56}$$

for the flexural-gravity problem where $\omega = ck$ is the angular frequency. Now we introduce $\widetilde{h} = kh$ which describes the ratio of the depth over the wavelength. By assuming $\widetilde{h}$ to be very small, (2.55) and (2.56) can be expanded in power series of $\widetilde{h}$, which are

$$\omega = c_o k\left[1 + \frac{1}{2}(\tau - \frac{1}{3})\widetilde{h}^2 + (\frac{19}{360} - \frac{\tau}{12} - \frac{\tau^2}{8})\widetilde{h}^4\right] + O(\widetilde{h}^6). \tag{2.57}$$

and

$$\omega = c_o k\left[1 - \frac{1}{6}\widetilde{h}^2 + (\frac{19}{360} + \frac{\sigma}{2})\widetilde{h}^4\right] + O(\widetilde{h}^6). \tag{2.58}$$

respectively. As we can see from (2.57) and (2.58), the coefficients of $\widetilde{h}$ correspond

perfectly to those of the dispersive terms in (2.51) and (2.53). The fully detailed derivations of (2.52) and (2.53) are presented in appendix A.2 .

Chapter 3

Numerical schemes

In this chapter, we present various numerical methods which will be used in the following chapters to compute nonlinear solutions.

3.1 Series truncation method

3.1.1 Symmetric flexural waves in water of finite depth

We recall the governing equations

$$\nabla^2 \phi = 0, \qquad\qquad -h < y < \eta(x), \qquad (3.1)$$

$$\phi_y = \phi_x \eta_x, \qquad\qquad \text{on } y = \eta(x), \qquad (3.2)$$

$$\frac{1}{2}(\phi_x^2 + \phi_y^2) + gy + \frac{p}{\rho} = B, \qquad\qquad \text{on } y = \eta(x), \qquad (3.3)$$

$$\phi_y = 0, \qquad\qquad \text{on } y = -h, \qquad (3.4)$$

where

$$p = D(\kappa_{ss} + \frac{1}{2}\kappa^3). \qquad (3.5)$$

We use ϕ and ψ as independent variables and choose $\psi = 0$ on the free surface and $\phi = 0$ at a crest. We denote by $-Q$ the value of ψ on the bottom. Next we introduce the complex velocity $w = u - iv$. By writing $u - iv = ce^{\tau - i\theta}$, we have

$$x_\phi + iy_\phi = \frac{1}{u - iv} = \frac{1}{c}e^{-\tau + i\theta} \tag{3.6}$$

whose real part and imaginary part can be used to find x and y by integrating with respect to ϕ. Thus (3.3) becomes

$$\frac{c^2}{2}e^{2\tau(\phi,0)} + \frac{g}{c}\int_0^\phi e^{-\tau(\varphi,0)} \sin[\theta(\varphi,0)]d\varphi + \frac{D}{\rho}(\kappa_{ss} + \frac{1}{2}\kappa^3) = B. \tag{3.7}$$

By using (2.13), we have

$$\kappa_s = \frac{\partial\phi}{\partial s}\frac{\partial\kappa}{\partial\phi} + \frac{\partial\psi}{\partial s}\frac{\partial\kappa}{\partial\psi}. \tag{3.8}$$

Along a streamline (and in particular along the free surface),

$$\frac{\partial\psi}{\partial s} = 0, \quad \text{and} \quad \frac{\partial\phi}{\partial s} = ce^\tau. \tag{3.9}$$

Therefore

$$\kappa = ce^\tau\frac{\partial\theta}{\partial\phi} \tag{3.10}$$

and

$$(\kappa_{ss} + \frac{1}{2}\kappa^3) = c^3e^{3\tau}(\theta_{\phi\phi\phi} + 3\tau_\phi\theta_{\phi\phi} + \tau_{\phi\phi}\theta_\phi + 2\tau_\phi^2\theta_\phi + \frac{\theta_\phi^3}{2}). \tag{3.11}$$

The total energy of the system is

$$\frac{1}{2}\int_{-\infty}^\infty \int_{-\infty}^\eta (\phi_x^2 + \phi_y^2)dydx + \frac{1}{2}g\int_{-\infty}^\infty \eta^2 dx + \frac{1}{2}\frac{D}{\rho}\int_{-\infty}^\infty \frac{\eta_{xx}^2}{(1 + \eta_x^2)^{5/2}}dx, \tag{3.12}$$

where these three integrals correspond to the kinetic energy, the gravitational potential energy and elastic potential energy respectively.
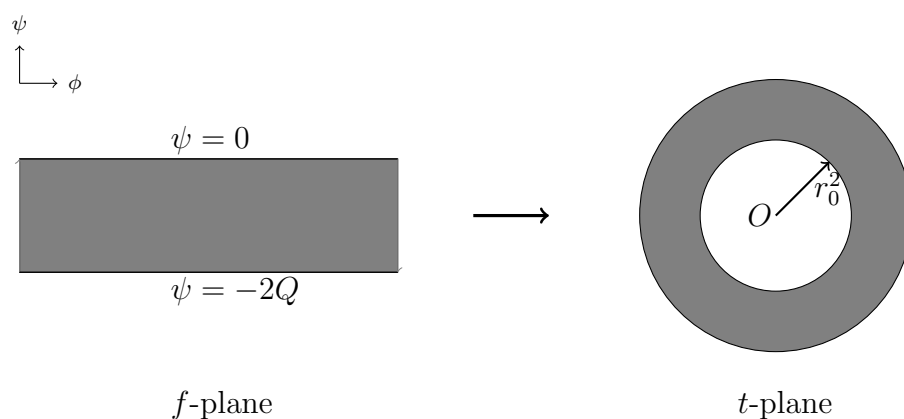
Figure 3.1: The conformal mapping (3.13) maps the strip $-2Q < \psi < 0$ on to an annulus $r_0^2 < |t| < 1$ whose outer and inner boundary correspond respectively to the free surface and the image of the free-surface into the bottom in the physical plane.

We note that a formulation similar to that described in this section was used before in [51] for the KL model.

The flow domain in the complex potential plane is the strip $-Q < \psi < 0$. The kinematic boundary condition (3.4) on the bottom can be satisfied by using the method of images. Then we have $\psi = -2Q$ on the image of the free-surface into the bottom. Hence the extended flow domain is the strip $-2Q < \psi < 0$. Then we perform the conformal mapping

$$t = e^{-\frac{2i\pi f}{c\lambda}}, \tag{3.13}$$

where $f = \phi + i\psi$ is the complex potential and λ is the wavelength.

It maps the strip onto the annulus $r_0^2 < |t| < 1$ (see figure 3.1), where

$$r_0 = e^{\frac{-2\pi Q}{c\lambda}}. \tag{3.14}$$

Since w is an analytic function of f, so is $\tau - i\theta$. Hence $\tau - i\theta$ is an analytic function of t which can be represented by the Laurent series

$$\tau - i\theta = a_0 + \sum_{n=1}^{\infty} a_n t^n + \sum_{n=1}^{\infty} b_n t^{-n}. \tag{3.15}$$

Since $\psi = -2Q$ is the image of the surface $\psi = 0$, we obtain

$$\tau(\phi, 0) - i\theta(\phi, 0) = \tau(\phi, -2Q) + i\theta(\phi, -2Q). \tag{3.16}$$

Combining (3.15) and (3.16) gives

$$b_n = a_n r_0^{2n}. \tag{3.17}$$

We choose c as the unit velocity and Q/c as the unit length. In dimensionless variables, (3.7) becomes

$$\frac{1}{2}e^{2\tau} + \frac{1}{F^2}\int_0^\phi e^{-\tau(\varphi)}\sin\theta(\varphi)d\varphi + \beta(\kappa_{ss} + \frac{1}{2}\kappa^3) = B, \tag{3.18}$$

where B is the dimensionless Bernoulli constant,

$$F = \frac{c}{\sqrt{gh}} \tag{3.19}$$

is the Froude number and

$$\beta = \frac{Dc}{\rho Q^3}. \tag{3.20}$$

One can easily rewrite (3.14) as

$$r_0 = e^{-\frac{2\pi}{l}} \tag{3.21}$$

where l is the dimensionless wavelength. By substituting (3.13) into (3.15) and truncating the series after $N - 2$ terms, we get

$$\tau = a_0 + \sum_{n=1}^{N-2} \cos(kn\phi)(1 + r_0^{2n})a_n, \tag{3.22}$$

$$\theta = \sum_{n=1}^{N-2} \sin(kn\phi)(1 - r_0^{2n})a_n. \tag{3.23}$$

Now we introduce $N-1$ collocation points uniformly distributed in $[0, \frac{l}{2}]$,

$$\phi_I = \frac{l}{2}\frac{I-1}{N-2}, \quad I = 1, 2, \dots N-1. \tag{3.24}$$

The dynamic boundary condition (3.18) is satisfied at these points, which yields $N-1$ algebraic equations. The periodicity of the wave implies

$$x = \frac{l}{2} \quad \text{when } \phi = \frac{l}{2}. \tag{3.25}$$

Fixing the amplitude gives the additional equation

$$|y(\frac{l}{2}) - y(0)| = A = Sl, \tag{3.26}$$

where S is the steepness (i.e. the difference of heights between a crest and a trough divided by the wavelength) and A is the height of the wave. By fixing β, A and l, the resulting system with $N+1$ equations and $N+1$ unknowns $(a_0, a_1, \dots, a_{N-2}, B, F)$ can be solved by Newton's method. The error of the numerical solution obtained by Newton's method is set to be less than 10^{-10}. Once the solution is obtained, one can get the values of x and y by integrating x_ϕ and y_ϕ respectively (see (3.6)). This gives the profile of the wave.

3.1.2 Symmetric flexural waves in deep water

In the case of infinite depth, the numerical scheme in Section 3.1 remains valid except that we now use the reference length $(D/\rho c^2)^{\frac{1}{3}}$ since Q/c tends to infinity as the depth tends to infinity. Following (3.14), $r_0 = 0$ since h tends to infinity and so $b_n = 0$ by (3.17). The dynamic boundary condition (3.7) becomes

$$\frac{1}{2}e^{2\tau} + \gamma \int_0^\phi e^{-\tau(\varphi)} \sin\theta(\varphi)d\varphi + \partial_s^2\kappa + \frac{1}{2}\kappa^3 = B, \tag{3.27}$$

where

$$\gamma = (Dg^3/\rho c^8)^{\frac{1}{3}}. \tag{3.28}$$

We note that γ is related to the phase velocity c. In Section 3.1.4 we use this parameter to test the numerical accuracy. According to [27], the energy can be expressed in terms of the variables on the free surface. In terms of the dimensionless variables, it is

$$-\frac{1}{2}\gamma^{-\frac{3}{8}}\int_{-\infty}^{\infty} y\,d\phi + \frac{1}{2}\int_{-\infty}^{\infty} y^2 x_\phi \,d\phi + \frac{1}{2}\int_{-\infty}^{\infty} \frac{(y_{\phi\phi}x_\phi - x_{\phi\phi}y_\phi)^2}{(x_\phi^2 + y_\phi^2)^{5/2}}\,dx. \tag{3.29}$$

3.1.3 Non-symmetric periodic waves

For studying non-symmetric periodic waves, we perform the same conformal mapping 3.13 as explained in Section 3.1.1. In the case of infinite depth, the flow domain which corresponds to the lower half plane of the complex potential (ϕ, ψ) plane is mapped onto a unit disc (as shown in Figure 3.2). Then we choose

$$c \quad \text{and} \quad \frac{\lambda}{2\pi} \tag{3.30}$$

as the reference velocity and length respectively. Since w is an analytic function of f, so is $\tau - i\theta$. Hence $\tau - i\theta$ is an analytic function of t which can be represented by the Laurent series

$$\tau - i\theta = \alpha_0 + \sum_{n=1}^{\infty} \alpha_n t^n + \sum_{n=1}^{\infty} \beta_n t^{-n}. \tag{3.31}$$

where the coefficients $\alpha_n,\ \beta_n \in \mathbb{C}$ except $\alpha_0 \in \mathbb{R}$. Hence we may write

$$\alpha_n = -a_n + ib_n, \tag{3.32}$$

with $a_n,\ b_n \in \mathbb{R}$ for all $n \geq 1$. In particular, the coefficients b_n are all zero in the case of symmetric waves. The minus sign in front of a_n on the right hand side of equation

(3.32) is chosen so that the definitions of a_n and b_n accord with those presented in [40]. Since $\psi = -2Q$ is the image of the surface $\psi = 0$, we obtain

$$\tau(\phi, 0) - i\theta(\phi, 0) = \tau(\phi, -2Q) + i\theta(\phi, -2Q). \tag{3.33}$$

Combining (3.31) and (3.33) gives

$$\beta_n = \alpha_n r_0^{2n}, \qquad \text{for } n \geq 1. \tag{3.34}$$

By substituting (3.32) into (3.15) and truncating after N terms, we obtain

$$\tau = \alpha_0 - \sum_{n=1}^{N} a_n(1 + r_0^{2n}) \cos n\phi + b_n(1 - r_0^{2n}) \sin n\phi, \tag{3.35}$$

$$\theta = \sum_{n=1}^{N} -a_n(1 - r_0^{2n}) \sin n\phi - b_n(1 + r_0^{2n}) \cos n\phi. \tag{3.36}$$

In the particular case of infinite depth (i.e. $h \to \infty$), the strip in Figure 3.1 becomes the lower-half f-plane and the annulus extends to a unit disc as sketched in Figure 3.2, i.e. $r_0 = 0$. The Laurent series (3.31) becomes a Taylor series since all the coefficients β_n decay. Also α_0 is zero because the velocity at infinite depth equals the phase speed whose value is 1 under the current scaling.
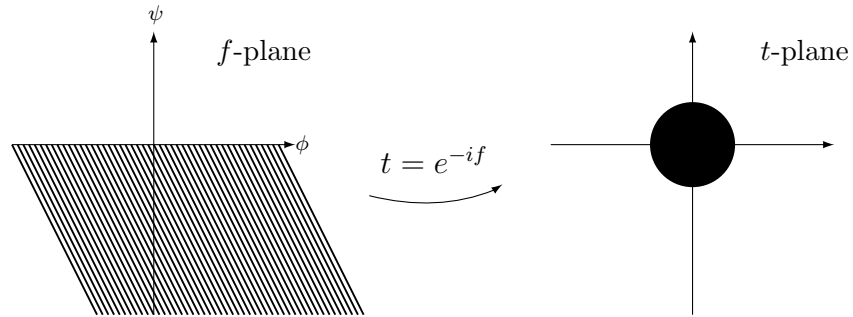
Figure 3.2: The conformal mapping in the case of infinite depth.

Symmetry-breaking occurs as a bifurcation from symmetric waves. Thus we start with reproducing results for symmetric waves. The rescaled wavelength and

the rescaled phase velocity are always set to be 2π and 1 respectively. Using the definition of c,

$$c = \frac{1}{\lambda} \int_0^\lambda \phi_x dx, \tag{3.37}$$

we obtain

$$x = 2\pi, \quad \text{when } \phi = 2\pi. \tag{3.38}$$

The wave is symmetric in the physical plane with respect to $x = \pi$ and in the complex potential plane with respect to $\phi = \pi$. By imposing the symmetry condition on (3.38), we have immediately

$$x = \pi, \quad \text{when } \phi = \pi. \tag{3.39}$$

Then we introduce N collocation points uniformly distributed along ϕ in $[0, \pi]$

$$\phi_j = \frac{(j - \frac{1}{2})\pi}{N}, \quad j = 1, 2, ...N. \tag{3.40}$$

The dynamic boundary condition (8.11) is satisfied at these points, which yields N algebraic equations. The final equation to fix the value of a specific coefficient, e.g.

$$a_m = \alpha, \tag{3.41}$$

where m and α are suitably chosen. By fixing the value of p and a_m, the resulting system with $N + 2$ equations and $N + 2$ unknowns $(\alpha_0, a_1, ..., a_N, q)$ can be solved by Newton's method. During the numerical calculations, we pay extra attention to the value of the Jacobian since bifurcation occurs when its value changes sign. We note that (3.41) is particularly useful for computing the solutions near bifurcation points.

For non-symmetric waves, the coefficients b_n are non-zero. We need to introduce

another N collocation points along ϕ in $(\pi, 2\pi]$ in addition to the previous ones

$$\phi_j = \frac{(j - \frac{1}{2})\pi}{N}, \quad j = N + 1, N + 2, ...2N. \tag{3.42}$$

The dynamic boundary condition (8.11) is also satisfied on these points, which yields extra N algebraic equations. Meanwhile, (3.39) is replaced by (3.38). The final control equation is to fix one of the coefficients b_n, e.g.

$$b_m = \beta, \tag{3.43}$$

where m and β are suitably chosen. We have a system with $2N + 2$ equations and $2N + 2$ unknowns $(\alpha_0, a_1, ..., a_N, b_1, b_2, ..., b_N, q)$ which can again be solved by Newton's method. To avoid small shifted symmetric waves, we replace one of the dynamic boundary conditions satisfied at the collocation points by

$$\sum_{n=1}^{N} b_n = 0. \tag{3.44}$$

This condition is to make sure that a crest or a trough lies at the origin as explained in [40]. One can get the wave profiles by integrating x_ϕ and y_ϕ once the Fourier coefficients are obtained. This numerical method was successfully used in several different problems, e.g. see [1], [40] or [13]. A discussion on the accuracy of this numerical method was presented in [13]. As we shall see in Chapter 8, the challenge is here to find suitable guesses to jump on branches of non-symmetric waves.

3.1.4   Numerical Accuracy

We check the convergence and accuracy of our numerical procedure in the particular case of symmetric flexural waves in infinite depth. As shown in Section 2.3, when the amplitude of the waves is small, the equations of Section 2.2 can be linearised

			Error		
Wavelength	N	$S = 0.001$	$S = 0.002$	$S = 0.1$	$S = 0.2$
10	20	1.08×10^{-3}	1.08×10^{-3}	1.50×10^{-3}	1.74×10^{-2}
10	100	3.96×10^{-5}	3.95×10^{-5}	4.06×10^{-4}	1.64×10^{-2}
10	500	1.52×10^{-6}	1.41×10^{-6}	3.66×10^{-4}	1.63×10^{-2}
10	1000	3.51×10^{-7}	2.37×10^{-7}	3.65×10^{-4}	1.63×10^{-2}
10	2000	5.90×10^{-8}	5.56×10^{-8}	3.65×10^{-4}	1.63×10^{-2}

Table 3.1: The values of e for periodic waves of small and finite amplitude.

and solved analytically. The (linear) dispersion relation of the waves is then

$$c^2 = \frac{g}{k} + \frac{D}{\rho}k^3 \qquad (3.45)$$

where $k = 2\pi/\lambda$ is the wavenumber (see (2.47)). Using the dimensionless variables of Section 3.1.2, we can rewrite (3.45) as

$$\gamma = k - k^4, \qquad (3.46)$$

where γ is defined by (3.28). Now we consider the quantity e defined by

$$e = |\gamma_n - \gamma_t|, \qquad (3.47)$$

where γ_t is the theoretical value predicted by (3.46) and γ_n is the corresponding numerical value given by the numerical procedure of Section 3.1 .

From Table 3.1, it can be seen in the column of $s = 0.001$ and $s = 0.002$ that e converges quickly to a value that is essentially equal to zero as the number of

		γ			
Wavelength	N	$S = 0.1$	$S = 0.15$	$S = 0.2$	$S = 0.25$
10	20	0.47396	0.47717	0.48989	0.54572
10	100	0.47287	0.47605	0.48883	0.54475
10	500	0.47283	0.47601	0.48879	0.54471
10	1000	0.47283	0.47601	0.48879	0.54471
10	2000	0.47283	0.47601	0.48879	0.54471

Table 3.2: The values of γ for periodic waves of finite amplitude.

collocation points increases. It can also be seen from the last two columns of Table 3.1 that the numerical values of γ for periodic waves of finite amplitude are different from the values of γ_t obtained from the linear dispersion relation (3.62) because of the nonlinearity. We compute γ_n for different values of N. Table 3.2 shows that γ_n converges quickly as N increases. In most of computations presented in this chapter we used $N = 500$.

3.2   Time-dependent Euler system in deep water

For the time-dependent problem, time-derivatives are included in equations (2.4) and (2.5). This gives

$$\eta_t = \phi_y - \eta_x \phi_x \tag{3.48}$$

$$\phi_t = -\tfrac{1}{2}\left[\phi_x^2 + \phi_y^2\right] - g\eta - \tfrac{p}{\rho} + P_e(x,t)\,, \tag{3.49}$$

where p is given by (2.20). We have included an extra external pressure P_e in (3.49) to study forcing problems (see Chapter 5). The problem is then defined by (2.3), (2.6), (3.48) and (3.49) In order to remove all the constants, the whole system can be non-dimensionalised by choosing

$$\left[\frac{D}{\rho g}\right]^{1/4}, \qquad \left[\frac{D}{\rho g^5}\right]^{1/8}, \qquad \left[\frac{gD^3}{\rho^3}\right]^{1/8} \tag{3.50}$$

as the units of length, time and potential respectively. With a little abuse of notations, (3.49) can be recast as

$$\phi_t = -\frac{1}{2}\left[\phi_x^2 + \phi_z^2\right] - \eta - \left(\frac{1}{2}\kappa^2 + \kappa_{ss}\right) + P(x,t)\,. \tag{3.51}$$

If the external forcing is negligible, the equations (2.3) (2.6) (2.20) (3.48) and (3.51) form a Hamiltonian system with the action functional being the total energy of the fluid which is the sum of the kinetic energy and the potential energy:

$$\mathcal{E} = \frac{1}{2} \left[\int_{\mathbb{R}} dx \int_{-\infty}^{\eta} \left(\phi_x^2 + \phi_y^2 \right) dy + \int_{\mathbb{R}} \eta^2 \, dx + \int \kappa^2 \, ds \right], \tag{3.52}$$

where $\mathbb{R}$ is the whole real line. Assume the velocity potential on the free surface is designated as $\varphi(x,t) \triangleq \phi(x, \eta(x,t), t)$. Working in the canonical variables φ and η, the kinematic and dynamic boundary conditions can be recast as:

$$\eta_t = \frac{\delta \mathcal{E}}{\delta \varphi}, \qquad \varphi_t = -\frac{\delta \mathcal{E}}{\delta \eta}. \tag{3.53}$$

It is noted that the effects due to inertia and the thickness of the elastic sheet can also be incorporated into the pressure equation (3.51) (see [41] for the expression of the inertia and [11] for how to model the system with the thickness of the plate). However the simulations of unsteady waves become much more complicated when the inertia is taken into account. For simplicity we neglect these two effects, and only consider the pressure jump exerted by the elastic sheet owing to flexing. The hydroelastic wave problem has been modelled with a variety of methods (the reader is referred to [31] for a discussion).

The main idea for solving the two-dimensional full Euler equations is based on a time-dependent conformal mapping, a numerical method pioneered by [9]. We start the derivation with finding a transformation that maps the physical domain $-\infty < y < \eta(x,t)$ into the lower half plane with horizontal and vertical coordinates denoted by ξ and ζ respectively. The conformal mapping from (x,y) to (ξ, ζ) can be

found by solving the following boundary-value problem:

$$
\begin{cases}
y_{\xi\xi} + y_{\zeta\zeta} = 0 & \text{for } -\infty < \zeta < 0 \\[2mm]
y = Y(\xi, t) & \text{at } \zeta = 0 \\[2mm]
y \sim \zeta & \text{as } \zeta \to -\infty
\end{cases}
\tag{3.54}
$$

where $Y(\xi, t) = \eta(x(\xi, 0, t), t)$. The harmonic conjugate $x(\xi, \zeta, t)$ is defined through the Cauchy-Riemann relations for the complex function $x(\xi, \zeta, t) + iy(\xi, \zeta, t)$. In the transformed plane, the velocity potential ϕ and its harmonic conjugate $\psi(\xi, \zeta, t)$ also satisfy Laplace's equations. Defining $\Phi(\xi, t) \triangleq \phi(x(\xi, 0, t), y(\xi, 0, t), t)$, $\Psi(\xi, t) \triangleq \psi(\xi, 0, t)$ and $X(\xi, t) \triangleq x(\xi, 0, t)$, we have from elementary harmonic analysis

$$
X = \xi - \mathcal{H}[Y] \quad \text{and} \quad \Psi = \mathcal{H}[\Phi],
\tag{3.55}
$$

where $\mathcal{H}$ is the operator of Hilbert Transformation with the Fourier symbol $i\mathrm{sgn}(k)$. Also it can be defined in the physical space as

$$
\mathcal{H}[f](\xi) = \mathrm{PV} \int_{\mathbb{R}} \frac{f(\xi')}{\xi' - \xi}\, d\xi',
\tag{3.56}
$$

where 'PV' means we take the Cauchy principal value of the integral. By using the chain rule, the kinematic boundary condition in the transformed plane is of the form

$$
X_\xi Y_t - Y_\xi X_t = -\Psi_\xi.
\tag{3.57}
$$

Following [10], the evolution equation for Y takes the form

$$
Y_t = Y_\xi \mathcal{H}\left[\frac{\Psi_\xi}{J}\right] - X_\xi \frac{\Psi_\xi}{J}
\tag{3.58}
$$

where $J = X_\xi^2 + Y_\xi^2$ is the Jacobian of the conformal map. Details are presented in

Appendix B. Finally we reformulate the dynamic boundary condition using the new variable ξ as

$$\Phi_t = \frac{\Psi_\xi^2 - \Phi_\xi^2}{2J} - Y - \frac{1}{2}\left[\frac{\kappa_{\xi\xi}}{J} + \left(\frac{\kappa_\xi}{J}\right)_\xi + \kappa^3\right] + \Phi_\xi \mathcal{H}\left[\frac{\Psi_\xi}{J}\right] + \mathcal{P}_e, \qquad (3.59)$$

with

$$\kappa = \frac{X_\xi Y_{\xi\xi} - X_{\xi\xi} Y_\xi}{J^{3/2}}. \qquad (3.60)$$

In order to find the dispersion relation of the system, we linearise the surface Euler system (3.58)-(3.59) and take Y, Φ_ξ, Ψ_ξ small, $\mathcal{P}_e = 0$ and $X_\xi \sim 1$, $J \sim 1$

$$\begin{cases} Y_t = -\Psi_\xi = -\mathcal{H}[\Phi_\xi] \\[2mm] \Phi_t = -Y - Y_{\xi\xi\xi\xi} \end{cases} \qquad (3.61)$$

which yields $\Phi_{tt} = \mathcal{H}[\Phi_\xi] + \mathcal{H}[\Phi_{\xi\xi\xi\xi\xi}]$, then the dispersion relation is

$$\omega^2 = |k|(1 + k^4). \qquad (3.62)$$

By using this dispersion relation, we know that as $k = (1/3)^{1/4}$ the group velocity equals the phase velocity, which implies the minimum phase speed $c_{\min} \approx 1.3247$ under our choice of dimensionless variables.

We then reformulate the system to seek fully localized solutions traveling with wave speed c. In order to make sure there are no waves in the far field, we choose $c < c_{\min}$. We assume functions Y and Φ depend on $\xi - ct$, then it follow from (3.57) that

$$\Psi_\xi = cY_\xi, \quad \text{and hence} \quad \Phi_\xi = -c\mathcal{H}[Y_\xi]. \qquad (3.63)$$

From (3.58), one can conclude that

$$\mathcal{H}\left[\frac{\Psi_\xi}{J}\right] = c\left(\frac{X_\xi}{J} - 1\right). \tag{3.64}$$

Substituting (3.63) and (3.64) into the dynamic boundary condition (3.59) with $\mathcal{P}_e = 0$ (since we seek free solitary waves) and noticing that $\Phi_t = -c\Phi_\xi$, one obtains the following nonlinear equation after some algebra

$$\frac{c^2}{2}\left(\frac{1}{J} - 1\right) + Y + \frac{1}{2}\left[\frac{\kappa_{\xi\xi}}{J} + \left(\frac{\kappa_\xi}{J}\right)_\xi + \kappa^3\right] = 0. \tag{3.65}$$

This, together with $X_\xi = 1 - \mathcal{H}[Y_\xi]$, completes an integro-differential system, and the velocity potential can be recovered by $\Phi = -c\mathcal{H}[Y]$. Finally, the Hamiltonian (3.52) in the new coordinates becomes

$$\mathcal{E} = \frac{c^2}{2}\int_\mathbb{R} Y_\xi \mathcal{H}[Y]\,d\xi + \frac{1}{2}\int_\mathbb{R} Y^2 X_\xi\,d\xi + \frac{1}{2}\int_\mathbb{R} \frac{(Y_{\xi\xi}X_\xi - X_{\xi\xi}Y_\xi)^2}{J^{5/2}}\,d\xi. \tag{3.66}$$

In Chapter 6, we use this scheme to compute solitary waves. This will be achieved by approximating the solitary waves by long periodic waves with flat tails. Therefore the equation (3.65) can be solved numerically using truncated Fourier series of Y, namely,

$$Y(\xi) = \sum_{n=1}^N a_n \cos(n\pi\xi/L) + \sum_{n=1}^N b_n \sin(n\pi\xi/L). \tag{3.67}$$

The Fourier coefficients a_n and b_n are treated as unknowns which need to be solved by Newton's method. We discretise the domain $[-L, L)$ into a uniform mesh. We evaluate the dynamics boundary condition (3.65) on the grid points and then project it onto each element of the $\cos(n\pi\xi/L)$ and $\sin(n\pi\xi/L)$ basis for $n = 0, 1, \cdots, N$. All the derivatives and the Hilbert transform are calculated via Fourier multipliers making the program efficient and accurate, while the nonlinear terms are computed

in real space. The underlying period L and the total wavenumber N are both chosen to be sufficiently large so that the wave profiles hardly change as L and N further increase, and in most computations, we keep the mesh size $\Delta\xi = 0.05$. We stop the Newton scheme as the $l^\infty-$norm of the residual error is less than 10^{-10}. It is noted that for symmetric solitary waves $b_n = 0$ for arbitrary n, which saves half the number of the computation.

In Chapter 7, the time dependent scheme is used to study the stability and the dynamics of the waves.

Chapter 4

Flexural periodic waves and generalised solitary waves

Previously in Section 2.3, we have studied the flexural-gravity waves of small amplitude by using the linear theory. In this chapter, we work on the nonlinear periodic waves and on the generalised solitary waves.

4.1 Stokes expansion

In this section, we are going to investigate nonlinear periodic surface waves by using the Stokes expansion which was first introduced in [43]. This topic has been studied in [51] with the KL model. Here we used the Plotnikov-Toland model. We follow the formulation from Section 2.2. The governing equations are (2.3)-(2.12). We consider the following expansions

$$\phi(x, y) = cx + \epsilon\phi_1(x, y) + \epsilon^2\phi_2(x, y) + O(\epsilon^3), \tag{4.1}$$

$$\eta(x) = \epsilon\eta_1(x) + \epsilon^2\eta_2(x) + O(\epsilon^3), \tag{4.2}$$

$$c = c_0 + \epsilon c_1 + \epsilon^2 c_2 + O(\epsilon^3), \tag{4.3}$$

$$B = B_0 + \epsilon B_1 + \epsilon^2 B_2 + O(\epsilon^3). \tag{4.4}$$

Here ϵ is a small parameter measuring the size of amplitude. A precise definition will be given later. Since (2.4) and (2.5) are imposed on $y = \eta(x)$, we need to expand $\phi_x(x, \eta(x))$ and $\phi_y(x, \eta(x))$ about $y = 0$,

$$\phi_x(x, \eta(x)) = \phi_x(x, 0) + \eta(x)\phi_{xy}(x, 0) + \frac{\eta(x)^2}{2}\phi_{xyy}(x, 0) + O(\eta(x)^3) \tag{4.5}$$

$$\phi_y(x, \eta(x)) = \phi_y(x, 0) + \eta(x)\phi_{yy}(x, 0) + \frac{\eta(x)^2}{2}\phi_{yyy}(x, 0) + O(\eta(x)^3) \tag{4.6}$$

We substitute the expansion (4.1)-(4.6) into the system (2.3)-(2.12) and equate terms of equal power in ϵ. The leading order term gives

$$B_0 = \frac{c_0^2}{2}. \tag{4.7}$$

The linear system obtained at the order of ϵ is

$$\nabla^2 \phi_1 = 0, \qquad\qquad -h < y < 0, \tag{4.8}$$

$$\phi_{1y} = c_0 \eta_{1x}, \qquad\qquad \text{on } y = 0, \tag{4.9}$$

$$c_0 \phi_{1x} + g\eta_1 + \frac{D}{\rho}\eta_{1xxxx} = B_1 - c_0 c_1, \qquad\qquad \text{on } y = 0, \tag{4.10}$$

$$\phi_{1y} = 0, \qquad\qquad \text{on } y = -h. \tag{4.11}$$

The system obtained from the terms of $O(\epsilon^2)$ is

$$\nabla^2 \phi_2 = 0, \qquad\qquad -h < y < 0, \tag{4.12}$$

$$\phi_{2y} + \eta_1 \phi_{1yy} = c_1 \eta_{1x} + c_0 \eta_{2x} + \phi_{1x}\eta_{1x}, \qquad \text{on } y = 0, \tag{4.13}$$

$$\frac{1}{2}(\phi_{1x}^2 + \phi_{1y}^2) + g\eta_2 + \frac{D}{\rho}\eta_{2xxxx} = B_2 - c_0 c_2 - \frac{c_1^2}{2}$$

$$- c_0\eta_1\phi_{1xy} - c_1\phi_{1x} - c_0\phi_{2x}, \qquad \text{on } y = 0, \tag{4.14}$$

$$\phi_{2y} = 0, \qquad\qquad \text{on } y = -h. \tag{4.15}$$

We solve the Laplace equations (4.8) and (4.12) by separating variables as we have seen in Section 2.3. It yields

$$\phi_1(x,y) = \sum_{n=1}^{\infty} B_n \cosh nk(y+h) \sin nkx, \tag{4.16}$$

$$\phi_2(x,y) = \sum_{n=1}^{\infty} F_n \cosh nk(y+h) \sin nkx, \tag{4.17}$$

$$\eta_1(x) = \sum_{n=1}^{\infty} A_n \cos nkx, \tag{4.18}$$

$$\eta_2(x) = \sum_{n=1}^{\infty} E_n \cos nkx. \tag{4.19}$$

The value of A_1 depends on the definition of the parameter ϵ. We use $\epsilon = \frac{a}{\lambda}$ as seen in [48] where a is the first Fourier coefficient of $\eta(x)$ defined as

$$a = \frac{2}{\lambda} \int_0^{\lambda} \eta(x) \cos(kx) dx. \tag{4.20}$$

By subsituting (4.2) (4.19) and (4.18) into the equation above and balancing both sides in ϵ, we get

$$A_1 = \lambda, \tag{4.21}$$

$$E_1 = 0. \tag{4.22}$$

We note that the system (4.8)-(4.11) is identical to (2.27)-(2.30). Therefore the solutions for c_0^2, ϕ_1 and η_1 agree with the ones found in Section 2.3. They are

$$c_0^2 = \left(\frac{g}{k} + \frac{D}{\rho}k^3\right) \tanh kh, \tag{4.23}$$

$$\phi_1 = -\frac{c_0 A_1}{\sinh kh} \cosh k(y+h) \sin kx, \tag{4.24}$$

$$\eta_1 = A_1 \cos(kx), \tag{4.25}$$

provided that

$$g + \frac{D}{\rho}n^4 k^4 - \frac{c_0^2 nk}{\tanh nkh} \neq 0, \quad n = 2, 3, 4... \tag{4.26}$$

Next we substitute (4.23)-(4.25) into (4.12)-(4.15) and solve for ϕ_2, η_2 and c_1. By equating coefficients of $\sin(nkx)$ in (4.9), we obtain

$$c_1 A_1 + F_1 \sinh kh = 0, \tag{4.27}$$

$$4F_2 \sinh^2 kh - A_1^2 c_0 k = 0, \tag{4.28}$$

$$nF_n k \sinh nkh = 0. \tag{4.29}$$

Equating coefficients of $\cos nkx$ in (4.14) gives

$$gE_1 + \frac{D}{\rho}k^4 E_1 = -c_0 kF_1 \cosh kh + A_1 c_0 c_1 k \coth kh, \tag{4.30}$$

$$gE_2 + 16\frac{D}{\rho}k^4 E_2 = \frac{1}{2}A_1^2 c_0^2 k^2 - 2c_0 kF_2 \cosh 2kh, \tag{4.31}$$

$$gE_n + n^4\frac{D}{\rho}k^4 E_n = -nc_0 F_n k \cosh nkh. \tag{4.32}$$

Combining (4.21), (4.27), (4.29), (4.30) and (4.32) gives

$$E_1 = 0, \ F_1 = 0, \ c_1 = 0, \tag{4.33}$$

$$E_n = 0, \ F_n = 0, \ \text{for } n = 3, 4, 5... \tag{4.34}$$

From (4.28) and (4.31), we obtain

$$F_2 = \frac{kA_1^2 c_0}{4\sinh^2 kh}, \tag{4.35}$$

$$E_2 = (g + 16\frac{D}{\rho}k^4)^{-1}(\frac{1}{2}A_1^2 c_0^2 k^2 - 2c_0 kF_2 \cosh 2kh). \tag{4.36}$$

Therefore

$$\eta_2 = E_2 \cos 2kx, \tag{4.37}$$

$$\phi_2 = F_2 \cosh 2nk(y+h) \sin 2nkx, \tag{4.38}$$

where E_2 and F_2 can be found in (4.35) and (4.36). This concludes the calculation up to order $O(\epsilon^2)$. To find the value of B_2 and c_2, one need to access order $O(\epsilon^3)$. The details of computations are not presented here since they are qualitively similar to those obtained in the gravity-capillary problem (see [48]).

If there exists an integer $m \geq 2$ such that

$$g + \frac{D}{\rho} m^4 k^4 - \frac{c_0^2 mk}{\tanh mkh} = 0, \tag{4.39}$$

then the solution is

$$\phi_1 = -\frac{c_0 A_1}{\sinh kh} \cosh k(y+h) \sin kx - \frac{c_0 A_m}{\sinh mkh} \cosh mk(y+h) \sin mkx, \tag{4.40}$$

$$\eta_1 = A_1 \cos(kx) + A_m \cos(mkx). \tag{4.41}$$

where A_m is determined at higher order. Now we examine in more details the situation when (4.39) is satisfied. For simplicity, we restrict our attention to infinite depth and $m = 2$.

$$c_0^2 = \frac{g}{k} + \frac{D}{\rho} k^3, \tag{4.42}$$

$$g + 16\frac{D}{\rho} k^4 - 2c_0^2 k = 0, \tag{4.43}$$

$$\phi_1 = -c_0 A_1 e^{ky} \sin(kx) - c_0 A_2 e^{2ky} \sin(2kx), \tag{4.44}$$

$$\eta_1 = A_1 \cos(kx) + A_2 \cos(2kx). \tag{4.45}$$

By substituting (4.42) into (4.43), we have

$$k^4 = \frac{\rho g}{14D}. \tag{4.46}$$

The cosh term in (4.17) becomes exponential,

$$\phi_2(x, y) = \sum_{n=1}^{\infty} F_n e^{nky} \sin nkx, \tag{4.47}$$

Using (4.19), (4.44), (4.45) and(4.47) in the kinematic boundary condition (4.13) we collect the coefficients of $\sin kx$ and $\sin 2kx$ to get the following two equations

$$F_1 k + c_1 A_1 k = \frac{3}{2} c_0 A_1 A_2 k^2, \tag{4.48}$$

$$2A_2 c_1 k + 2c_0 E_2 k + 2F_2 k = A_1^2 c_0 k^2. \tag{4.49}$$

Similarly by substituting the solution into the dynamics boundary condition (4.14) and equating the coefficients of $\cos kx$ and $\cos 2kx$ yields

$$- A_1 c_0 c_1 k + c_0 F_1 k = \frac{1}{2} A_1 A_2 c_0^2 k^2, \tag{4.50}$$

$$(g + 16\frac{D}{\rho} k^4) E_2 - 2A_2 c_0 c_1 k + 2c_0 F_2 k = \frac{1}{2} A_1^2 c_0^2 k^2. \tag{4.51}$$

Combining (4.48) and (4.50) gives

$$c_1 = \frac{1}{2} c_0 A_2 k. \tag{4.52}$$

Substituting (4.49) into (4.51) gives

$$(g + 16\frac{D}{\rho} k^4 - 2c_0^2 k) E_2 = 4A_2 c_0 c_1 k - \frac{1}{2} A_1^2 c_0^2 k^2. \tag{4.53}$$

By assumption (4.43), the left hand side equals zero. Hence we obtain

$$c_1 = \frac{A_1^2 c_0 k}{8 A_2}. \tag{4.54}$$

Then (4.52) and (4.54) give the following relations,

$$A_1 = \pm \frac{1}{2} A_2, \tag{4.55}$$

$$c_1 = \pm \frac{1}{4} c_0 k A_1. \tag{4.56}$$

Therefore the corresponding solution is

$$\eta_1 = A_1 \cos kx \pm \frac{1}{2} A_1 \cos 2kx, \tag{4.57}$$

$$\phi_1 = -c_0 A_1 e^{ky} \sin kx \mp \frac{c_0}{2} A_1 e^{2ky} \sin 2kx. \tag{4.58}$$
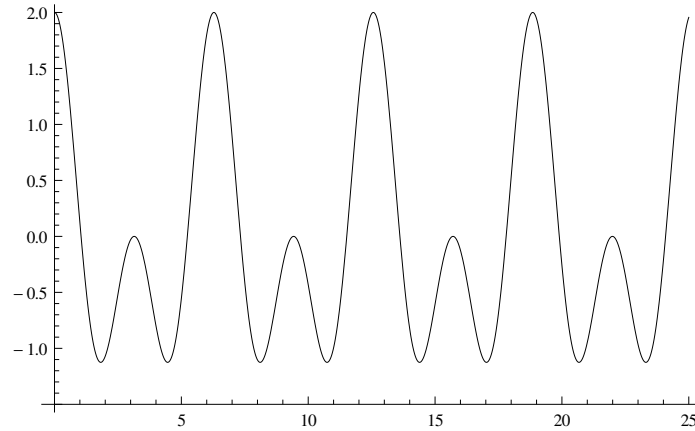
Figure 4.1: The surface profile for the solution (4.57) with $A_1 = 1$, $k = 1$ and $A_2 = \frac{1}{2}$.

We have so far studied the case when the condition (4.39) is satisfied for $m = 2$. Two different different periodic solutions are obtained. The profiles of these two solutions are shown in Figure 4.1 and Figure 4.2. They are called the Wilton ripples because they were first calculated by Wilton in 1915 for gravity-capillary waves. The curves are basically sinusoidal but with dimples either on the crests or on the troughs. Meanwhile it indicates the non-uniqueness of periodic solutions. When the
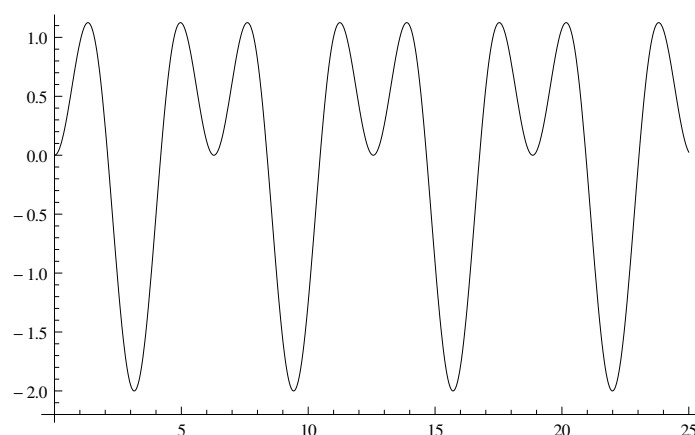
Figure 4.2: The surface profile for the solution (4.57) with $A_1 = 1$, $k = 1$ and $A_2 = -\frac{1}{2}$.

condition (4.39) is satisfied for higher value of m, there also exists more than one solution. We have seen the same properties of periodic waves in the gravity-capillary problem, whose Stokes expansions are similar to the current ones. To find solutions for $m > 3$, one need to access higher order of the Stokes expansion, which becomes quite intractable due to extremely messy computations. Therefore we shall solve the problem numerically in Section 4.2 .

4.2   Periodic Waves

4.2.1   Symmetric waves in infinite depth

Nonlinear solutions can be computed by using the numerical procedure of Section 3.1. To achieve this we need to make an appropriate initial guess for $(a_0, a_1, ..., a_{N-2}, B, \gamma)$ in the Newton's iterations. The value of k can be predicted by (3.45) and (4.39) for different values of m. Then the value of γ can be easily computed by using (3.28). We choose $a_1 = -0.1$ and set all the remaining coefficients equal to zero. This completes the initial guess which leads to a nonlinear solution by Newton's iterations. In deep water, as explained in [51], there exist many different families of periodic waves with dimples on their free-surface. This is confirmed by the present numerical

results. Some typical free-surface profiles are presented in Figure 4.3. These results show that more and more dimples appear on the free surface profiles as m increases.
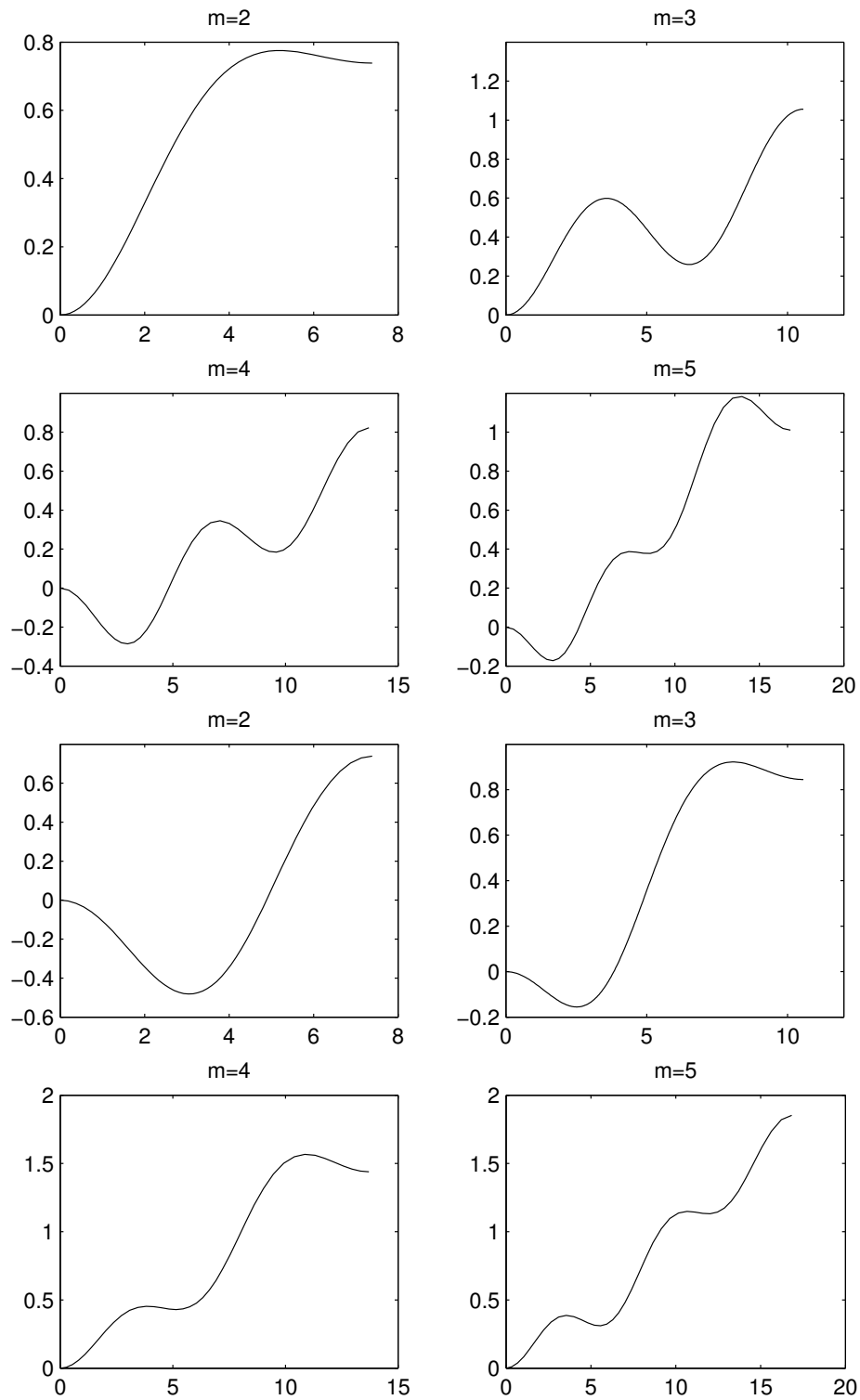

Figure 4.3: Typical surface profiles for order $m = 2, 3, 4, 5$ in deep water. Only half of a wavelength of the waves is shown.

4.2.2 Symmetric waves in finite depth

The infinite depth numerical results of Figure 4.3 can be extended to finite depth by assuming $r_0 \neq 0$. As expected by analogy with the infinite depth results, there are again dimples on the free surface. However as the wavelength l increases (i.e. as r_0 in (3.21) approaches 1) these dimples tend to concentrate in the troughs of the waves (see Figure 4.4). These results suggest that the waves approach as $l \to \infty$ solitary waves characterised by a train of ripples of constant amplitude in the far field. Such waves are called generalised solitary waves to contrast then to true solitary waves which are characterised by a flat free surface in the far field.

4.3 Generalised Solitary Waves

In order to confirm the existence of generalised solitary waves, we repeated the computations of Figure 4.4 for larger values of l and various values of β and A. We present in Figure 4.5 values of $1/F^2$ versus l for $\beta = 0.07$ and $A = 0.14$. These results illustrate that there are an infinite number of branches of solutions which approach parallel curves as $l \to \infty$. Two such branches are shown in Figure 4.5. To explain this property we present in Figure 4.6 two profiles corresponding to the points P_1 and P_2 in Figure 4.5. We see that these two profiles are very close to each other except that the one corresponding to P_2 has one more "wavelength of ripples" in the far field. This implies that the distance between the two parallel curves of Figure 4.5 is approximately equal to twice the wavelength of the ripples in the tail of the waves (this becomes exact as $l \to \infty$). Generalised solitary waves are then obtained by jumping from one curve (such as those in Figure 4.5) to the next as we take the limit $l \to \infty$. After each jump, two more wavelengths of the ripples appear (one on the right and one on the left). In the limit $l \to \infty$, we obtain a generalised solitary wave characterised by infinite train of ripples in the far field. For each value of β,
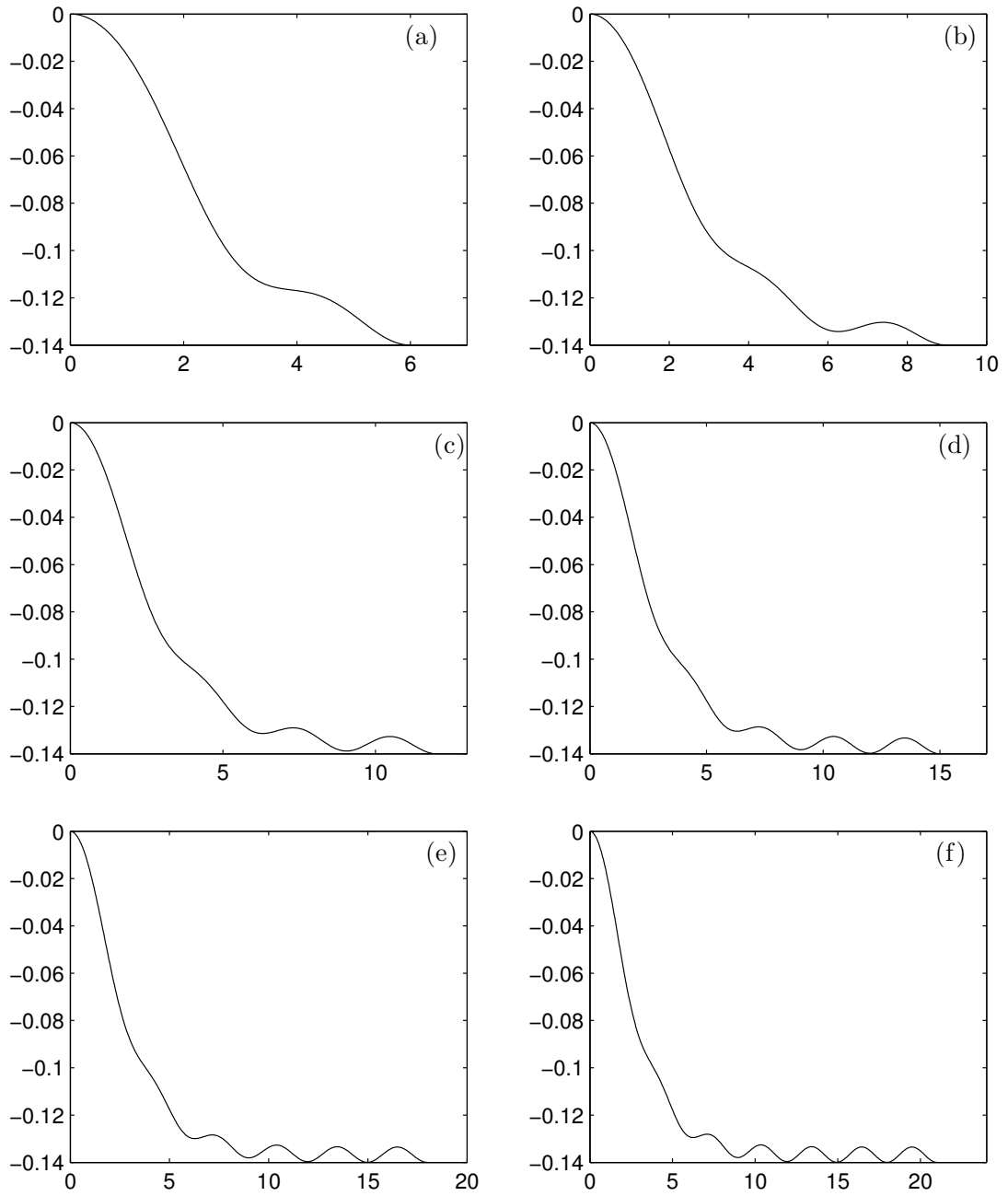
Figure 4.4: Surface profiles in the case of finite depth for $\beta = 0.07$ and $A = 0.14$: the half wavelength $l/2$ equals (a) 6, (b) 9, (c) 12, (d) 15, (e) 18, (f) 21. Only half of a wavelength of the waves is shown.

these generalised solitary waves form a two-parameter family of solutions.

We consider a particular family for $89 < l < 95$ which is shown in Figure 4.7 (since l is large, it provides an approximation of generalised solitary waves). Two sub-branches of solutions are discovered. The intersection illustrates the fact that it is possible to have two different generalised solitary waves with same wavelength
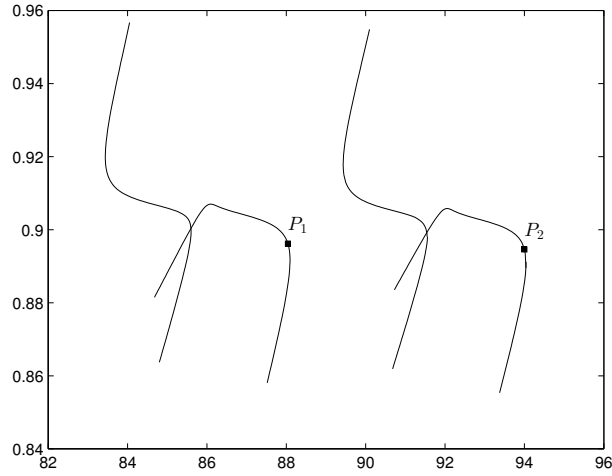
Figure 4.5: The graphs of $1/F^2$ versus the wavelength l for $\beta = 0.07$ and $A = 0.14$.
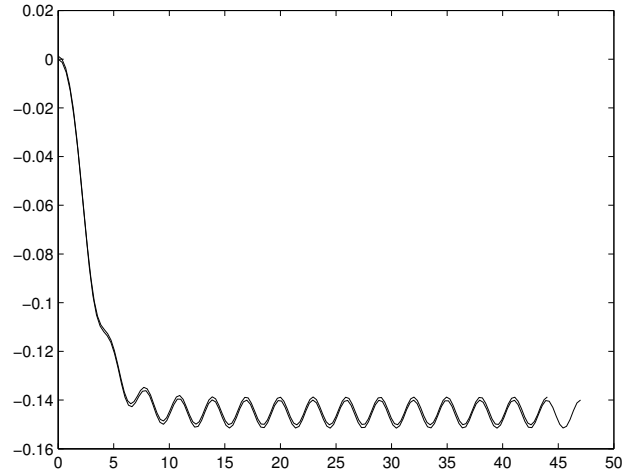
Figure 4.6: The two profiles corresponding to P_1 and P_2 in Figure 4.5. The vertical scale has been exaggerated to show the difference of these two profiles.

and same Froude number. Some typical free surface profiles for the left sub-branch and the right sub-branch are shown in Figure 4.8 and Figure 4.9 respectively. From Figure 4.8, it can be seen that waves start with large ripples and then evolve to generalised solitary waves with small ripples which enlarges again in the later stage. From Figure 4.9, one can observe first very large ripples which become smaller and then larger again. The main difference is that the right-end point of the solutions from the left branch is a trough whereas the one from the right branch is a crest.

Alternatively we may impose a different condition instead of (3.26). For example,

Figure 4.7: The graph of $1/F^2$ versus the wavelength for a particular family when $\beta = 0.07$ and $A = 0.14$.

Figure 4.8: Typical surface profiles from the left branch. Only half of a wavelength is shown.

we can fix the value u_0 of the velocity at $x = 0$. This condition was already considered in [21] for the gravity-capillary problem. Accordingly, we replace equation (3.26) by

$$\tau(0,0) = \ln u_0. \tag{4.59}$$

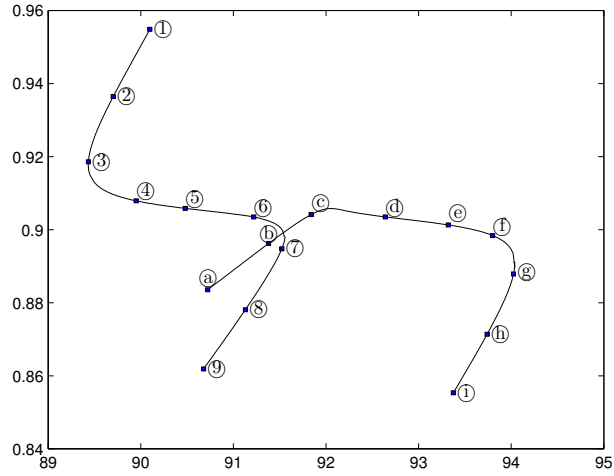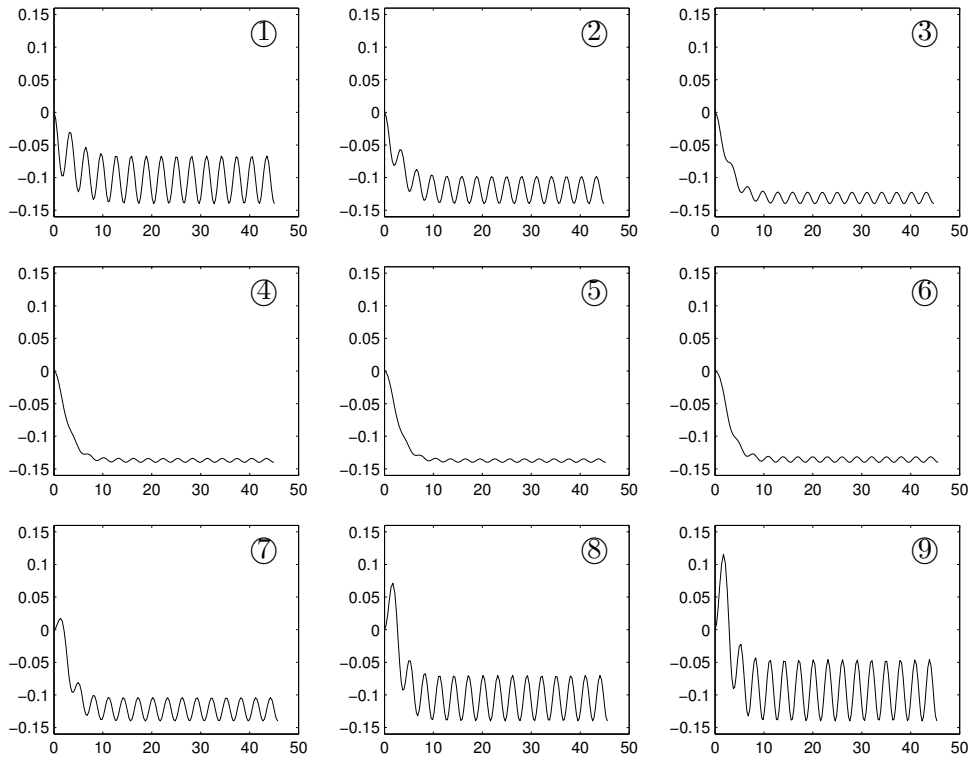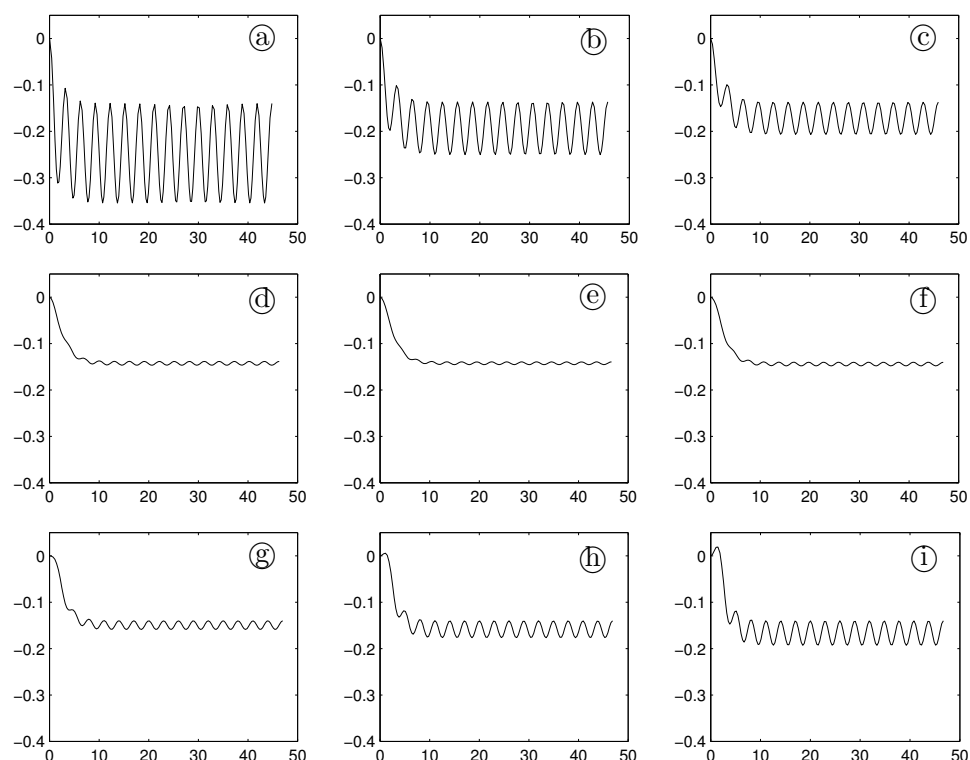Figure 4.9: Typical surface profiles from the right branch. Only half of a wavelength is shown.

We present values of $1/F^2$ versus l for $u_0 = 0.97$ and $\beta = 0.07$ in Figure 4.10. The value of $1/F^2$ changes little as the wavelength varies since the vertical scaling is small. The function is monotonically decreasing in each family and will eventually converges to a limit as the wavelength tends to infinity. Unlike what we have seen in Figure 4.7, we have only found a single branch rather than two. From two consecutive families in Figure 4.10, one corresponds to the waves whose right-end point is a crest whilst the other one has a trough as its right-end point. Similar results are found in the case of gravity-capillary waves (see Section 4.4).

We note that solitary waves in the absence of the elastic sheet exists up to some critical value of A of the order 0.83 at which a limiting configuration is reached. Therefore our results for $A = 0.14$ are of moderate height and can be described as weakly nonlinear.

The ripples in the tail of generalised solitary waves are of questionable physical validity because they occur on both sides and therefore do not satisfy the radiation
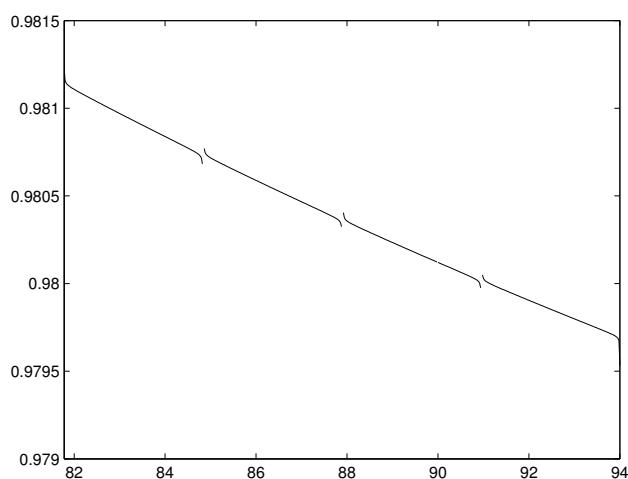
Figure 4.10: Value of $1/F^2$ versus the wavelength when $u_0 = 0.97$ and $\beta = 0.07$.

condition. Therefore an important question is whether or not the parameters can be chosen so that the amplitude of the ripples vanish. To investigate this question we choose the absolute value of the curvature of the free surface at $\phi_{N-1} = l/2$ as a measure of the amplitude of the ripples in the tail. We denote this parameter by J. Values of J versus β for $l = 99.58$ and $F = 1.03$ are shown in Figure 4.11. These results and similar ones obtained for other values of l and A strongly suggest that $J \neq 0$ for $\beta \neq 0$ and that there are therefore no true solitary waves (i.e. solitary waves for which the free surface is flat in the far field). A qualitatively similar result was found in [3] for gravity-capillary waves.

4.4 Comparison to the Kirchhoff-Love model

We may compare the results from the previous section to the ones produced by the KL model which is defined by (2.18). We follow the numerical procedure of Section 3.1 to simulate the solutions.

In Figure 4.12 we plot values of $1/F^2$ versus the wavelength l for $A = 0.14$ and $\beta = 0.07$. One can see that there are again two different sub-branches for each family. One slight difference is that the two curves in each family do not intersect
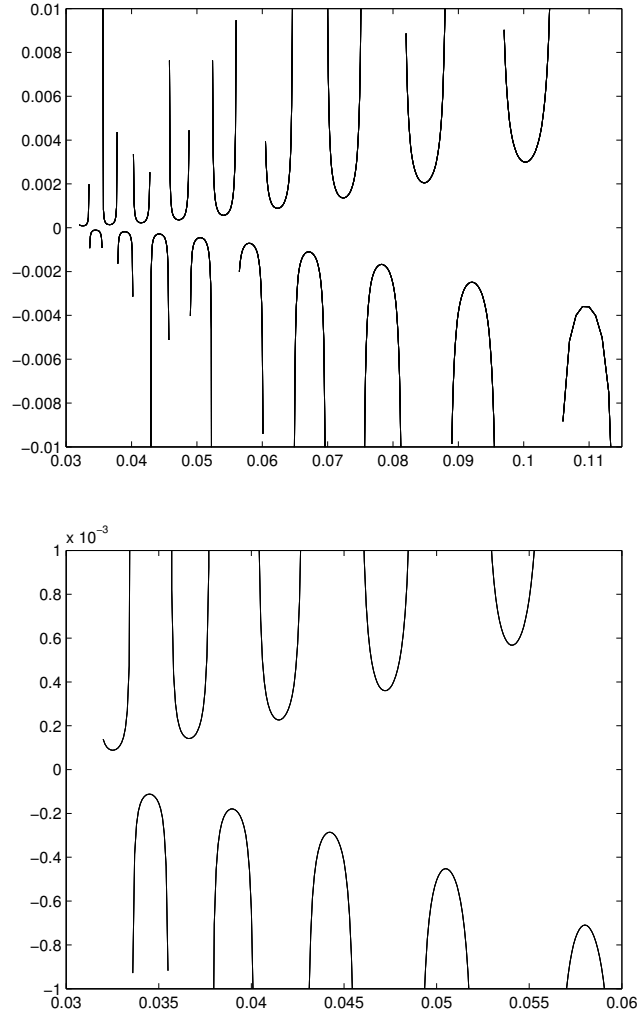
Figure 4.11: Value of the curvature κ versus β when $l = 100$ and $F = 1.03$.

in Figure 4.12 whereas they do in Figure 4.5. Apart from this, the two graphs are qualitatively similar.

Furthermore, we can also use the KL model and fix the velocity u_0 instead of A. The result is shown in Figure 4.13. This is qualitatively similar to what we have seen in Figure 4.10.

4.5 Related gravity-capillary problem

Generalised solitary waves have been found before in the study of gravity-capillary waves (see [21] and [48] for a review). We present in this section a comparison of our
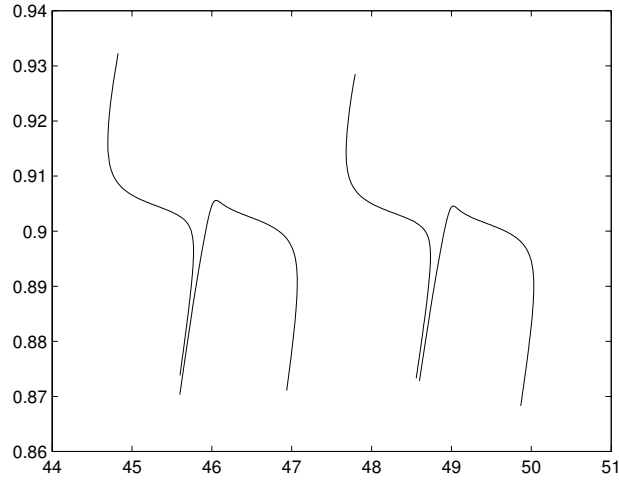
Figure 4.12: Value of $1/F^2$ versus the wavelength when $A = 0.14$ and $\beta = 0.07$.
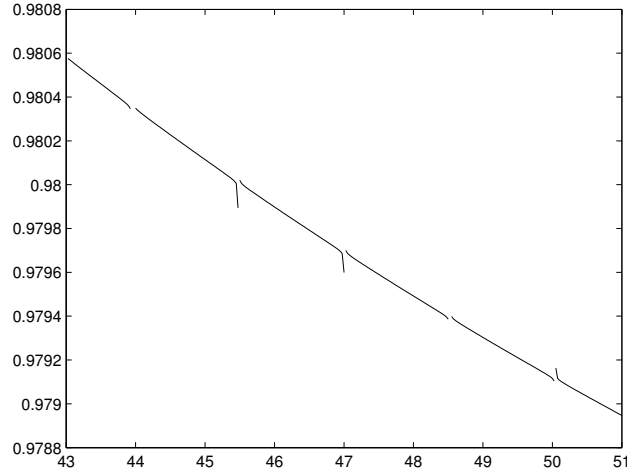
Figure 4.13: Value of $1/F^2$ versus the wavelength when $u_0 = 0.97$ and $\beta = 0.07$.

results for flexural-gravity waves with those of gravity-capillary waves.

For gravity-capillary waves, (3.5) is replaced by

$$p = -T\kappa, \tag{4.60}$$

where T is the surface tension. Using again c as the reference velocity and Q/c as the reference length, (3.18) becomes

$$\frac{1}{2}e^{2\tau} + \frac{1}{F^2}\int_0^\phi e^{-\tau(\varphi)}\sin[\theta(\varphi)]d\varphi - \bar{\tau}\kappa = B, \tag{4.61}$$

where

$$\bar{\tau} = \frac{T}{\rho Q c} \tag{4.62}$$

is the Bond number.

The remaining equatoins are unchanged and numerical results can be obtained by the procedure of Section 3.1. Values of $1/F^2$ versus l are presented in Figure 4.14 and Figure 4.15. The results from Figure 4.15 agree with those found in [21]. Two sub-branches are again found in Figure 4.14. These results are qualitatively similar to those obtained in the previous sections for flexural-gravity waves.
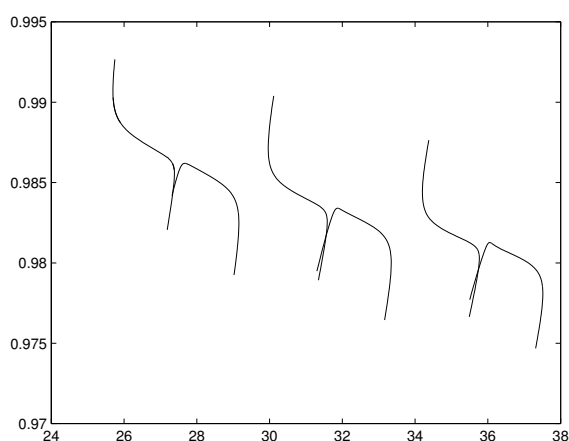
Figure 4.14: Value of F versus l when $A = 0.14$ and $\tau = 0.24$.
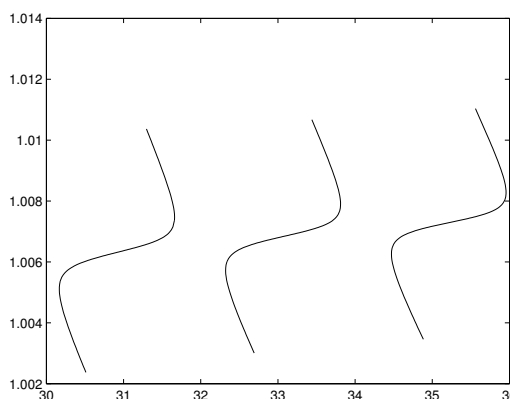
Figure 4.15: Value of F versus l when $u_0 = 0.97$ and $\tau = 0.24$.

4.5.1   Flexural-Gravity-Capillary waves

In the previous section, we have studied generalised solitary waves. Unlike true
solitary waves, these waves have infinitely many ripples of constant amplitude in the
far field. It has been found that the amplitude of the ripples in the far field is always
non-zero for both flexural-gravity waves and gravity-capillary waves. In this section,
we want to investigate how these waves behave with the presence of both the flexural
term and the surface tension. Of particular interest is whether or not the ripples in
the far field can be eliminated. We recall the governing equations

$$\nabla^2 \phi = 0, \qquad -h < y < \eta(x), \qquad (4.63)$$

$$\phi_y = \phi_x \eta_x, \qquad \text{on } y = \eta(x), \qquad (4.64)$$

$$\frac{1}{2}(\phi_x^2 + \phi_y^2) + gy + \frac{D}{\rho}(\kappa_{ss} + \frac{1}{2}\kappa^3) - \frac{T}{\rho}\kappa = B, \qquad \text{on } y = \eta(x), \qquad (4.65)$$

$$\phi_y = 0, \qquad \text{on } y = -h. \qquad (4.66)$$

We continue to use the numerical scheme presented in Section 3.1. In terms of the
dimensionless variables, the dynamics boundary condition becomes

$$\frac{1}{2}e^{2\tau} + \frac{1}{F^2}\int_0^\phi e^{-\tau(\varphi)}\sin\theta(\varphi)d\varphi + \beta(\kappa_{ss} + \frac{1}{2}\kappa^3) - \bar{\tau}\kappa = B, \qquad (4.67)$$

where F, β and $\bar{\tau}$ are defined in (3.19), (3.20) and (4.62) respectively. We follow the
same numerical procedure as shown in Section 4.3. As we have seen in Section 4.3,
there exists many different families of generalised solitary waves and each one has
two sub-branches in the case of flexural-gravity waves. When the flexural term and
the surface tension are both present, we have found similar results which are shown
in Figure 4.16. The flash-shape curves correspond to the waves whose right-end point
is a trough and the n-shape ones to the waves whose right-end point is a crest. The
outcomes are qualitatively similar to those we have found in Section 4.3.
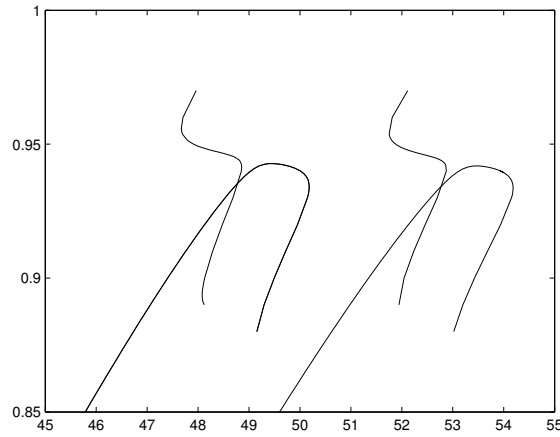
Figure 4.16: Value of $1/F^2$ versus the wavelength when $\bar{\tau} = 0.1$ and $\beta = 0.09$.

Next we compute the value of curvature of the end point of these generalised solitary waves and present the value of the curvature versus the Bond number $\bar{\tau}$ in Figure 4.17. When the Bond number is negative (i.e. surface tension corresponds to compression) the curvature is very close to zero but never equals zero since only n-shape and u-shape curves have been observed. When the Bond number becomes positive and close to zero, the effect of surface tension is relatively small and the flexural term dominates. The curves obtained are quite similar to those found in Figure 4.11. As the Bond number increases, the surface tension dominates and the curves behave like those of gravity-capillary waves presented in [3].

As can be seen from Figure 4.17, the curvature is always different from zero. With addition of the surface tension, the ripples of the generalised solitary waves the far field still cannot be removed. In other words, true elevation solitary waves do not exist with surface tension and the flexural term both present.

4.6   Conclusion

We have presented numerical computations of nonlinear periodic waves and of generalised solitary waves propagating under an elastic sheet. Most of the results
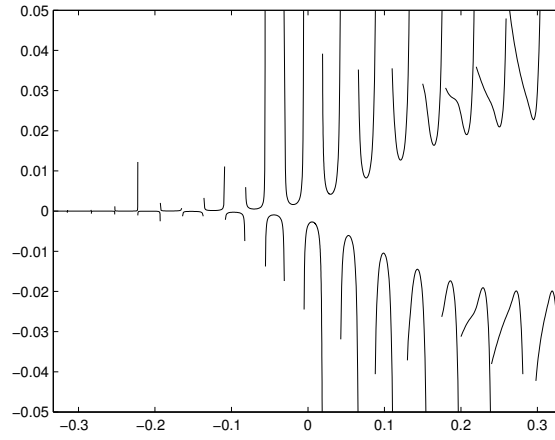
Figure 4.17: Value of curvature versus the Bond number when $l = 100$, $F = 1.03$ and $\beta = 0.09$.

were obtained for the Plotnikov-Toland model. We have provided numerical evidence that there are no true solitary waves (i.e. solitary waves with a flat free surface in the far field). Our findings were then compared with those obtained with the simplified KL model and with computations of gravity-capillary waves. In the last part of this chapter, we add the surface tension to the flexural-gravity system to investigate whether the ripples can be eliminated. However the answer is negative.

Chapter 5

Surface waves due to a moving disturbance

In this chapter, we consider hydroelastic flows generated by a disturbance moving with a constant velocity U. The moving disturbance can be a vehicle, a heavy object or a distribution of pressure. We use the formulation shown in Section 2.2 and choose the disturbance to be a pressure distribution. In Section 5.1, the linear model introduced in (2.22) was used with a perturbation method and Fourier transforms to solve this problem. We presented the results with a discussion of the validation of the linear theory in Section 5.1.4. Linear gravity-capillary flows due to a steadily moving pressure have been considered by [48]. As we shall see, the properties of linear waves beneath an ice sheet are similar to those of gravity-capillary waves. Then we use in Section 5.2 the numerical method presented in Section 3.1 to study the nonlinear model.
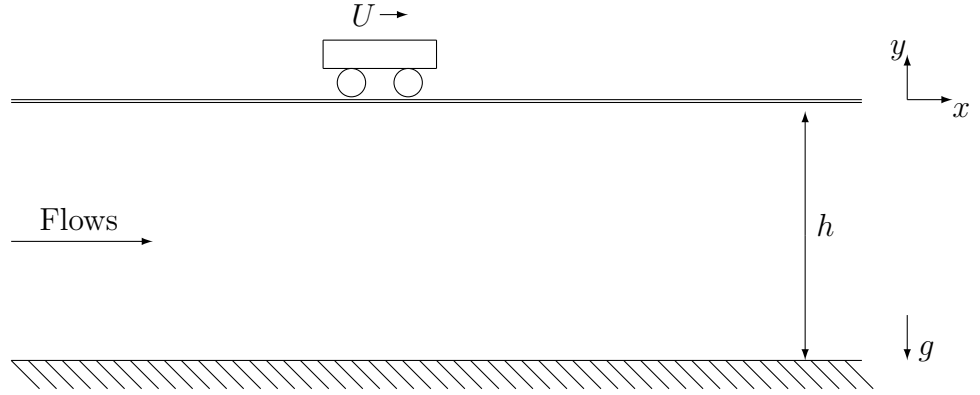
Figure 5.1: The two-dimensional problem of waves beneath an elastic sheet due to a moving disturbance.

5.1   Linear theory

5.1.1   Formulation

We introduce a cartesian coordinate system with the x-axis parallel to the horizontal and the y-axis upwards. The pressure exerted by the ice sheet is given by

$$p = D\eta_{xxxx}. \tag{5.1}$$

where D is the flexural rigidity of the ice (see (2.19)). We introduce the potential function ϕ and the streamfunction ψ. We choose $\psi = 0$ on the free-surface and $\phi = 0$ where $x = 0$. The flow configuration is shown in Figure 5.1. We assume that the disturbance moves with a constant velocity U and we choose a frame of reference such that the flow is steady. The disturbance is modelled by a pressure distribution $P(x)$. Then $\phi(x,y)$ and $\eta(x)$ satisfy the following equations

$$\nabla^2\phi = 0 \qquad\qquad -h < y < \eta(x), \tag{5.2}$$

$$\phi_y = \phi_x\eta_x \qquad\qquad \text{on } y = \eta(x), \tag{5.3}$$

$$\frac{1}{2}(\phi_x^2 + \phi_y^2) + gy + \frac{D}{\rho}\eta_{xxxx} + \frac{\epsilon P(x)}{\rho} = B \qquad\qquad \text{on } y = \eta(x), \tag{5.4}$$

$$\phi_y = 0 \qquad\qquad \text{on } y = -h. \tag{5.5}$$

Here h is the depth. Equation (5.5) is the kinematic boundary condition on the bottom channel. $y = \eta(x)$ describes the free-surface. The equations (5.3) and (5.4) are the kinematic and the dynamic boundary conditions on the free-surface respectively. The parameter ϵ measures the size of the pressure $P(x)$. We choose $y = 0$ as the constant level of the free-surface corresponding to zero pressure. It leads to

$$B = \frac{1}{2}U^2. \tag{5.6}$$

since the flow is then uniform with constant velocity U.

5.1.2 Case of finite depth

We notice that $\phi(x) = Ux$, $\eta(x) = 0$ is an exact solution to the previous equations when ϵ is zero. We consider a small perturbation by writing the solutions in powers of ϵ and get the linear solution if we retain only the terms of order ϵ. Hence

$$\phi(x, y) = Ux + \epsilon\phi_1(x, y) + O(\epsilon^2), \tag{5.7}$$

$$\eta(x) = \epsilon\eta_1(x) + O(\epsilon^2). \tag{5.8}$$

Substituting (5.7) and (5.8) into (5.2)-(5.5) gives

$$\phi_{1xx} + \phi_{1yy} = 0, \quad -h < y < 0, \tag{5.9}$$

$$\phi_{1y} = U\eta_{1x}, \quad \text{on } y = 0, \tag{5.10}$$

$$U\phi_{1x} + g\eta_1 + \frac{D}{\rho}\eta_{1xxxx} + \frac{P(x)}{\rho} = 0, \text{ on } y = 0, \tag{5.11}$$

$$\phi_{1y} = 0, \quad \text{on } y = -h. \tag{5.12}$$

When $P(x) = 0$, this system reduces to (2.27)-(2.30) with $c = U$. Thus the

solution of (5.9)-(5.12) is non-unique in the case of non-zero pressure distribution since one can always add to it a multiple of a solution of (2.27)-(2.30) when U is greater than the minimum phase speed. By solving the problem with dissipation and then taking the limit as the coefficient of dissipation tends to zero, one can obtain a unique solution that satisfies the radiation condition which requires that no energy comes in from infinity as shown in [37]. Therefore we introduce the Rayleigh viscosity μ when the pressure is non-zero. The dynamic boundary condition (5.11) can be expressed as

$$U\phi_{1x} + g\eta_1 + \frac{D}{\rho}\eta_{1xxxx} + \frac{P}{\rho} + \mu\phi_1 = 0, \quad \text{on } y = 0. \tag{5.13}$$

Using (5.10) to eliminate η_1 in (5.13) gives

$$U\phi_{1xx} + \frac{g}{U}\phi_{1y} + \frac{D}{\rho U}\phi_{1xxxxy} + \frac{P_x}{\rho} + \mu\phi_{1x} = 0 \tag{5.14}$$

Now we write ϕ_1 as the Fourier transform,

$$\phi_1(x, y) = \int_{-\infty}^{\infty} F(a, y)e^{iax}. \tag{5.15}$$

Then equations (5.9) and (5.12) become

$$F_{yy} - a^2 F = 0, \quad -h < y < 0, \tag{5.16}$$

$$F_y = 0, \quad \text{on } y = -h. \tag{5.17}$$

The solution of (5.16) and (5.17) can be written as

$$F(a, y) = A(a)\cosh a(y + h), \tag{5.18}$$

and (5.15) becomes

$$\phi_1(x) = \int_{-\infty}^{\infty} A(a) \cosh(a(y+h)) e^{iax} dx, \tag{5.19}$$

where $A(a)$ is an arbitrary function of a. Then we write the pressure distribution $P(x)$ as the Fourier Transform,

$$P(x) = \int_{-\infty}^{\infty} B(a) e^{iax}. \tag{5.20}$$

Then $B(a)$ is given by the inverse formula,

$$B(a) = \frac{1}{2\pi} \int_{-\infty}^{\infty} P(x) e^{-iax} dx. \tag{5.21}$$

Combining (5.14),(5.19) and (5.20) gives

$$A(a) = \frac{iB(a)}{\rho U \cosh(ah) \widetilde{D}(a)}, \tag{5.22}$$

where

$$\widetilde{D}(a) = a - \frac{g}{U^2} \tanh(ah) - \frac{Da^4}{\rho U^2} \tanh(ah) - i\mu_1, \tag{5.23}$$

with $\mu_1 = \frac{\mu}{U}$. Combining (5.22), (5.19) and (5.10) yields after integration

$$\eta_1(x) = \frac{1}{\rho U^2} \int_{-\infty}^{\infty} \frac{e^{iax} B(a) \tanh(ah)}{\widetilde{D}(a)} da. \tag{5.24}$$

We assume that $P(x)$ is an even function and so $B(a)$ is also even. A simple analysis shows that the real part of the integrand in (5.24) is even and the imaginary part is odd. Hence (5.24) can be rewritten

$$\eta_1(x) = \frac{2}{\rho U^2} \Re \int_{0}^{\infty} \frac{e^{iax} B(a) \tanh(ah)}{\widetilde{D}(a)} da. \tag{5.25}$$

where we denote $\Re(.)$ by the real part of a complex number. We now take the limit $\mu \to 0$.

If $\Re(\widetilde{D}(a)) \neq 0$, the limit is simply

$$\eta_1(x) = \frac{2}{\rho U^2} \Re \int_0^\infty \frac{e^{iax} B(a) \tanh(ah)}{a - \frac{g}{U^2} \tanh(ah) - \frac{Da^4}{\rho U^2} \tanh(ah)} da, \qquad (5.26)$$

It can be easily calculated by numerical integration such as the trapezoidal rule. We note that the free-surface is flat in the far field in this case (i.e. no wave train as $|x| \to \infty$).

If $\Re(\widetilde{D}(a)) = 0$ for some values of a, we need to take more care in taking the limit and the integral must be evaluated differently. Let us denote by $a^* \in \mathbb{R}$ the values of a satisfying

$$a^* - \frac{g}{U^2} \tanh(a^*h) - \frac{Da^{*4}}{\rho U^2} \tanh(a^*h) = 0. \qquad (5.27)$$

As shown in Chapter 2 the phase velocity c defined by (2.43) always admits a minimum $c_{\min}$. Therefore when $U > c_{\min}$, there are two real positive values a_1^* and a_2^* of a^*. Without losing generality, we let $0 < a_1^* < a_2^*$. We note that $-a_1^*$ and $-a_2^*$ are also two solutions to $\Re(\widetilde{D}(a)) = 0$ since $\Re(\widetilde{D}(a))$ is an odd function. Then we rewrite $\Re(\widetilde{D}(a))$ in the following form

$$\widetilde{D}(a) = \frac{a}{U^2}(U^2 - \widetilde{C}^2(a)) - i\mu_1, \qquad (5.28)$$

where

$$\widetilde{C}^2(a) = \left(\frac{g}{a} + \frac{D}{\rho} a^3\right) \tanh(ah). \qquad (5.29)$$

If a^* is a solution to $\Re(\widetilde{D}(a)) = 0$, then we want to seek a solution to $\widetilde{D}(a)$ by writing

$$a = a^* + \widetilde{\epsilon}(a^*), \qquad (5.30)$$

where $|\widetilde{\epsilon}(a^*)|$ is small. Expanding $\widetilde{D}(a^* + \widetilde{\epsilon}(a^*))$ in a Taylor expansion, we obtain

$$\widetilde{\epsilon}(a^*) = i\epsilon_0(a^*) = -\frac{i\mu_1 U}{2a^*\widetilde{C}'(a^*)}. \tag{5.31}$$

Now we introduce the complex plane $\xi = a + ib$ and consider the following complex integral

$$\frac{2}{\rho U^2} \int_C \frac{e^{i\xi x} B(\xi) \tanh(\xi h)}{\widetilde{D}(\xi)} d\xi \tag{5.32}$$

where C is a contour consisting of the real axis and a semi-circle with infinite radius. Since $\widetilde{C}'(a_1^*) < 0$ and $\widetilde{C}'(a_2^*) > 0$, (5.31) implies $\epsilon_0(a_1^*) > 0$ and $\epsilon_0(a_2^*) < 0$. Thus the pole $a_1^* + i\epsilon_0(a_1^*)$ is in the upper-half of the complex plane whereas $a_2^* + i\epsilon_0(a_2^*)$ is in the lower-half plane.

We denote the integrand in (5.32) by

$$F(\xi) = \frac{2}{\rho U^2} \frac{e^{i\xi x} B(\xi) \tanh(\xi h)}{\widetilde{D}(\xi)}. \tag{5.33}$$

Hence by the residue theorem, (5.32) can be evaluated. This gives

$$\int_{C^+} F(\xi) = 2i\pi R_I^+ + 2i\pi R(F, a_1^* + i\epsilon_0(a_1^*)) +$$

$$2i\pi R(F, -a_1^* + i\epsilon_0(a_1^*)) \quad \text{for } x > 0, \tag{5.34}$$

and

$$\int_{C^-} F(\xi) = -2i\pi R_I^- - 2i\pi R(F, a_2^* - i\epsilon_0(a_2^*))$$

$$- 2i\pi R(F, -a_2^* - i\epsilon_0(a_2^*)) \quad \text{for } x < 0, \tag{5.35}$$

where $R(F, p)$ denotes the residue of $F(\xi)$ at pole p. R_I^+ and R_I^- are the sums of remaining residues in the upper-half imaginary axis and in the lower-half imaginary

axis respectively. We rewrite

$$F(\xi) = \frac{N(\xi)}{\widetilde{D}(\xi)}. \tag{5.36}$$

Then the residue at pole p can be computed as

$$R(F, p) = \frac{N(p)}{\widetilde{D}'(p)}. \tag{5.37}$$

We note that $2\eta_1(x)$ equals the real part of (5.32) by comparing it to (5.25). Combining (5.37), (5.34) and (5.35) yields

$$\eta_1(x) = \Re(i\pi R_I^+) + \frac{2\pi}{\rho U} \frac{B(a_1^*)\tanh(a_1^* h)}{a_1^* \widetilde{C}'(a_1^*)} \sin(a_1^* x) \quad \text{for } x > 0, \tag{5.38}$$

$$\eta_1(x) = -\Re(i\pi R_I^-) - \frac{2\pi}{\rho U} \frac{B(a_2^*)\tanh(a_2^* h)}{a_2^* \widetilde{C}'(a_2^*)} \sin(a_2^* x) \quad \text{for } x < 0, \tag{5.39}$$

When $|x| \to \infty$, $e^{i\xi x} = e^{iax} e^{-bx}$ implies that R_I^+ tends to zero for $x > 0$ and R_I^- tends to zero for $x < 0$. Hence when $|x| \to \infty$, we have

$$\eta_1(x) \approx \frac{2\pi}{\rho U} \frac{B(a_1^*)\tanh(a_1^* h)}{a_1^* \widetilde{C}'(a_1^*)} \sin(a_1^* x) \qquad \text{for } x > 0, \tag{5.40}$$

$$\eta_1(x) \approx -\frac{2\pi}{\rho U} \frac{B(a_2^*)\tanh(a_2^* h)}{a_2^* \widetilde{C}'(a_2^*)} \sin(a_2^* x) \qquad \text{for } x < 0. \tag{5.41}$$

The free-surface is characterised by a periodic wave train in the far field. The waves behave like (5.41) and (5.40) when x tends to minus infinity and plus infinity respectively. Since $a_1^* < a_2^*$, the wave of longer wavelength $2\pi/a_1^*$ occur as x tends to infinity and the wave of shorter wavelength $2\pi/a_2^*$ as x tends to minus infinity. We have seen very similar results for linear free-surface flows with surface tension generated by a moving pressure in [48].

5.1.3 Case of infinite depth

In this section, we examine the case of water of infinite depth. Now we take the limit $h \to \infty$. The computations are similar to what we have seen in section 5.1.2. (5.23) becomes

$$\widetilde{D}(a) = a - \frac{g}{U^2}\frac{|a|}{a} - \frac{Da^4}{\rho U^2}\frac{|a|}{a} - i\mu_1, \tag{5.42}$$

where the tanh factors turn out to be $|a|/a$. (5.24) reduces to

$$\eta_1(x) = \frac{2}{\rho U^2}\Re \int_0^\infty \frac{e^{iax}B(a)}{a - \frac{g}{U^2} - \frac{Da^4}{\rho U^2} - i\mu_1}da, \tag{5.43}$$

where $|a|/a$ equals 1 since a is positive. We can further rewrite $\widetilde{D}(a)$

$$\widetilde{D}(a) = a - \frac{g}{U^2} - \frac{Da^4}{\rho U^2} - i\mu_1. \tag{5.44}$$

We need to examine whether

$$\Re(\widetilde{D}(a)) = 0. \tag{5.45}$$

According to Figure 2.3, equation (5.45) admits two real solutions if $U > c_{\min}$ whereas no real solutions if $U < c_{\min}$. We define a parameter

$$f = \left(\frac{Dg^3}{\rho U^8}\right)^{\frac{1}{3}}. \tag{5.46}$$

We can immediately find that

$$\text{if } f > f_c, \text{ then } U < c_{\min}, \tag{5.47}$$

$$\text{if } f < f_c, \text{ then } U > c_{\min}, \tag{5.48}$$

where

$$f_c = \frac{3}{4^{\frac{4}{3}}} \approx 0.472. \tag{5.49}$$

When $U < c_{\min}$, there does not exist $a \in \mathbb{R}$ such that $\Re(\widetilde{D}(a)) = 0$. Then we can

take the limit $\mu_1 \to 0$. Equation (5.43) reduces to

$$\eta_1(x) = \frac{2}{\rho U^2} \Re \int_0^\infty \frac{e^{iax} B(a)}{a - \frac{g}{U^2} - \frac{Da^4}{\rho U^2}} da. \tag{5.50}$$

In this case, the function in the integrand has no singularity for $a \in \mathbb{R}$. Hence we

can evaluate the integral directly to get $\eta_1(x)$.

When $U > c_{\min}$, we need to take extra care in taking the limit of μ. We consider

the following complex integral

$$\frac{2}{\rho U^2} \int_C \frac{e^{i\xi x} B(\xi)}{\xi - \frac{g}{U^2} - \frac{D\xi^4}{\rho U^2} - i\mu_1} d\xi. \tag{5.51}$$

where C is the same contour as we defined in (5.32). Unlike what we did for the case

of finite depth, we do not use the symmetry since the real part of the denominator

of the integrand in (5.51) is not odd. Instead we consider

$$I(x) + \eta_1(x), \tag{5.52}$$

where

$$I(x) = \frac{2}{\rho U^2} \Re \int_{-\infty}^0 \frac{e^{iax} B(a)}{a - \frac{g}{U^2} - \frac{Da^4}{\rho U^2} - i\mu_1} da. \tag{5.53}$$

Then we can relate (5.51) and (5.52) by taking the limit of the radius of the semi-

circle from contour C to infinity. By using the residue theorem, (5.51) becomes

$$\frac{2}{\rho U^2} \int_C \frac{e^{i\xi x} B(\xi)}{\xi - \frac{g}{U^2} - \frac{D\xi^4}{\rho U^2} - i\mu_1} d\xi = \Omega(C)[2i\pi \sum \text{residues}], \tag{5.54}$$

where $\Omega(C)$ describes the orientation of the contour. Here $\Omega(C) = 1$ if C is anti-

clockwise and $\Omega(C) = -1$ if C is clockwise. Combining (5.52) and (5.54) yields

$$\eta_1(x) = \Omega(C)[\Re(2i\pi \sum \text{residues})] - I(x). \tag{5.55}$$

We note that there is no singularity in the denominator of (5.53) for $a < 0$. Therefore we can take the limit $\mu_1 \to 0$ and compute the value of $I(x)$. The remaining work is to compute all the residues. Unlike the gravity-capillary problem, there are two extra poles besides two real solutions of (5.45). We denote a_1^* and a_2^* by the two real roots of (5.45) and let z_+ and z_- be the other two complex conjugate roots of (5.45) with positive and negative imaginary part respectively. Then we have

$$\Omega(C)\Re(2i\pi \sum \text{residues}) = \Re(2i\pi R(F, z_+))$$
$$+ \Re(2i\pi R(F, a_1^* + i\epsilon_0(a_1^*))) \quad \text{for } x > 0 \tag{5.56}$$

and

$$\Omega(C)\Re(2i\pi \sum \text{residues}) = -\Re(2i\pi R(F, z_-))$$
$$- \Re(2i\pi R(F, a_2^* + i\epsilon_0(a_2^*))) \quad \text{for } x < 0. \tag{5.57}$$

After calulations similar to those presented in Section 5.1.2, we obtain

$$\Re(2i\pi R(F, a_1^* + i\epsilon_0(a_1^*))) = \frac{2\pi}{\rho U} \frac{B(a_1^*)}{a_1^* \widetilde{C}'(a_1^*)} \sin(a_1^* x), \tag{5.58}$$

$$\Re(2i\pi R(F, a_2^* + i\epsilon_0(a_2^*))) = \frac{2\pi}{\rho U} \frac{B(a_2^*)}{a_2^* \widetilde{C}'(a_2^*)} \sin(a_2^* x). \tag{5.59}$$

The extra poles z_+ and z_- play an important role in the computation and cannot be neglected. We have to include the contribution of $R(F, z_+)$ and $R(F, z_-)$ since z_+ and z_- are complex, i.e. far away from the real axis, we can take the limit $\mu_1 \to 0$ and use elementary residue calculus. In this case, there are four simple poles $\widetilde{D}(a) = 0$.

With further computations, we have

$$R(F, z_+) = -\frac{2}{D} \frac{e^{iz_+ + x} B(z_+)}{(z_+ - a_1^*)(z_+^* - a_2^*)(z_+ - z_-)}, \tag{5.60}$$

$$R(F, z_-) = -\frac{2}{D} \frac{e^{iz_- - x} B(z_-)}{(z_- - a_1^*)(z_-^* - a_2^*)(z_- - z_+)}. \tag{5.61}$$

The free-surface is characterised by (5.56), (5.58), (5.60) for $x > 0$ and by (5.57), (5.59), (5.61) for $x < 0$.

5.1.4   Discussion of the results

We discuss the results in the case of infinite depth. i.e. $h \to \infty$. Here we choose $|\epsilon| = 0.001$ and the following expression for the moving pressure

$$P(x) = \frac{\rho U^2}{2} \exp(-\frac{4g^2 x^2}{U^4}). \tag{5.62}$$

When $U < c_{\min}$, the free-surface is characterised by (5.50) and is shown in Figure 5.2. It is characterised by decaying oscillations in the far field.
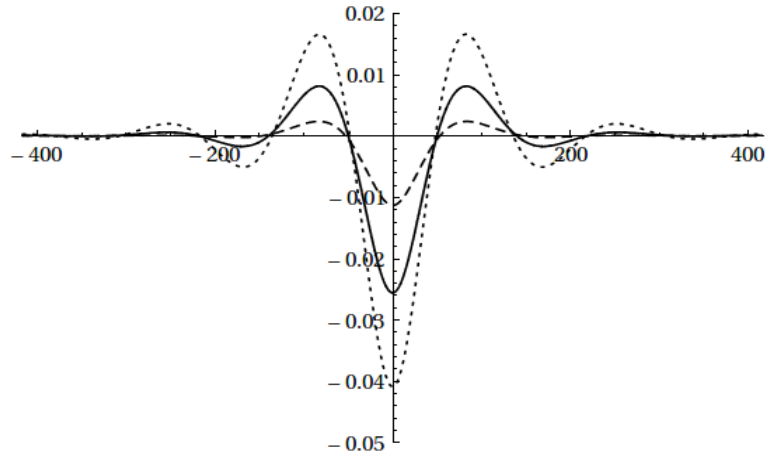

Figure 5.2: Free-surface profile in the case of infinite depth for $f = 0.6$ (dotted line), $f = 0.7$ (solid line) and $f = 1$ (dashed line).

It is interesting to find out how $\eta(0)$ behaves when $f \to f_c^+$. Hence we evaluate the integral (5.50) when $x = 0$ for different values of f and plot it in a single graph (see

Figure 5.3). As can be seen from the figure, the amplitude blows up as f approaches the left bound that is the critical value $f_c \approx 0.472$. However it contradicts the assumption that the amplitude remains small in the linear theory. Hence the linear theory becomes invalid as $f \to f_c^+$.
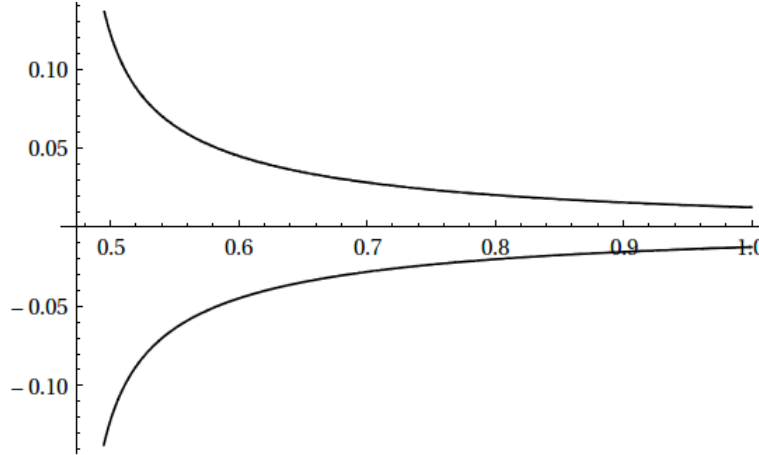

Figure 5.3: Values of $\eta(0)$ versus f for pressure distribution (5.62) with $\epsilon = 0.001$ (lower curve) and $\epsilon = -0.001$ (upper curve).

When $U > c_{\min}$, there are two real values a_1^* and a_2^* of a such that

$$a^* - \frac{g}{U^2} - \frac{Da^{*4}}{\rho U^2} = 0. \tag{5.63}$$

Then the free-surface is described by (5.53). We use (5.56),(5.58),(5.60) to compute the free-surface for $x > 0$ and (5.57), (5.59), (5.61) for $x < 0$. Several graphs for different values of f are shown in Figure 5.4.

Combining (5.50)-(5.61), we can derive that $\eta_1(x)$ is continuous for $x < 0$, $x > 0$ and $x = 0$. i.e. $\eta_1(x)$ is continuous everywhere. However, there is a discontinuity in the derivative of η_1 when $x = 0$. This is because we used linear theory in the kinetic boundary condition (5.4) which implies that $\phi_y = 0 + O(\epsilon)$ and then ϕ_{1y} becomes discontinuous when $x = 0$. The problem will not happen if we use a non-linear theory (see Section 5.2).

In the limit $f \to f_c^-$, the two real roots coincide and it implies that $\widetilde{C}'(a_1^*) = \widetilde{C}'(a_2^*) = 0$. Following (5.55) and (5.56), it shows that the magnitude of the solutions
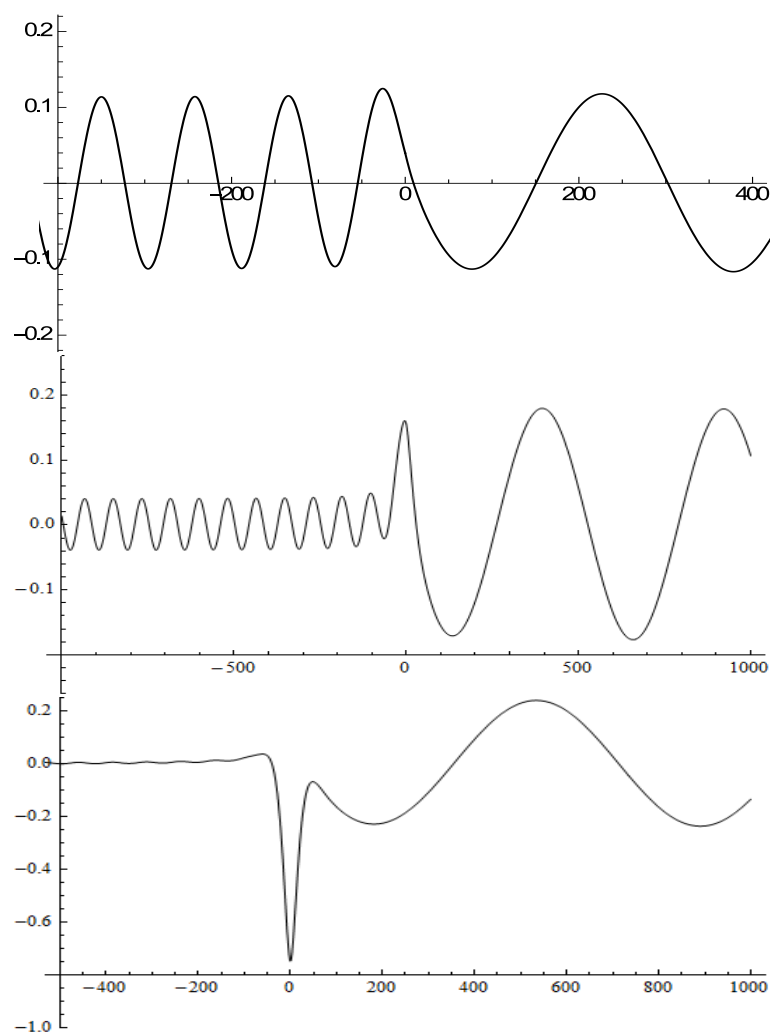
Figure 5.4: Free surface profile for $f = 0.3$ (top), $f = 0.15$ (middle) and $f = 0.1$ (bottom).

tends to infinity when $\sin(a_1^* x)$ is not equal to zero. Thus the amplitude of the waves becomes infinitely large and the linear theory breaks down when f tends to f_c^-.

The linear theory is not valid in the neighbourhood of $f = f_c$. A non-linear theory needs to be used to investigate what happens as $f \to f_c$. This is achieved in Section 5.2 .
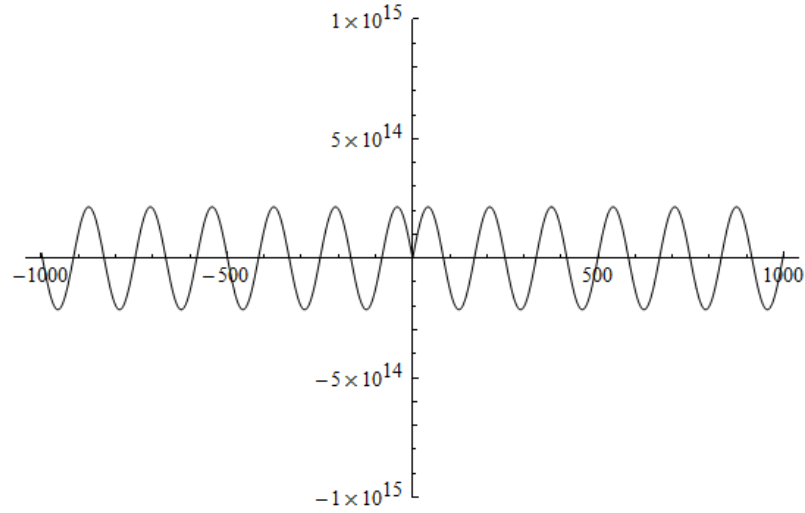
Figure 5.5: Free surface profile when f is close to f_c.

5.2 Nonlinear theory

In Section 5.1 we investigated the problem by using the linear model together with a perturbation method and Fourier transforms. It was found that the linear theory breaks down when f defined in (5.46) reaches its critical value (see Figure 5.3). In order to study what happens in that case, we need to use a nonlinear theory which has been presented in Chapter 4. We especially focus on the case in infinite depth and $U < c_{\min}$. We recall that the governing equations are

$$\nabla^2 \phi = 0 \qquad\qquad y < \eta(x), \qquad (5.64)$$

$$\phi_y = \phi_x \eta_x \qquad\qquad \text{at } y = \eta(x), \qquad (5.65)$$

$$\frac{1}{2}(\phi_x^2 + \phi_y^2) + \gamma y + [\kappa_{ss} + \frac{1}{2}\kappa^3] + P(x) = B \qquad\qquad \text{at } y = \eta(x), \qquad (5.66)$$

$$\phi_y = 0 \qquad\qquad \text{as } y \to -\infty, \qquad (5.67)$$

where we have used c, $(D/\rho c^2)^{\frac{1}{3}}$ as the reference velocity and the reference length respectively. γ is defined in (3.28). $P(x)$ is the dimensionless pressure distribution exerted by a load on the elastic sheet. In all computations, we let

$$P(x) = \epsilon e^{-\frac{x^2}{16}}, \qquad (5.68)$$

where the parameter ϵ measures the size of the pressure. The readers may try other pressure distributions while the results are qualitatively similar. The numerical method introduced in Section 3.1 is still useful for the present problem by simply adding the external forcing term. We present the results of forced depression waves for the case of small forcing and large forcing in Figure 5.6 and 5.7. Unlike the linear theory introduced in Section 5.1, the value of A (defined as the value of η as $|x| \to \infty$) does not blow up but bounces back and remains finite. The linear theory fails when f is close to its critical value since an infinitely large amplitude is not physical and the problem has to be solved by using a fully non-linear numerical method as shown in this section.

As can be seen in Figure 5.6 and Figure 5.7, there exists two waves with same value of f but different amplitudes. The one with small amplitude can be calculated by perturbing the uniform stream. In other words, the waves from the lower branch are perturbations from the uniform stream (they were calculated in Section 5.1 by using the linear theory). Meanwhile, the ones from the upper branch are perturbations from the free solitary waves. These solutions can be used to compute the free solitary waves by letting $P = 0$ through the continuation method. The work will be done in Chapter 6.

Similarly, we may introduce negative ϵ to compute the forced elevation waves. We begin by perturbing the uniform stream with a negative pressure and follow the branch by using the continuation method. As shown in Figure 5.8, the curve also bounces back so the amplitude remains finite, which is different from Figure 5.3. It is interesting to discover a new type of elevation solitary wave which is shown on the top right of Figure 5.8. The bifurcation diagram for elevation solitary waves is much more complicated than the one for depression waves. We shall see this feature in Chapter 6 where the free solitary waves are studied carefully.

Figure 5.6: The values of A versus f for $\epsilon = 0.01$ (left). The wave profiles corresponding to the highlighted point on the upper branch (top right) and the one on the lower branch (bottom right).

Figure 5.7: The values of A versus f for $\epsilon = 1$ (left). The wave profiles corresponding to the highlighted point on the upper branch (top right) and the one on the lower branch (bottom right).
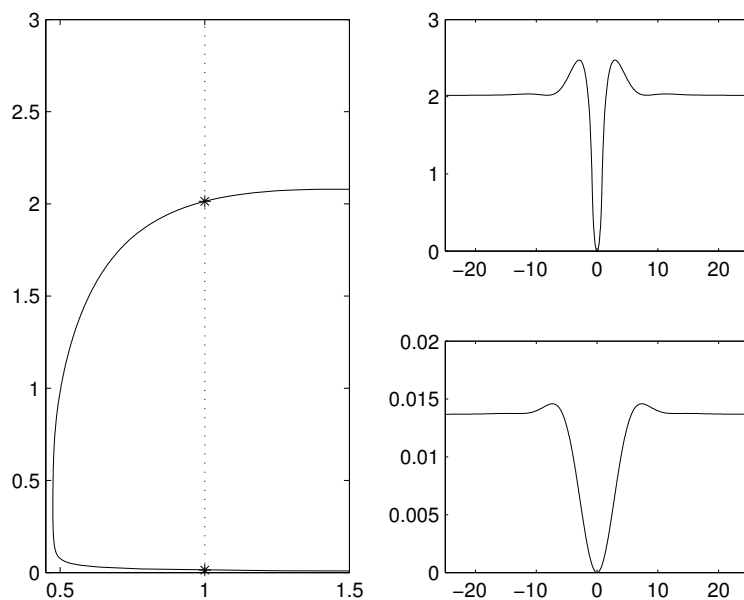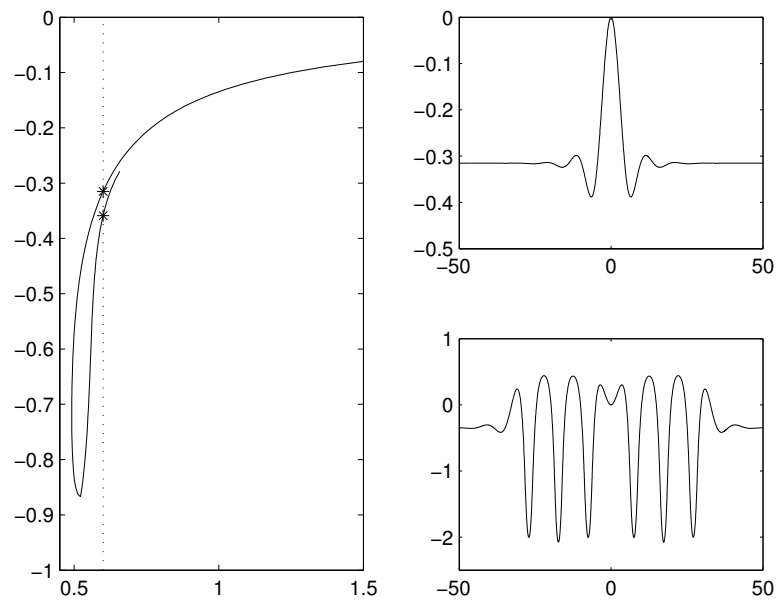
Figure 5.8: The values of A versus f for $\epsilon = -0.1$ (left). The wave profiles corresponding to the highlighted point on the upper branch (top right) and the one on the lower branch (bottom right).
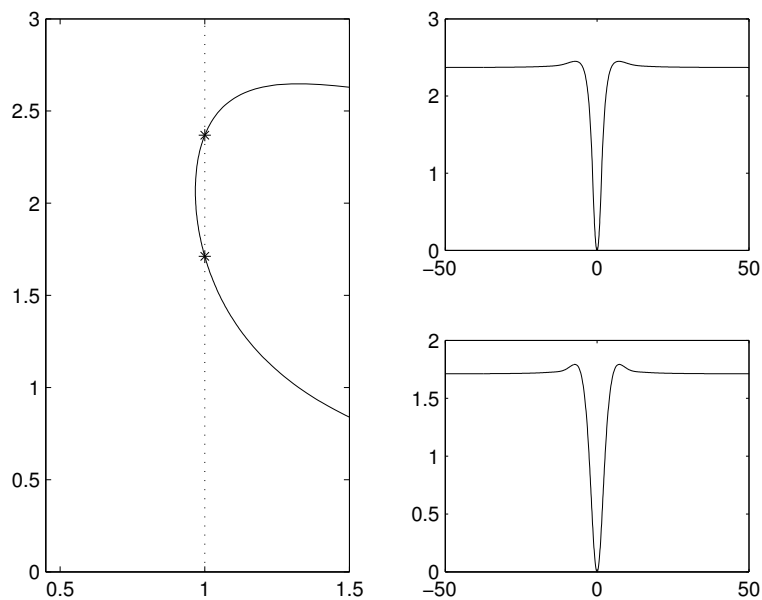
Chapter 6

Flexural solitary waves with decaying tails in deep water

6.1 Symmetric waves: numerical results

We have seen generalised solitary waves in Chapter 4. These waves have oscillatory tails of constant amplitude in the far field. In this chapter, we continue our interest in studying waves with decaying tails in the far field. The wave with a crest in the middle is called an elevation wave while a depression wave admits a trough. The numerical scheme introduced in Section 3.1 is still useful. The wavelength l is chosen to be sufficiently large so that the profile does not change as l increases. $N = 2000$ is usually used in the computations. We focus on the case of infinite depth, i.e. h tends to ∞. We continue to use the same notations as introduced in Chapter 2. The linear dispersion relation is shown in (2.47). It admits a minimum phase speed

$$c_{\min} = \frac{2}{3^{8/3}}(\frac{Dg^3}{\rho})^{\frac{1}{8}},\tag{6.1}$$

when

$$k = (\frac{\rho g}{3D})^{\frac{1}{4}}.\tag{6.2}$$

We recall from (3.27) that

$$\gamma = \left(\frac{Dg^3}{\rho c^8}\right)^{\frac{1}{3}} \tag{6.3}$$

and introduce a dimensionless parameter $\zeta = \gamma^{-3/8}$. An immediate relation between ζ and the phase speed is

$$\zeta = \frac{2}{3^{8/3}} \frac{c}{c_{\min}}. \tag{6.4}$$

In particular, the minimum phase speed is reached when $\zeta = \frac{2}{3^{8/3}} = 1.3247$. The energy of the system can be expressed in terms of the variables on the free surface as shown in (3.29). We present the values of the height A which is defined in (3.26) versus ζ in Figure 6.1 . There are two branches which correspond to elevation waves and depression waves respectively. Both branches bifurcate from finite amplitude at $\zeta = 1.3247$. For the lower branch, the amplitude decreases as c decreases. We discuss the numerical results for depression waves and elevation waves in Section 6.1.1 and Section 6.1.2 respectively.
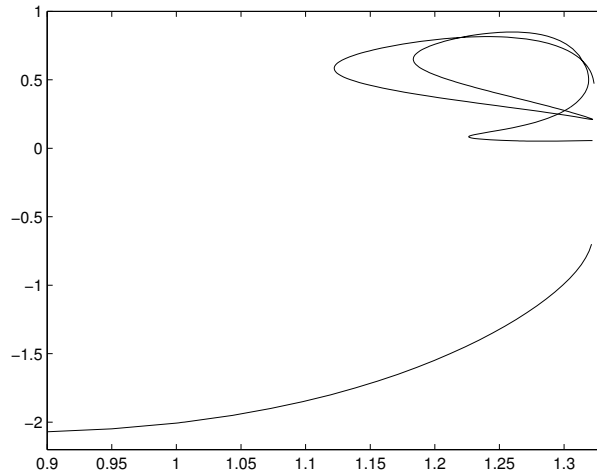

Figure 6.1: The values of A versus ζ for solitary waves. The upper branch corresponds to the elevation waves and the lower branch to the depression waves.

6.1.1   Depression waves

Depression waves bifurcate at finite amplitude from generalised solitary waves at the minimum phase speed. We present the values of the amplitude versus the values of ζ in Figure 6.2. The same results have been found in [18] and [54] by using a different numerical method.   Typical profiles for depression waves can be seen in
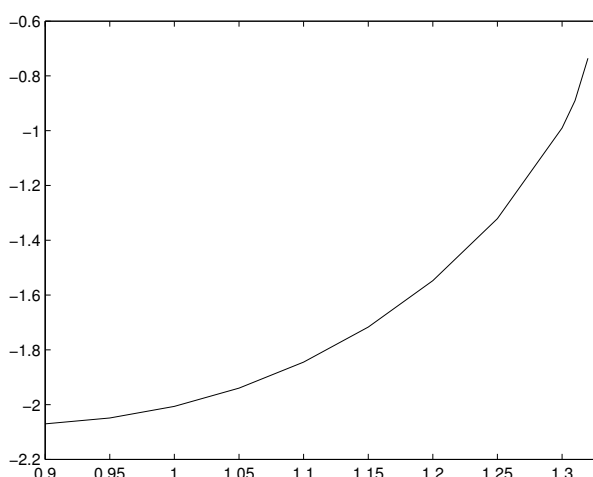
Figure 6.2: The values of A versus ζ for depression solitary waves.

Figure 6.3. As the phase speed decreases, the amplitude increases and the number of ripples decreases. The waves start to become overhanging when ζ is less than 0.7 and finally a trapped bubble is observed when $\zeta = 0$. However a very large value of N is needed for the present numerical method to remain highly accurate when ζ is small. That is why we stop at $\zeta = 0.9$. The reader is referred to [54] for overhanging waves.

We present the values of energy versus the values of ζ in Figure 6.4. We observe two turning points. The first one is near $\zeta = 1.3$ and the second one is about $\zeta = 1.05$. Following [38], the instability changes at the critical points of the Hamiltonian. i.e. it changes twice along the branch of depression waves. We expect that the depression wave is unstable when c is close to the minimum phase speed. As c decreases, the wave becomes stable beyond the right turning point in Figure 6.4 and then unstable
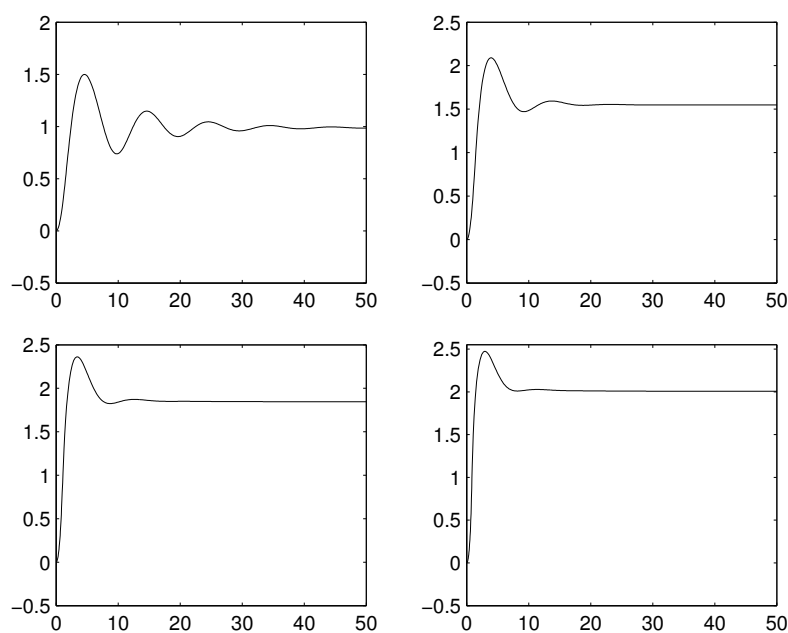
Figure 6.3: Surface profiles for depression waves with $\zeta = 1.3$ (top left), $\zeta = 1.2$ (top right), $\zeta = 1.1$ (bottom left) and $\zeta = 1$ (bottom right). Only one half of the free-surface profiles are shown.
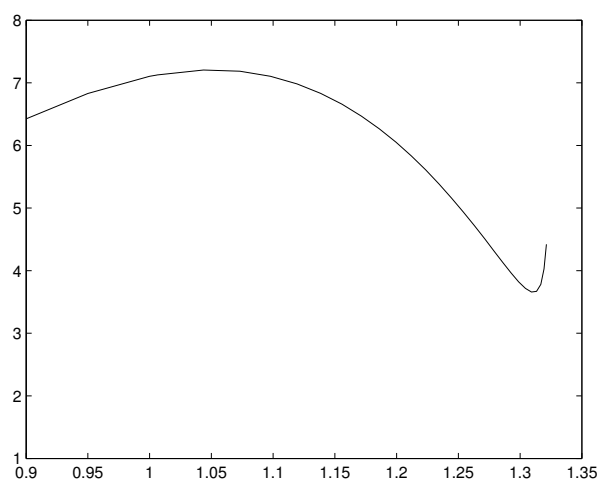
Figure 6.4: Energy versus ζ for depression solitary waves.

again beyond the left turning point. This will be studied numerically in Chapter 7.

6.1.2 Elevation waves

Unlike depression waves, the branch of elevation waves is much more complicated. A more precise view is shown in Figure 6.5.
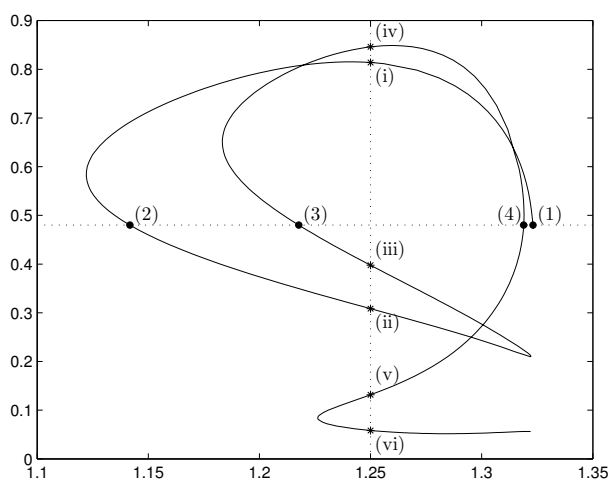
Figure 6.5: The values of A versus ζ for elevation solitary waves.

The curve starts from point (1) and its gradient changes sign several times. The intersections illustrate the fact that there exists different solitary waves with the same amplitude and the same phase speed. We are particularly interested in the case where A or ζ are fixed. There are four elevation waves of amplitude $A = 0.48$ corresponding to points (1)-(4) in Figure 6.5. The surface profiles are shown in Figure 6.6. The first one is the classical elevation wave with decaying tails. As it moves along the curve, the far field becomes flat and there are only two ripples survived near the origin, which can be seen in the second profile of Figure 6.6. As it continues further, one large crest is generated between the previous two, which is shown in the third profile. Then decaying tails are generated beyond the large ripples.

Similarly, there exists different waves with the same phase speed as shown in Figure 6.7. The surface profile eventually becomes a depression-like wave. The profile corresponding to the final point of the curve can be seen from Figure 6.8. Its phase speed is very close to the minimum phase speed. By symmetry, this elevation wave is essentially consisting of two depression waves with a dimple in the middle. The instability of this wave might be related to the instability of depression waves, which will be figured out in Chapter 7.
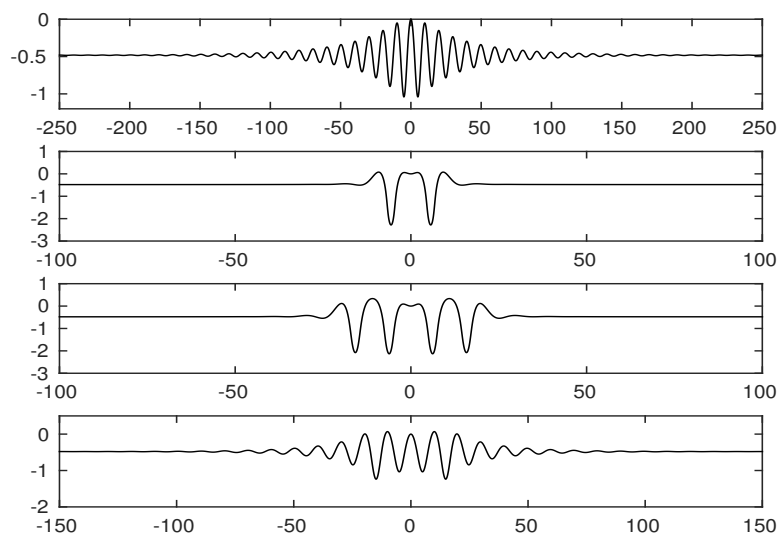
Figure 6.6: Surface profiles for elevation waves of amplitude $A = 0.48$. They correspond to point (1), (2), (3), (4) in Figure 6.5 from top to bottom.
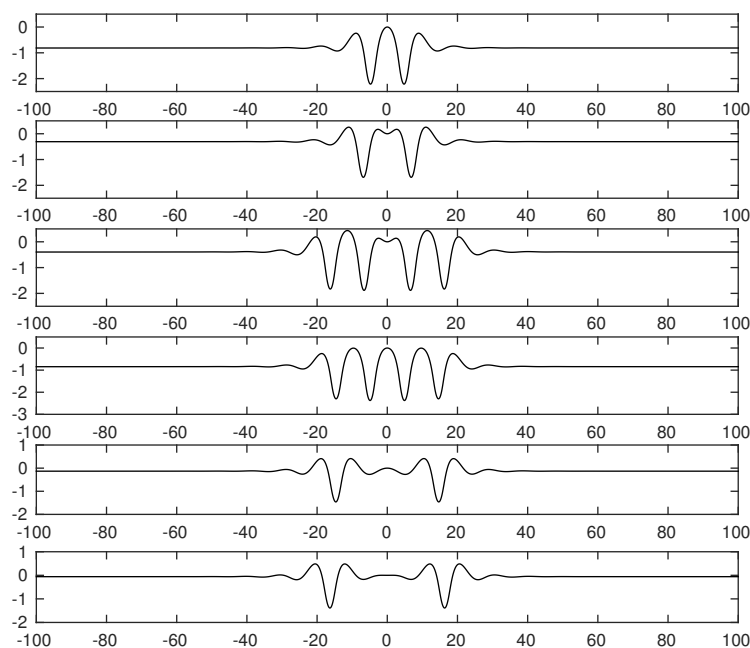
Figure 6.7: Surface profiles for elevation waves of phase speed $c = 1.25$. They correspond to points (i), (ii), (iii), (iv), (v) and (vi) in Figure 6.5 from top to bottom.

The energy-velocity graph for elevation waves is very complicated as shown in Figure 6.9. The energies at the points (i)-(vi) are shown in Table 6.1. The energies at point (i), (ii), (v) and (vi) are very close to each other whilst the energies at point
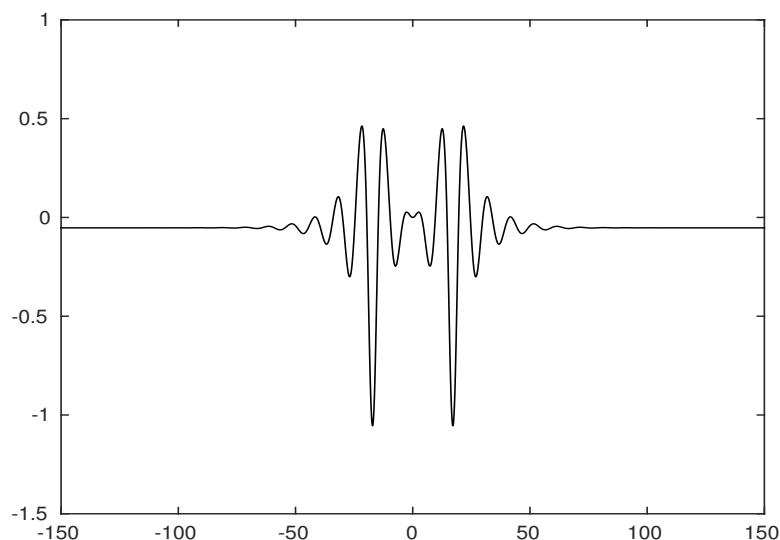
Figure 6.8: Surface profile corresponding to the final point on the amplitude bifurcation curve for elevation waves.

At point	(i)	(ii)	(iii)	(iv)	(v)	(vi)
The values of energy	11.27	10.44	23.95	25.37	10.21	10.13

Table 6.1: Energy values at point (i)-(vi).

(iii) and point (iv) are approximately doubled. This is very reasonable since there is one extra large ripple in the half of the wave in these two profiles (iii) and (iv). The instability changes many times in this case. We expect that the waves are initially stable when c is close to the minimum phase speed. It will be interesting to work this out numerically in Chapter 7.

6.1.3 Conclusion

In this section, we have studied the flexural-gravity solitary waves in deep water using the numerical method introduced in Section 3.1. We have found that both elevation and depression waves bifurcate from non-zero amplitude, which is different from the gravity-capillary problem. We have also presented the energy bifurcation diagrams for both elevation and depression waves.

In Section 3.2, we introduced a new numerical scheme which allows us to study the time-dependent solutions. We will use it to study the stability of the waves

by perturbing the steady solutions. This method may be also applied to find non-symmetric waves.
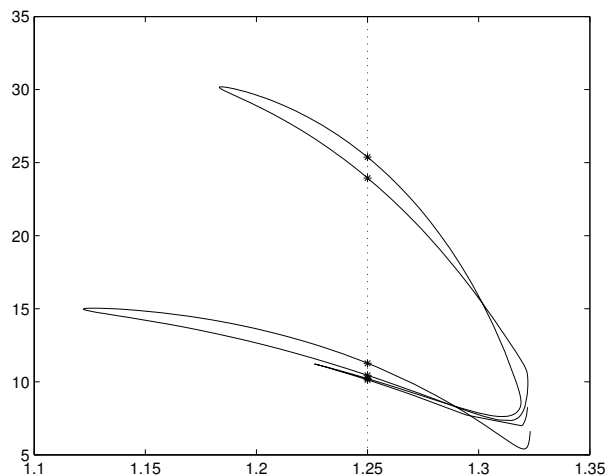
Figure 6.9: Energy versus ζ for elevation solitary waves.

6.2 Symmetric Waves: analytical insight

As shown in the last section, the dispersion relation (3.62) implies that the linear phase speed has a global minimum at finite wavenumber. Free solitary waves, which are fully localised in the horizontal direction and propagate with the translating speed c without changing form, may exist below this minimum (namely, $c < c_{\min} \approx 1.3247$). Nevertheless, the weakly nonlinear analysis shows that at the bifurcation point (i.e. the minimum of the phase speed) the associated cubic nonlinear Schrödinger equation (NLS) is of defocussing type. The NLS is a conventional tool to predict the existence of wavepacket solitary waves and their dynamical behaviours in the modulational regime. Briefly we introduce the amplitude parameter ϵ and the slow-varying variables $(X, T, \tau) = (\epsilon x, \epsilon t, \epsilon^2 t)$, then expand the free surface and the velocity potential as

$$\eta = \epsilon A(X - c_g T, \tau) e^{i(kx - \omega t)} + \epsilon^2 A_1 + \epsilon^3 A_2 + \cdots + \text{c.c.} , \tag{6.5}$$

$$\phi \;=\; \epsilon B(X - c_g T, \tau)e^{i(kx - \omega t) + |k|y} + \epsilon^2 B_1 + \epsilon^3 B_2 + \cdots + \text{c.c.}, \qquad (6.6)$$

where 'c.c.' represents the complex conjugate and $c_g = \omega_k$ is the group velocity. Substituting the ansatz (6.5) and (6.6) into the system (2.3) (3.48) and (3.51) with the external forcing $P_e = 0$ results in the NLS for the envelope A:

$$iA_\tau + \lambda(k)A_{XX} = \gamma(k)|A|^2 A. \qquad (6.7)$$

If we consider the special wavenumber k^* which is at the phase speed minimum, namely $k^* = 3^{-1/4}$, the coefficients of (6.7) read

$$\lambda = \frac{14}{11}\,3^{-9/8}, \qquad \gamma = \frac{1}{44}\,3^{-9/8}. \qquad (6.8)$$

The reader can find the derivation of (6.7) and (6.8) in [31], and we omit the details in the present work. We can deduce from the positivity of λ and γ that the cubic NLS (6.7) at k^* is of defocussing type, hence there are no small-amplitude solitary waves bifurcating from the phase speed minimum. However the normal form analysis described above does not exclude large-amplitude solitary waves in the full Euler equations. [18] first computed free solitary waves bifurcating from the phase speed minimum $c^* \approx 1.3247$, including both elevation branch (a positive free-surface elevation at their centre) and the depression branch (a negative free-surface elevation at their centre), with (3.65). They noticed that hydroelastic solitary waves in Plotnikov-Toland model can only exist with non-zero amplitude as shown in Figure 6.10(a), which is coincident with the Kirchhoff-Love model (see [30]). Later on, [54] calculated the complete solution branches for depression and elevation solitary waves. They found that the elevation branch exhibits multiple turning points, which indicates that different elevation solitary waves can travel at same speed (typical profiles of the elevation solitary waves are shown in the top figures of Figure 7.4). For
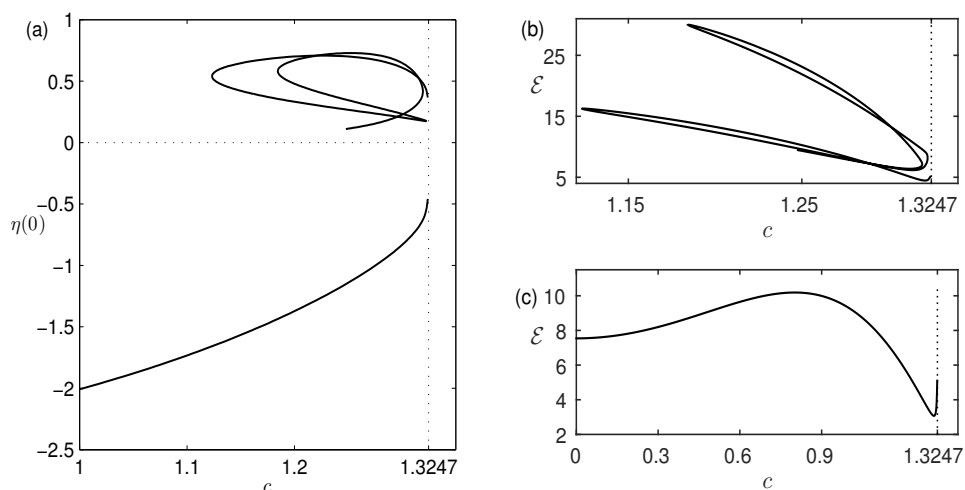
Figure 6.10: Speed-amplitude and speed-energy curves for symmetric elevation and depression solitary waves emerging from the bifurcation point $c^* \approx 1.3247$. (a) speed-amplitude curves of the elevation and depression branches. The value of the middle point of the wave profile is considered as the amplitude. The depression branch is monotonic for $c \in [0, c^*)$ (only part of the curve is shown), while the elevation branch demonstrates complex behaviour with multiple turning points. (b) speed-energy curve of the elevation branch showing a zig-zag behaviour; (c) speed-energy curve of the depression branch with two stationary points.

the depression branch, both [18] and [54] found that as the speed c decreases and approaches zero, the depression solitary waves become steeper, eventually with an overhanging profile (a typical example of overhanging solitary wave is shown in the right panel of Figure 7.1). The speed-energy bifurcation curves are shown in Figure 6.10 (b,c) which are closely related to the stability property of solitary waves subject to longitudinal perturbations. [38] considered the stability of periodic waves due to superharmonic perturbations (the period of the perturbation is less than that of the wave), and gave a necessary but not sufficient condition for the stability exchange. He pointed out that the stability exchange must occur at the critical points, either stationary points or turning points, of the speed-energy bifurcation curve, namely,

$$\frac{\partial \mathcal{E}}{\partial c} = 0 \ \ \text{or} \ \ \frac{\partial c}{\partial \mathcal{E}} = 0. \tag{6.9}$$

Saffman's argument is based on Hamiltonian formulation of water waves (see [57]) and for pure gravity waves. However, the result can be generalised to hydroelastic waves without any essential modification due to its Hamiltonian structure (3.52). Furthermore, since all the disturbances are superharmonic for solitary waves, Saffman's conclusion is extremely useful for our problem. In Section 7.1, we will focus on the stability properties for solitary waves via direct numerical simulations together with Saffman's result.

6.3   Non-symmetric Waves: numerical results

The numerical evidence of non-symmetric gravity-capillary waves in deep water has recently been shown in [53]. The basic idea for computing these waves is that the non-symmetric gravity-capillary solitary waves feature multi-packet structures, namely they are formed by two or more adjacent packets. This fact leads to the idea of constructing non-symmetric hydroelastic solitary waves, since Plotnikov-Toland model supports both elevation and depression branches so that different solitary waves can propagate with the same speed. In order to compute non-symmetric hydroelastic solitary waves, it is essential to choose a good initial guess for the Newton iterations. Following the procedure described in [53], we choose a depression wave (the top figure in Figure 6.11) and an elevation wave (the middle figure in Figure 6.11) computed in the last section. These two waves have the same translating speed which is close to $c_{\min}$. We shift the profiles and then merge them in the middle as a new wave profile (see the bottom figure in Figure 6.11). This new profiles is considered as the initial guess of the Newton's method, and the algorithm converges to a solution after several iterations. After obtaining a convergent solution, we can follow the branch by using the continuation method to complete the complete speed-
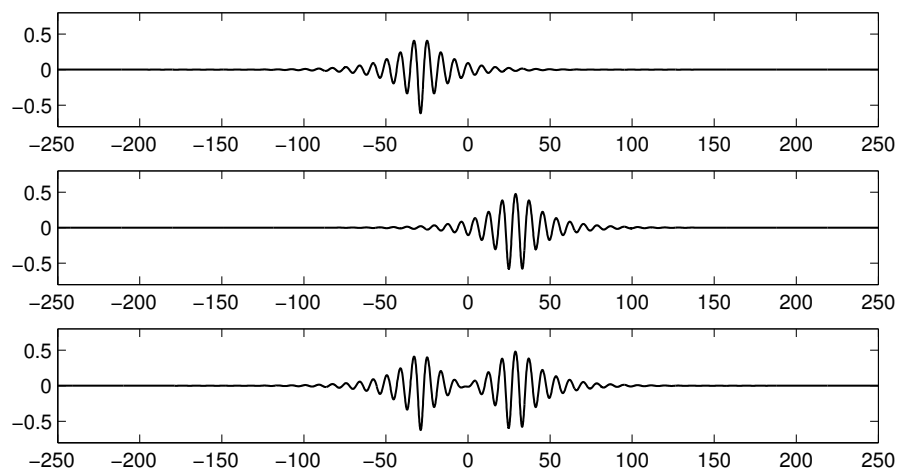
Figure 6.11: An initial guess of non-symmetric hydroelastic solitary-wave profile (bottom figure) which is composed of a depression wave (top figure) and a one-hump elevation wave (middle figure) propagating at $c = 1.32$.

energy bifurcation diagram which has been shown in Figure 6.12 .

Figure 6.12 shows that the speed of non-symmetric solitary waves from this branch is always below the minimum of the phase speed. Therefore these waves are not resonant with linear periodic waves, namely, they do not turn to be generalised solitary waves or periodic waves (see [30] for comparison). In Figure 6.12 , the solid curves in the middle correspond to the non-symmetric waves, whereas the dotted curve and the dashed curve to the symmetric waves. And typical wave profiles labelled (a)–(f) are shown in Figure 6.13 including two non-symmetric ones (see Figure 6.13 (c,d)). As can be seen from Figure 6.12 , the solid branches join the dashed and the dotted branches, i.e. the non-symmetric waves eventually become symmetric (see profile (g) and (h) in Figure 6.13) . It shows that the non-symmetric waves appear from a spontaneous symmetry-breaking bifurcation and vanish at another symmetry-breaking bifurcation. It is worth mentioning that profiles 6.13 (a,b) from the upper branches are essentially consisting of two identical elevation waves, while the profiles 6.13 (e,f) from the lower branches are two depression waves merged at the origin. Energywise, the results are quite reasonable since an elevation wave possesses more energy than a depression wave with the same speed.
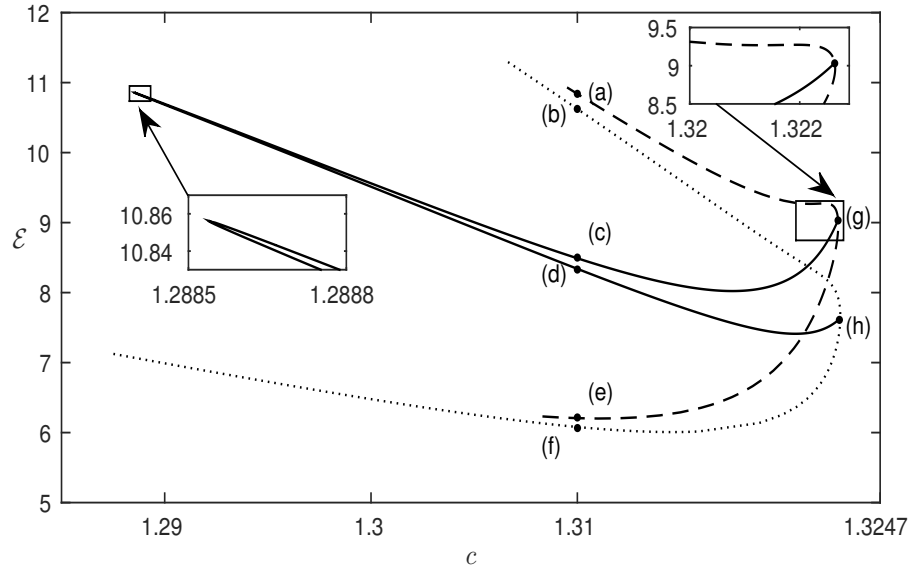
Figure 6.12: Speed-energy bifurcation diagram of non-symmetric hydroelastic solitary waves. The solid curve correspond to the branch of non-symmetric waves. The dotted curve and the dashed curve correspond to two different branches of symmetric waves where the non-symmetric branch bifurcates from. (a)-(f) correspond to those waves travel at speed $c = 1.31$ whose profiles are shown in Figure 6.13.
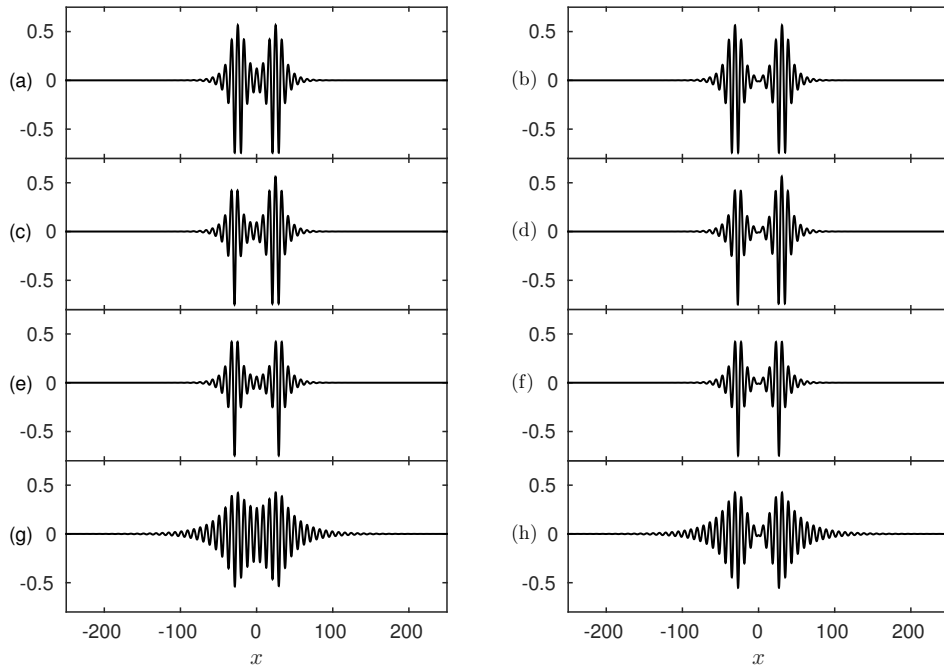
Figure 6.13: Typical wave profiles plotted in the physical plane which corresponding to points (a)-(h) indicated in Figure 6.12. (c) and (d) are the typical profiles of the non-symmetric waves; (g) and (h) correspond to two symmetry-breaking bifurcation points.

There exist many other families of non-symmetric solitary-wave solutions which can be found by using different initial guesses because of the many possible choices of elevation waves travelling at the same speed as demonstrated in Figure 6.10. These results have been published in [15].

Chapter 7

Dynamics and stability of solitary waves

7.1 Stability

In this section, we study the stability problem of the hydroelastic solitary waves subject to longitudinal perturbations. We recall that (3.58) and (3.59) are the time-evolution equations. The travelling-wave solutions superposed by small perturbations are used as initial data for the dynamics. Meanwhile we choose a frame of reference moving with the speed of the unperturbed solitary wave.

We start with the symmetric depression solitary waves. We recall the speed-energy bifurcation curve for the depression branch in Figure 7.1, which has two stationary points labelled (1) and (2) in the figure. According to Saffman's theory [38], the stability exchange may occur at these points. We first consider the stability of the waves before the first stationary point ($c \lesssim 0.8$). The waves in this regime are large and steep, and some have even overhanging structures. Therefore the numerics becomes very *stiff*, namely, if an explicit time integration method is used, there is a strong stability constraint on the time step. The constraint can be removed by using an implicit integration scheme, such as the backward Euler's method which is
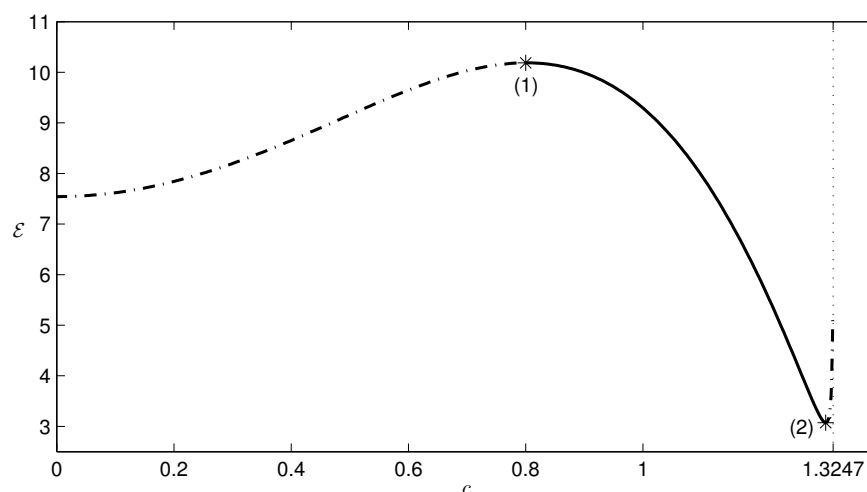
Figure 7.1: Stability of the depression waves. Waves from the solid branch are stable whereas those from the dash-dotted branches are unstable. The stationary points have been marked as stars in the graph.

applied in the present paper. We take a large-amplitude depression solitary waves $\eta(\xi)$ with $c = 0.5$ and $\eta(0) = -2.70$, which features the overhanging structure (see the top figure of the right panel of Figure 7.2). At $t = 0$, a small perturbation, which equals $0.01 \cos(\xi)\eta(\xi)$ in the example we have shown in Figure 7.2, is added to the steady solution. The system (3.58) and (3.59) is then integrated by the backward Euler's method with the time step $dt = 0.002$, and in each step the discretised nonlinear algebraic system is solved via the Newton's method. The time evolution of the perturbation in the transformed space is shown in the left part of Figure 7.2. While wave profiles in the physical space at time $t = 0, 2, 4$ are presented in the right panel from top to bottom, from which we can conclude that the bubble changes its shape quickly and is then of-course unstable. We stop the computation when the wave touches itself forming a closed bubble. Beyond this particular time, the solution becomes unphysical subject to the Euler system since the topology of the fluid domain changes. We can further deduce from this numerical experiment that the depression solitary waves lie in the segment $0 < c \lesssim 0.8$ are all unstable due to Saffman's theory.

For the remaining time-evolution computations, we use the fourth-order Runge-
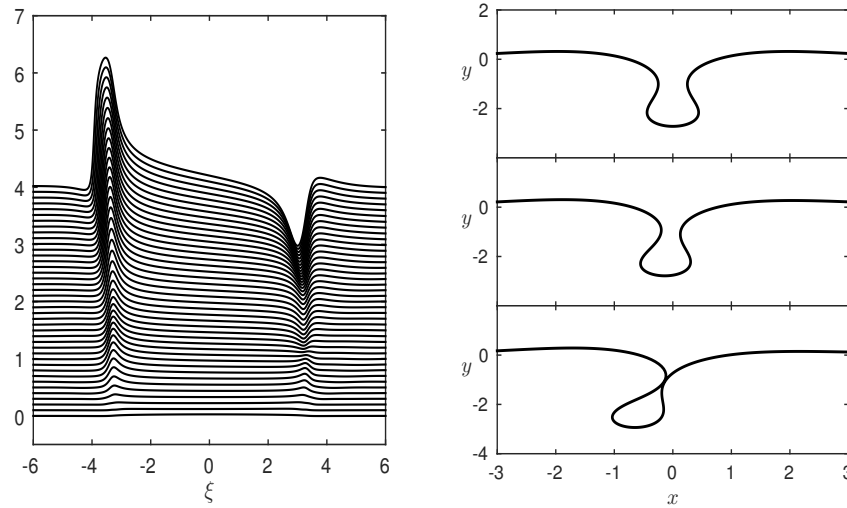
Figure 7.2: Time evolution of a large-amplitude depression solitary wave propagating with the velocity $c = 0.5$ and amplitude $\eta(0) = -2.70$. The computation is performed with $dt = 0.002$ and $d\xi = 0.01$. Left: time evolution of the perturbation which is initially $0.01\cos(\xi)\eta(\xi)$ for $t = 0, 0.01, 0.02, ..., 4$ (left bottom to top). Right: wave profiles in the physical space at time $t = 0, 2, 4$ (right top to bottom). Only the main profiles are shown in figures.

Kutta method rather than the backward Euler's scheme since the problems are not extremely stiff for moderate-amplitude hydroelastic solitary waves. The mesh size in space and the step size in time are chosen to be $d\xi = 0.1$ and $dt = 5 \times 10^{-4}$ respectively in most numerical experiments. For the solid part in Figure 7.1 (the segment between the stationary points (1) and (2)), a variety of perturbations with 5% of the energy of the initial depression solitary waves did not show instability. However, as the speed increases and passes the second stationary point, the solitary wave regains the instability where the curve becomes dot-dashed again in Figure 7.1. The snapshots of the dynamics of a depression solitary wave in this region subject to the 1% amplitude-decreasing perturbation are shown in Figure 7.4 (a). The wave eventually disperses out as time evolves. Finally we can draw the conclusion that for the depression branch of hydroelastic solitary waves, there are two stationary points in the speed-energy bifurcation diagram and the stability exchanges occur at both of them (see Figure 7.1).

The stability problem for the elevation branch is more complicated since the
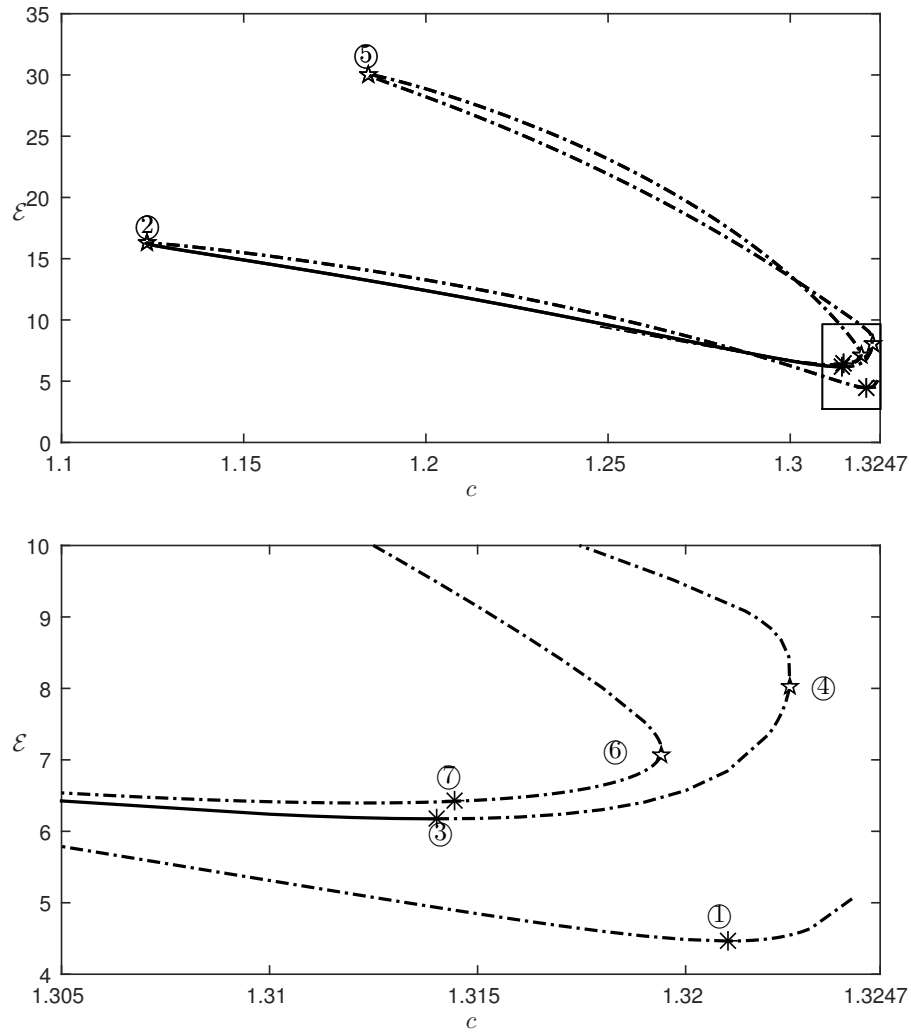
Figure 7.3: Stability of the elevation waves. The graph on the bottom is a zoom in of the box in the graph on the top. Waves from the solid branches are stable whereas from the dot-dashed curves are unstable. The stationary points and the turning points are marked as stars and pentagrams respectively in the graphs.

speed-energy curve has many stationary points and turning points, and we need to choose one typical example between every two successive critical points and check its stability. In the speed-energy bifurcation diagram (Figure 7.3), the stationary points and the turning points have been numbered from ① to ⑦. We found that only the waves between the turning point ② and stationary point ③ (solid curve in Figure 7.3) are stable subject to the longitudinal perturbations. All other waves on the elevation branch (dot-dashed curve in Figure 7.3) turn out to be unstable.

We present some time-evolutions of elevation waves to demonstrate their stability

properties. A wave from the segment on the right of point ① has been perturbed by 1% of the amplitude of its initial steady wave. The snapshots show little focussing phenomenon and symmetry-breaking instability as well, and finally becomes a stable depression solitary waves with a radiated wave field of linear wave packets shed on both sides (see Figure 7.4 (b)). Figure 7.5 (a) displays a stable elevation wave which is located between point ② and ③ of Figure 7.3. These stable elevation solitary waves feature two big troughs separated by a small dimple. A 5% amplitude-decreasing perturbation has been applied to the initial solitary wave but did not show any instability for a long-time computation. It is worth mentioning that the amplitude-decreasing perturbation results in a wave of slightly smaller energy but larger speed than the original one which shows the right translation in the moving frame. However, not all the elevation waves featuring two depression solitary waves placing side-by-side are stable. Figure 7.5 (b) presents an example of unstable elevation waves composed by two troughs with a small hump. The wave is located from the very last branch, i.e. beyond ⑦, with $c = 1.25$, $\eta(0) = 0.113$ and $\mathcal{E} = 9.34$. We choose a specific perturbation which decreases the amplitude of the left trough by 0.5% and increases the right one by 0.5%. Therefore the speed of the left trough is greater than that of the right trough so that overtaking collision occurs from which we can deduce its instability.

We then move on to the stability of the non-symmetric solitary waves computed in Section 6.3. One typical example with $c = 1.3$ are shown in Figure 7.6. We take a solitary wave, which consists of a stable depression wave on the left and an unstable elevation wave on the right connected with small ripples in the middle, as the initial data. As time goes on, the depression wave remains unchanged but the elevation wave abruptly turns to be a depression wave with a larger amplitude (see the second graph of Figure 7.6). Although we can already conclude that the non-symmetric solitary wave is longitudinally unstable, it is still interesting to continue

Figure 7.4: Time-evolution of (a) a depression wave profile with $c = 1.32$ plotted in the physical plane at $t = 0, 500, 1000$ (right top to bottom), (b) an elevation wave profile with $c = 1.323$ plotted in the physical plane at $t = 0, 1500, 3000$ (left top to bottom).

the computation to see what happens next. We notice that the depression wave of a larger amplitude travels at a lower speed. It follows that the wave on the right travels leftwards since its speed is less than the speed of the moving frame. Therefore the stability problem becomes an overtaking collision. From the graph on the bottom, we observe that the depression wave of larger amplitude survives while the smaller one is killed. Numerical experiments have been done for other non-symmetric solitary waves on different sides of the turning point in Figure 6.12 and it turns out that all the non-symmetric waves are unstable on this branch.

7.2   Dynamics

7.2.1   Collision

In this section, head-on collision and overtaking collision between stable hydroelastic solitary waves are both considered. For all collision experiments, the initial data were constructed by shifting the existing travelling waves so as to minimize
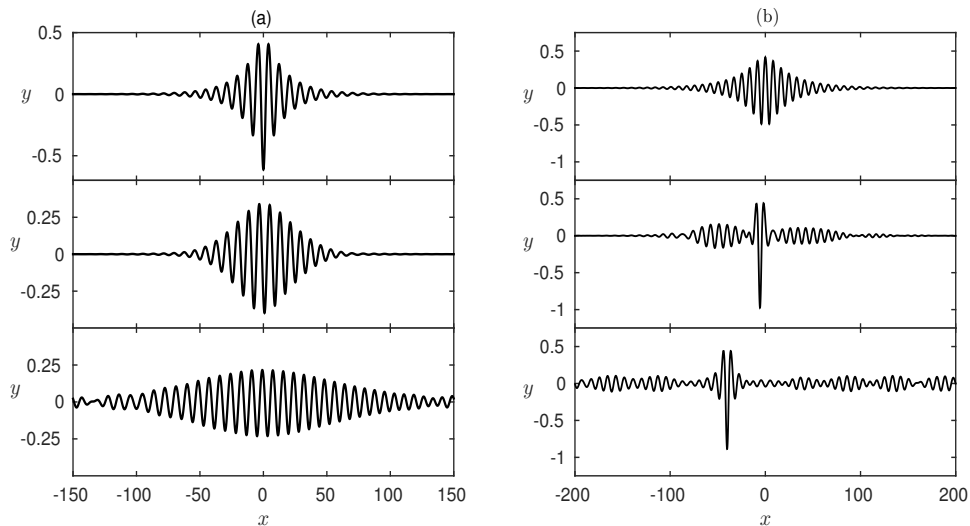
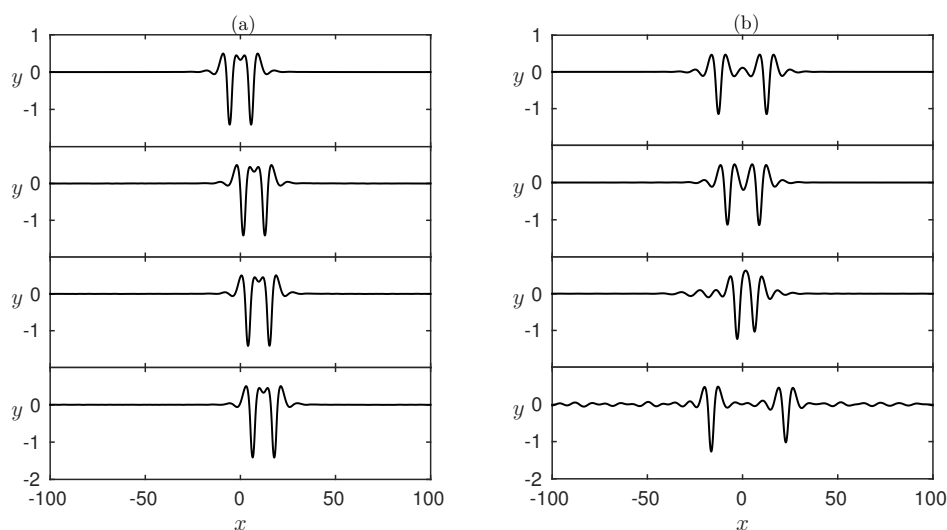Figure 7.5: Time-evolution of (a) an elevation wave profile with $c = 1.2$ plotted in the physical plane at $t = 0, 3000, 4000, 5000$ (left top to bottom), (b) an elevation wave profile with $c = 1.25$ plotted in the physical plane at $t = 0, 750, 1000, 1500$ (right top to bottom).
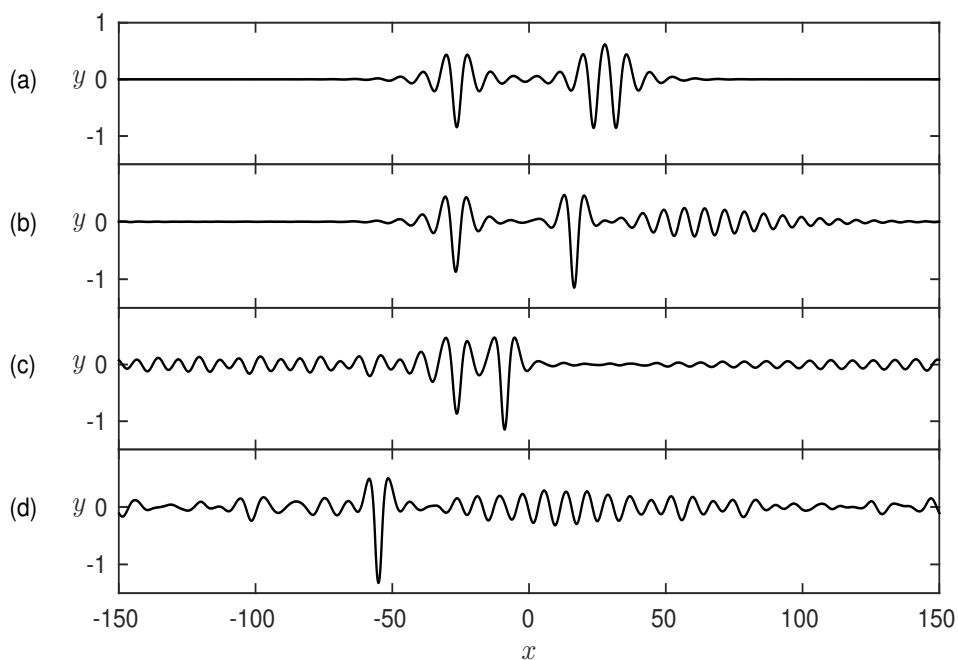
Figure 7.6: Time-evolution of an non-symmetric wave profile with $c = 1.3$ plotted in the physical plane for time $t = 0, 250, 750, 1250$ (from a-d).
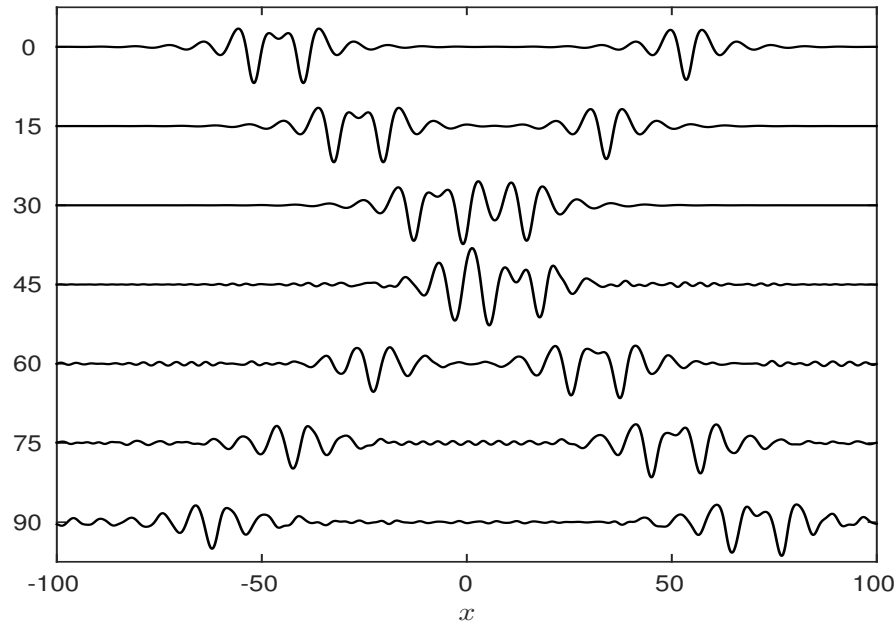
Figure 7.7: Head-on collision. An elevation wave travels rightwards at a speed $c = 1.3$ and a depression wave travels leftwards at a speed $c = 1.3$. The wave profiles are shown for time $t = 0, 15, 30, 45, 60, 75, 90$.

their overlap, and then adding them together.

A typical example of head-on collisions is shown in Figure 7.7, where a stable elevation waves traveling rightwards collides with a stable depression one travelling leftwards. The collision is inelastic even though both waves survive after the collision, since a lot of visible ripples shed on both sides during the collision (see Figure 7.7). Several other computations of head-on collisions were carried out, and in all cases the collisions appeared to be inelastic.

The second set of numerical experiments on the dynamics of hydroelastic solitary waves is of overtaking collisions. We choose two stable depression waves travelling along the same direction but with different translating speed. When the difference in wave amplitudes between the two waves is large, only one wave remains after the collision with a radiation field. However, both depression wave can survive if both of them are of moderate amplitude and their amplitude difference is small. As can be seen from Figure 7.2.1, the overtaking collision is also inelastic in the case when both waves survive whereas some radiation field is generated during the interaction. The

accuracy of the integration was tested by monitoring the value of the total energy, the error of which was of order 10^{-12} through the whole computation. The difference between the initial data and the solution obtained by reversing time after $t = 4200$ in the collision was of order 10^{-9} (see figure 7.2.1. This further validates the time-dependent codes. We can also choose a stable elevation wave to overtake a depression one, and vice versa. One example of this kind of overtaking collision is presented in Figure 7.9 . The structure of the elevation solitary wave featuring two well-separated troughs was destroyed during the interaction, and two depression waves travelling at different speeds were observed finally.

7.2.2 Excitation

The coupling between a moving load and the hydroelastic waves generated by it in a floating ice sheet has attracted a long interest since it enjoys wide usage in the safe use of transport links in polar region ([42, 44, 55]). Due to the linear theory, the critical velocity for resonance between the moving load and the hydroelastic waves occurs at the minimum of the phase speed. The resonance results in the accumulation of the energy and unlimited growing in amplitude of the wave, therefore the linear theory fails to predict the wave behaviour in reality. The nonlinear effects in the problem of of an elastic sheet under moving loads has been considered by [2, 30, 34] based on the Kirchhoff-Love model and [18, 19] based on the Toland's elastic model with the truncation of Dirichlet to Neumann operator in the time-dependent computations. When a fully localised forcing moving with a constant speed slightly below the phase speed minimum, the fundamental phenomena of the nonlinear waves generated by the load is the periodic shedding of solitary waves. These finite-amplitude stable responses used to radiate the energy are observed in all aforementioned experiments but cannot be explained via linear theory.

Based on the full Euler computations, we now consider the generation of stable
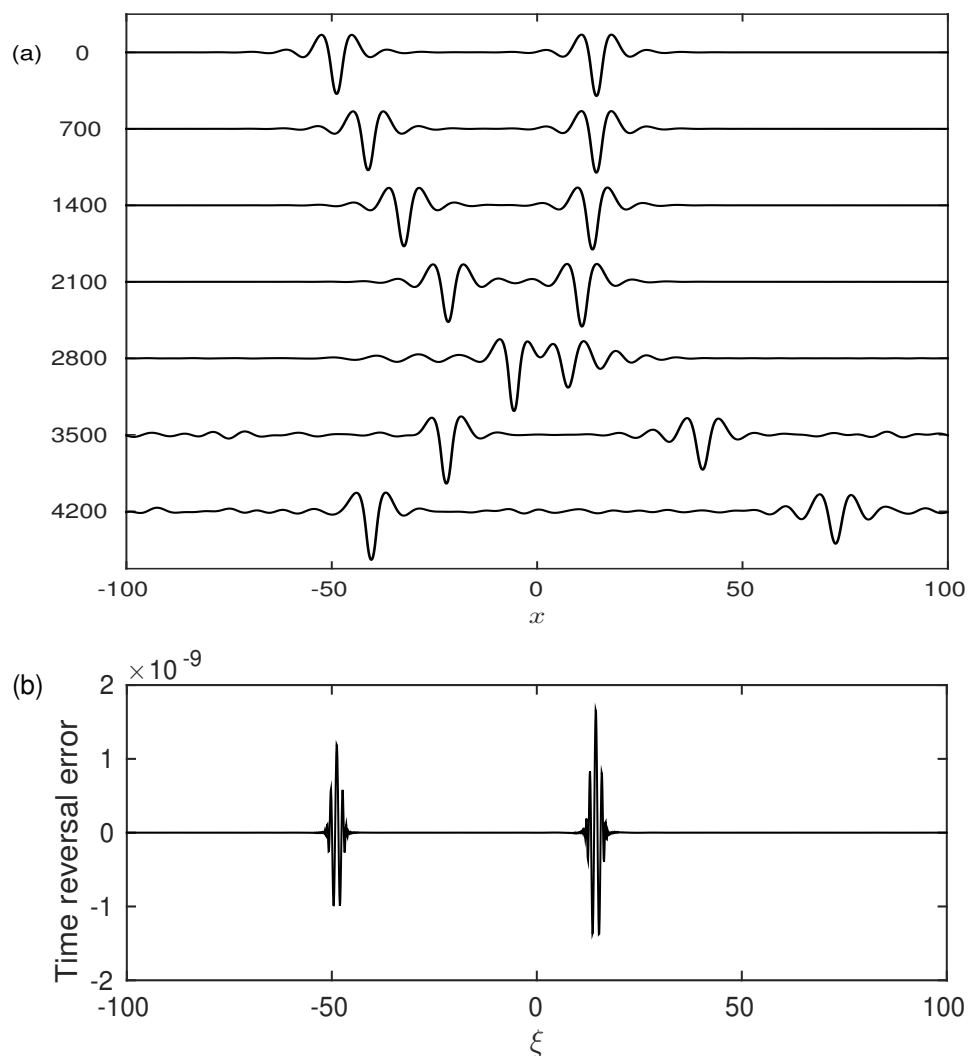
Figure 7.8: Overtaking collision. Two depression waves travel rightforwards at $c = 1.26$ and $c = 1.25$ respectively. (a) Snapshots for time $t = 0, 700, 1400, 2100, 2800, 3500, 4200$ are shown in a frame of reference moving with the speed c = 1.25. (b) The difference between the initial data and the time-reversed solution computed from $t = 4200$ back to $t = 0$.
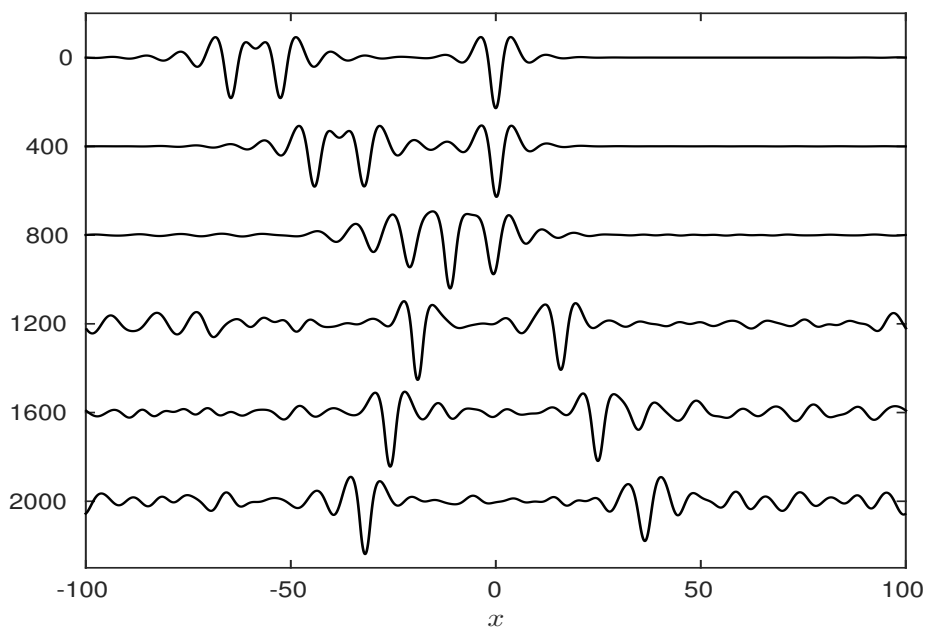
Figure 7.9: Overtaking collision. An elevation wave travels rightforwards at $c = 1.3$ and a depression travels at $c = 1.25$ in the same direction. The wave profiles are shown for time $t = 0, 400, 800, 1200, 1600, 2000$.

hydroelastic solitary waves by loads moving steadily on an ice sheet floating on the top of deep water. When the speed of the moving forcing, c, is slightly less than the phase speed minimum, the forced problem does not admit a travelling-wave solution and is therefore called the *transcritical regime* in the literature. [30] and [18] have managed to obtain the stable depression solitary waves by using a moderate-amplitude moving pressure. We first reconsider their situation using the full Euler equations with Toland's elasticity. A single moving pressure which is defined as

$$P = A\, e^{-(x+220-ct)^2/16}\,, \tag{7.1}$$

is applied in (3.59) initially with the amplitude $A = 0.2$ and the translating speed $c = 1.3$. It was then switched off at $t = 125$. This problem has been considered in [29] for the Kirchhoff-Love model and [18] based on a truncated model for the Toland's elasticity. We found the similar results that the system gains enough localised energy before the forcing is switched off and the solution rapidly relaxes to a symmetric

Figure 7.10: Snapshots of the free-surface due to large-forcing moving pressures ($A = 0.2$ and $u = 1.3$) at $t = 25, 100, 140, 200, 325$ (from top to bottom). The forces is switched on at $t = 0$ and off at $t = 125$. It is initially placed at $x = -220$.

depression solitary wave after the forcing is released (see Figure 7.10). This large-amplitude, fully-localised response can coexist within the background radiation filed and propagate for long time, which proves its stability from another point of view.

The stability analysis in Section 7.1 shows that besides the moderate-amplitude depression waves, the elevation waves with the structure of two well-separated troughs connected by a dimple is also longitudinally stable. One can therefore ask the question whether these stable elevation solitary waves can be obtained in the full Euler equations by moving loads. Motivated by the structure of the stable elevation solitary waves, one applies two fully-localised pressures separated properly and moving simultaneously on the ice sheet. The pressures are defined as

$$P_1 \;=\; A\,e^{-(x+220-ct)^2/16} , \tag{7.2}$$

$$P_2 \;=\; A\,e^{-(x+220+d-ct)^2/16} , \tag{7.3}$$

where A is the parameter of measuring the amplitude of the pressures and d is the
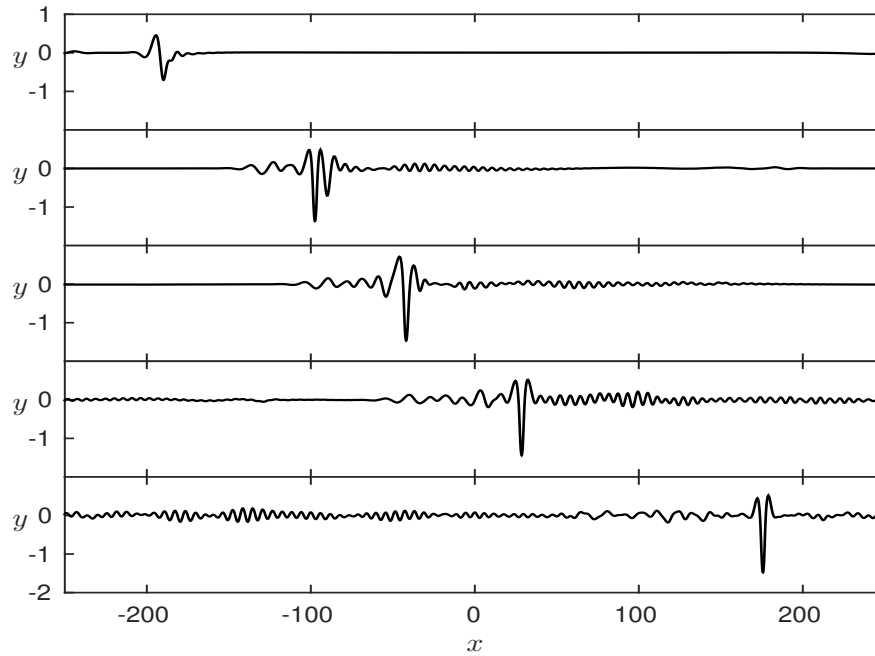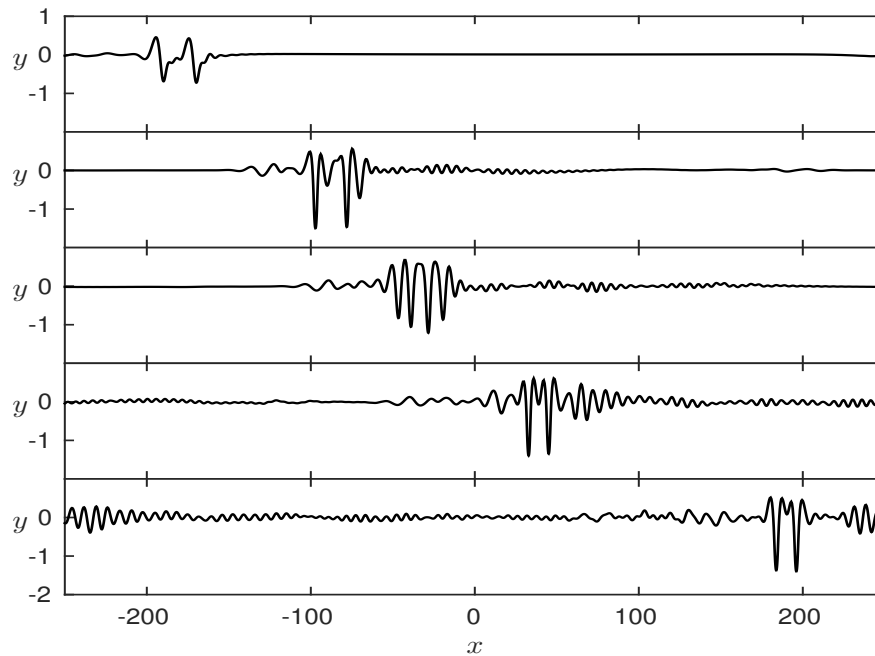
Figure 7.11: Snapshots of the free-surface due to large-forcing moving pressures ($A = 0.2$ and $c = 1.3$) at $t = 25, 100, 140, 200, 325$ (from top to bottom). The forces are switched on at $t = 0$ and off at $t = 125$. The centre of P_1 is initially placed at $x = -220$ and that of P_2 is at $x = -200$,i.e., $d = 20$.

distance between the centres of two pressures. Figure 7.10 shows the snapshots of the generation of a stable elevation solitary wave by two pressures moving with the same speed. An elevation wave of two big troughs quickly forms after the forcing is turned off (the 3rd and 4th pictures in Figure 7.11). From longer computations (not shown), we believe that these solitary waves are stable and robust. This large response can propagate without changing its main structure, in spite of the interactions with the background radiation induced by the initial generation process. This numerical experiment can be used to mimic cars or aircrafts running successively on a very large floating structure and implies that fully-localised two-trough structure may be observed in the real situation.

7.3 Conclusion

As shown in Chapter 6 , the Toland's elastic model allows depression and elevation solitary waves both of which are symmetric in the wave propagation direction. These two branches, which were previously computed and extended respectively by [18] and [54], were quickly reviewed. Both the depression and the elevation branches bifurcate from the minimum of the phase speed and exist in the subcritical regime (namely, the translating speed of the solitary wave is less than the phase speed minimum) with non-zero amplitudes. The fact that different symmetric solitary can propagate with the same speed inspires us to search for non-symmetric solitary waves in hydroelastic waves. We superposed a depression wave and an elevation one as the initial guess to successfully find an non-symmetric solitary wave using Newton's method. Based on this solution, the complete bifurcation diagram were then carried out by using the numerical continuation method. These asymmetric solitary waves feature two-packet structure and only exist in the subcritical regime. The non-symmetric branch appears from a spontaneous symmetry-breaking bifurcation and end up with another symmetry-breaking bifurcation.

The stability properties of all the hydroelastic solitary waves found to date subject to longitudinal perturbations were systematically studied by using the time-dependent conformal map technique together with backward Euler's method or fourth-order Runge-Kutta method in time integration. Our numerical experiments show that moderate-amplitude depression waves (lie between stationary points (1) and (2) in Figure 7.1) and certain elevation waves featuring two troughs connected by a dimple (lie in the segment between the turning point ② and the stationary point ③ in Figure 7.3) turn out to be stable. These two kinds of stable solitary waves can both be excited by applying one or two loads on the ice and moving the loads with a constant speed slightly below the minimum phase speed. Once the system gains enough localised energy, a stable hydroelastic solitary wave with the radiation field

can be obtained after the pressure is switched off. Also, a series of numerical experiments were performed to show the non-elastic behaviour of two interacting stable solitary waves. These results have been published in [15].

Chapter 8

Non-symmetric periodic gravity-capillary waves

It is well acknowledged that a bifurcation can lead to symmetry breaking. Two typical examples are Hopf bifurcation and Bénard convection in physics. The temporal symmetry is destroyed in a Hopf bifurcation, and so is the spatial symmetry in Bénard convection. Symmetry breaking plays a major role in pattern formation whose aim is to discover the principles behind it. It can be found in many scientific disciplines such as biology, chemistry, and physics. On the theoretical side, there is an extensive literature on the analysis of bifurcation and symmetry breaking by using the group-representation theory, e.g. [39].

The problem of solving the Euler equations for travelling waves on the surface of water flows has been widely studied by many authors both analytically and numerically, however in most works certain symmetry conditions were imposed. The term "symmetric waves" is defined to be those waves whose shape is symmetric about the vertical axis. If a wave is symmetric about a vertical line other than the vertical axis, we call this wave a shifted symmetric wave. Apart from these two kinds of waves, the others are named non-symmetric waves. Non-symmetric water waves receive considerable attention not only because symmetry breaking is of scientific

interest as mentioned in the last paragraph but also because it is a big mathematical challenge to find new kinds of fully nonlinear solutions in surface water-wave problems. Without further specifications, all the waves are assumed to be periodic in this Chapter.

For pure capillary waves, [6] derived exact nonlinear symmetric solutions of explicit form in terms of elementary functions on water of infinite depth. The wave profile becomes steep as the amplitude increases prior to reaching a limiting configuration with a trapped bubble at the trough. Beyond that, the profile had a non-physical self-intersecting structure. [50] extended the family of Crapper's solutions beyond the limiting configuration by considering the pressure inside the trapped bubble as part of the solutions. [47] worked on capillary waves with variable surface tension and found new solutions by using a collocation method. [32] proved the non-existence of bifurcation from the family in [6] (known as Crapper's waves). This implies that non-symmetric capillary waves are very unlikely since there are no solutions found other than Crapper's. [24] generalised Crapper's solutions to the case of capillary waves on fluid sheets of finite thickness and to capillary waves on water of finite depth. [7] presented a simple derivation by using complex variables. [1] found new solutions which have no horizontal symmetry or anti-symmetry from Kinnersley's solutions. However these waves were still symmetric in a sense of "symmetric waves" defined earlier. Whether or not non-symmetric capillary waves on fluid sheets exist remains an open question.

For pure gravity waves, the problem was studied widely in the case of finite and infinite depth since the pioneering work of [43]. Most of the work was done for symmetric waves. The research on non-symmetric waves could be tracked back to 1980 when [4] found bifurcations to new families of solutions in the case of deep water. They tried to compute non-symmetric gravity waves but only shifted symmetric waves were found. [59] derived a weakly nonlinear Hamiltonian model to find non-

symmetric waves with 6 peaks via spontaneous symmetry breaking bifurcations from symmetric waves. Later [58] used numerical approaches to compute non-symmetric waves on water of infinite depth for the full Euler equations. Qualitatively similar results with 6 peaks in one wavelength were produced but no other solutions were presented. It remains unclear whether there exist non-symmetric gravity waves with peak number other than 6.

In the presence of both gravity and surface tension, there is a very rich structure of solutions for water waves. [56] showed the non-uniqueness of solutions, even for waves at small amplitude, which are the so-called Wilton's ripples. The reader is referred to [49] for a quick review. [59] used again a weakly nonlinear Hamiltonian model to rediscover non-symmetric gravity-capillary waves with 6 peaks in the case of finite depth. He also computed approximate non-symmetric solitary waves. New non-symmetric waves with 2 peaks were discovered numerically in [40]. All the literatures mentioned on non-symmetric waves were carried out by investigating spontaneous symmetry-breaking bifurcations mechanism. [53] worked on non-symmetric solitary waves with a quite different approach. They began with constructing an special initial guess for Newton's method and obtained a convergent solution, then the bifurcation diagram was completed based on a numerical continuation method. They found that all the non-symmetric solitary waves finally join the branches of symmetric solitary waves. Despite of a very different start, it ends up with another example of spontaneous symmetry-breaking bifurcations.

In the present Chapter, we aim to discover new non-symmetric gravity-capillary periodic waves numerically. The problem is formulated in Section 2.2. We state the numerical scheme in Section 3 based on a collocation technique which was firstly used by [47]. The numerical solutions and the global bifurcation diagrams are presented in full details in Section 8.2. The concluding remarks are given in Section 8.3.

8.1 Formulation

We consider a two-dimensional irrotational flow of an inviscid and incompressible fluid of finite depth h with gravity and surface tension both present. The free-surface (i.e. the upper surface of the fluid) is deformed by a train of waves travelling at a constant velocity c.

We introduce a two-dimensional cartesian system with the y-axis pointing upwards. A frame of reference moving with the waves is chosen so that the flow is steady. We denote by $y = \eta(x)$ the equation of the (unknown) free-surface. The acceleration of gravity g acts in the negative y-direction.

The governing equations are

$$\nabla^2 \phi = 0 \,, \qquad\qquad -h < y < \eta(x) \,, \qquad (8.1)$$

$$\phi_y = \phi_x \eta_x \,, \qquad\qquad \text{on } y = \eta(x) \,, \qquad (8.2)$$

$$\frac{1}{2}\left|\nabla\phi\right|^2 + gy - \frac{T}{\rho}\kappa = B \,, \qquad\qquad \text{on } y = \eta(x) \,, \qquad (8.3)$$

$$\phi_y = 0 \,, \qquad\qquad \text{on } y = -h \,, \qquad (8.4)$$

where T is the surface tension, κ is the curvature and ρ is the fluid density. Equation (8.2) and (8.4) are the kinematic boundary conditions on the free-surface and on the bottom respectively. Equation (8.3) is the Bernoulli equation on the free-surface or, in other words, the dynamic boundary condition and B is the Bernoulli constant.

We introduce the potential function ϕ and the streamfunction ψ. Then $f = \phi + i\psi$ denotes by the complex potential. We choose $\psi = 0$ on the free-surface and $\phi = 0$ at $x = y = 0$. In this chapter, we focus on the periodic waves with wavelength λ. Therefore we impose

$$\eta(x + \lambda) = \eta(x) \,, \qquad (8.5)$$

By choosing

$$c \quad \text{and} \quad \frac{\lambda}{2\pi} \tag{8.6}$$

as the reference velocity and length respectively, we rewrite the dynamic boundary condition (8.3) as

$$\frac{1}{2}\left|\nabla\phi\right|^2 + py - q\kappa = B, \quad \text{on } y = \eta(x), \tag{8.7}$$

where

$$p = \frac{g\lambda}{2\pi c^2} \quad \text{and} \quad q = \frac{2\pi T}{\rho\lambda c^2}. \tag{8.8}$$

We use (ϕ, ψ) as the independent variables. $w = u - iv$ denotes by the complex velocity. Then we introduce $\mathcal{T} - i\vartheta$, which is an analytic function of (ϕ, ψ) by the formula

$$u - iv = e^{\mathcal{T} - i\vartheta}. \tag{8.9}$$

On the free surface, we define $\tau(\phi) \triangleq \mathcal{T}(\phi, 0)$ and $\theta(\phi) \triangleq \vartheta(\phi, 0)$. It immediately follows that

$$x_\phi + iy_\phi = e^{-\tau + i\theta}, \tag{8.10}$$

whose real part and imaginary part can be used to compute x and y respectively by integrating with respect to ϕ. We substitute (8.9) and (8.10) into (8.7) and differentiate the result with respect to ϕ to get

$$e^{2\tau}\tau_\phi + pe^{-\tau}\sin\theta - q\frac{d}{d\phi}\left(e^\tau\theta_\phi\right) = 0, \tag{8.11}$$

where we have used $\kappa = e^\tau\theta_\phi$. An equivalent formulation was used in [40]. Their parameter θ was of opposite sign.

The linear dispersion relation for gravity-capillary waves is

$$c^2 = \frac{g}{k} + \frac{T}{\rho}k, \tag{8.12}$$

where k is the wavenumber. We note that c in (8.12) admits a minimum that is

$$c^* = \left(\frac{4Tg}{\rho}\right)^{\frac{1}{4}}.$$ (8.13)

This value is called the minimum phase speed at which solitary waves bifurcate. Or equivalently, when

$$pq = \frac{Tg}{\rho}\frac{1}{c^4} = \frac{1}{4}.$$ (8.14)

As shown in Chapter 6, solitary waves bifurcate from the minimum phase speed. Under scaling (8.8), (8.12) becomes

$$\widetilde{k} - p - \widetilde{k}^2 q = 0,$$ (8.15)

where $\widetilde{k}$ is the dimensionless wavenumber or the number of waves peaks within one wavelength.

We use the numerical method introduced in Section 3.1.3 to compute non-symmetric solutions. The challenge here is to find suitable initial guesses to jump on branches of non-symmetric waves. To find a symmetry-breaking point, we interpolate a symmetric solution $(\alpha_0, a_1, ..., a_N, q)$ with zero b_n coefficients. Then $(\alpha_0, a_1, ..., a_N, q, 0, 0, ..., 0)$ is still an exact solution of symmetric waves. We perform this operation along the symmetric branches and evaluate the Jacobian of the enlarged system with a_n and b_n all involved. Symmetry-breaking takes place when the Jacobian changes its sign. We name this operation the *non-symmetric Jacobian test*. By using (3.43) near a symmetry-breaking point, the solution converges after several iterations and a non-symmetric wave is obtained. Afterwards the whole bifurcation diagram can be completed by using the continuation method. In this paper, we choose $N = 500$ for computing symmetric waves and $N = 1000$ for non-symmetric waves. There are no significant changes in solutions by using a larger N. A solution is considered to be

converged if the l^∞-norm of the residual error of Newton's method is less than 10^{-9}.

8.2 Numerical results

8.2.1 Non-symmetric waves in deep water

[40] discovered numerically non-symmetric waves with 6 peaks and 2 peaks per wavelength resulting from the spontaneous symmetry-breaking bifurcations. As presented in their paper, a branch emanating from a linear wave solution which satisfies the dispersion relation for some integer wave number m is called a *primary branch* of mode m. If a further bifurcation occurs on a primary branch, it leads to a new family of solutions and is called a *secondary branch*. Analogously, a branch bifurcating from a secondary branch is called a *tertiary branch*. We denote the primary branch of mode m by P_m, the secondary branch of mode (m, n) by S_{mn} and the tertiary branch of mode (m, n, j) by T_{mnj}. The order of the index numbers essentially shows the solution structure, e.g. a T_{mnj} bifurcates from a S_{mn} which originates from P_m (see the following schematic)

$$P_m \to S_{mn} \to T_{mnj}. \tag{8.16}$$

We continue to investigate this problem by reproducing first the results in [40] and then by searching for new types of non-symmetric waves. We fix the value of p and change q in the continuation method. As described in §3, we depart from P_6 and perform the symmetric and non-symmetric Jacobian tests along the branch at the same time. A S_{62} is found but there is no non-symmetric branch. We continue the same work on S_{62} and find a T_{621}, but still there is no non-symmetric branch. Finally, on the tertiary branch T_{621}, we managed to find a symmetry-breaking point from which a non-symmetric branch emanates. A typical wave profile is shown in
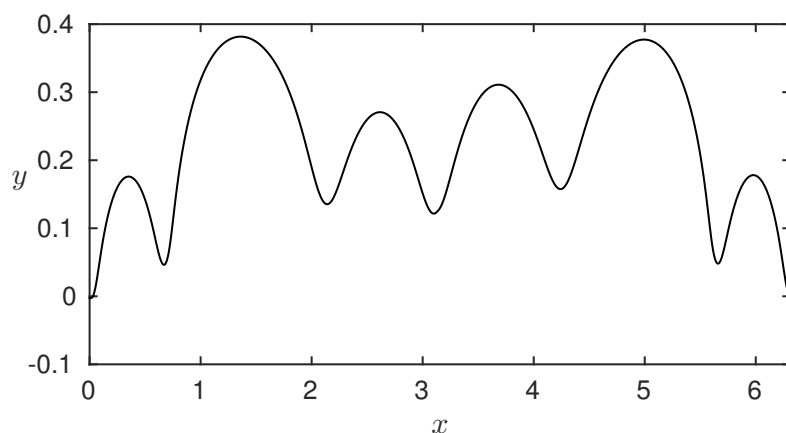
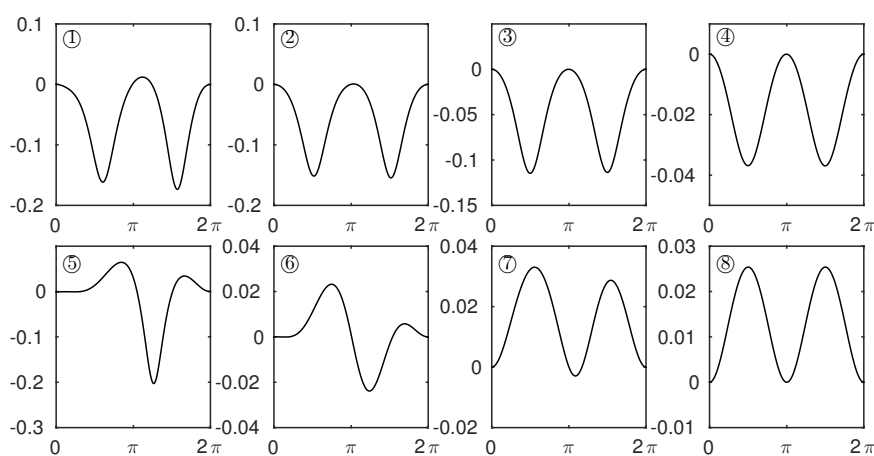Figure 8.1: A non-symmetric wave profile with 6 peaks in one wavelength with $p = 1.41$ and $q = 0.1376$.

Figure 8.2: Top: non-symmetric waves of 2 peaks on the branch bifurcating from the primary branch P_2 for $q = 0.2208$ and $p = 1.2, 1.18, 1.15, 1.12$ respectively (from ① to ④). Bottom: non-symmetric waves of 2 peaks on the branch bifurcating from S_{23} for $q = 0.2487$ and $p = 1.2, 1.01, 1.007, 1.006$ respectively (from ⑤ to ⑧). The profiles are plotted in the physical x-y plane.

figure 8.1 . The detailed bifurcation diagrams are shown in figure 4 and figure 5 of [40].

For non-symmetric waves with two peaks, there are two types: (1) those bifurcating from the primary branch P_2; (2) those bifurcating from the secondary branch S_{23}. Examples for both types are shown in figure 8.2. By using a continuation method in p for the non-symmetric branch of 2 peaks, we observe that the non-symmetry vanishes as the value of p decreases to a certain number.

In [8] the author obtained symmetric capillary-gravity solitary waves by extend-
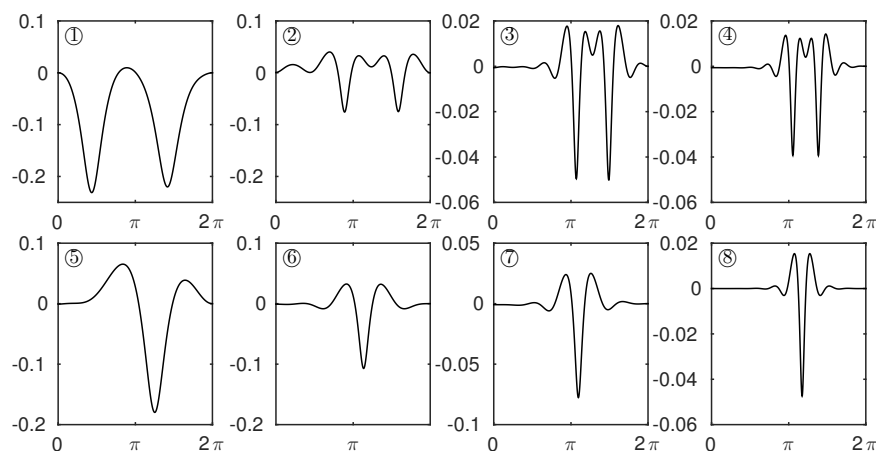
Figure 8.3: Top: non-symmetric waves with 2 peaks on the branch bifurcating from P_2 for $pq = 0.28$ and $p/q =$5.18, 21, 55, 89 respectively (from ① to ④). Bottom: non-symmetric waves with 2 peaks on the branch bifurcating from S_{23} for $pq = 0.29$ and $p/q = 5$, 16, 30, 80 respectively (from ⑤ to ⑧). The profiles are plotted in the physical x-y plane.

ing the wavelength of periodic waves. Inspired by this work, we perform the same procedure to see whether it is possible to find new non-symmetric solitary waves. This can be achieved in our problem by fixing the value of pq and enlarging p/q of a solution whose phase speed is less than the minimum of the phase speed, i.e. $pq > 1/4$. Unfortunately the asymmetry evanescences as the value of p/q is further increased, and the solution finally ends up with a shifted depression or elevation solitary wave (see figure 8.3). However this approach is found to be extremely useful for discovering new non-symmetric waves with more peaks. This is discussed in Section 8.2.1.1 and Section 8.2.1.2.

8.2.1.1 New non-symmetric waves

An immediate question which aroused following the work of [40] is: can we find non-symmetric waves with a number of peaks other than 2 or 6? The answer is positive. We start with presenting the results for 3 peaks. The symmetry-breaking point is found to be on an S_{32} branch. By following the branch of non-symmetric waves, the solution eventually joins a branch of shifted symmetric waves. A detailed bifurcation diagram is presented in the left graph of figure 8.4(a), and typical wave
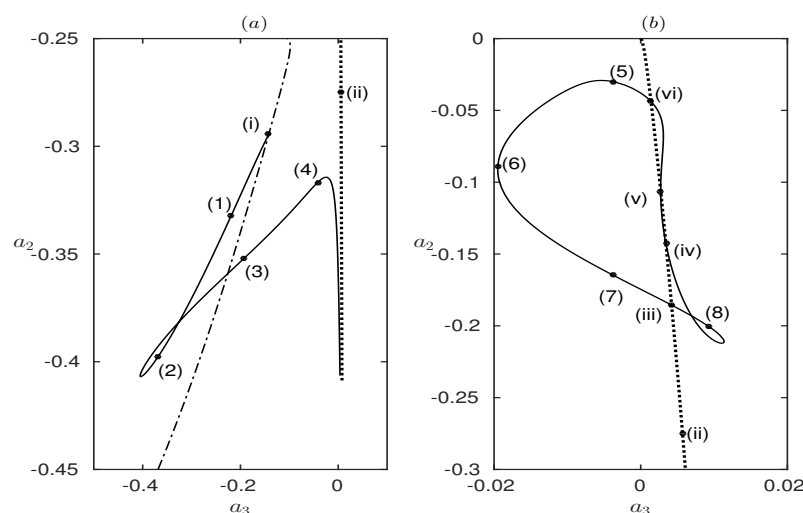
Figure 8.4: (a) Bifurcation diagram of non-symmetric waves with 3 peaks for $p = 1.2$. The solid curve is a branch of non-symmetric waves with 3 peaks in a wavelength. The dash-dotted curve is a branch of symmetric waves of mode (3,2) whereas the dotted curve corresponds to a branch of shifted symmetric waves. (b) Continuation of the dotted branch of shifted symmetric waves. The solid curve is a branch of non-symmetric waves with 4 peaks.

profiles are shown in figure 8.5.

By following further the branch of shifted symmetric waves, we discover a new branch of non-symmetric waves with 4 peaks. The full bifurcation diagram is shown in figure 8.4(b) and typical wave profiles are sketched in figure 8.6. We notice that the dotted curve in the right graph of Figure 8.4 finally tends to the origin, which implies that this type of shifted waves with 4 peaks can only bifurcate from the uniform stream. This is the reason why one cannot obtain these results with 4 wave peaks by the routine approach for the symmetry-breaking study.

The bifurcations for non-symmetric waves with 5 and 7 peaks are qualitatively similar to those with 3 peaks. They both emanate from a secondary branch (S_{54} and S_{76} respectively) and end at a branch of shifted symmetric waves (see figure 8.7). Due to large wave amplitudes, overhanging structures are observed. A large number of collocation points is required to maintain the high accuracy near the dotted curves in both graphs of figure 8.7. A typical value for N there is 3000.

A further extension is to find non-symmetric waves with more peaks. It can be
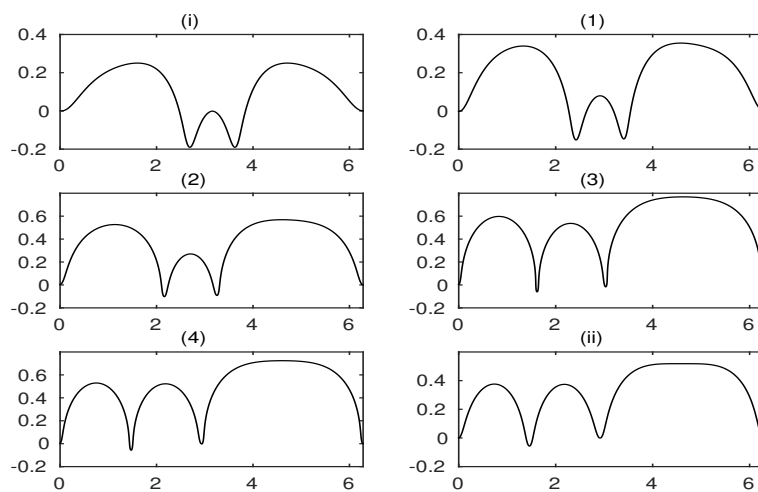
Figure 8.5: Wave profiles for those points indicated in figure 8.4(a). They are plotted in the x-y plane.

Figure 8.6: Wave profiles for those points indicated in figure 8.4(b). They are plotted in the x-y plane.

Figure 8.7: (a) Bifurcation diagram of non-symmetric waves with 5 peaks for $p = 1$. The solid curve is the branch of non-symmetric waves with 5 peaks. The dotted curve is part of the S_{54} branch. The dashed curve is part of a branch of shifted symmetric waves. (b) Bifurcation diagram of non-symmetric waves with 7 peaks for $p = 1.05$. The solid curve is the branch of non-symmetric waves with 7 peaks. The dashed curve is part of the S_{76} branch. The dotted curve is part of a branch of shifted symmetric waves.
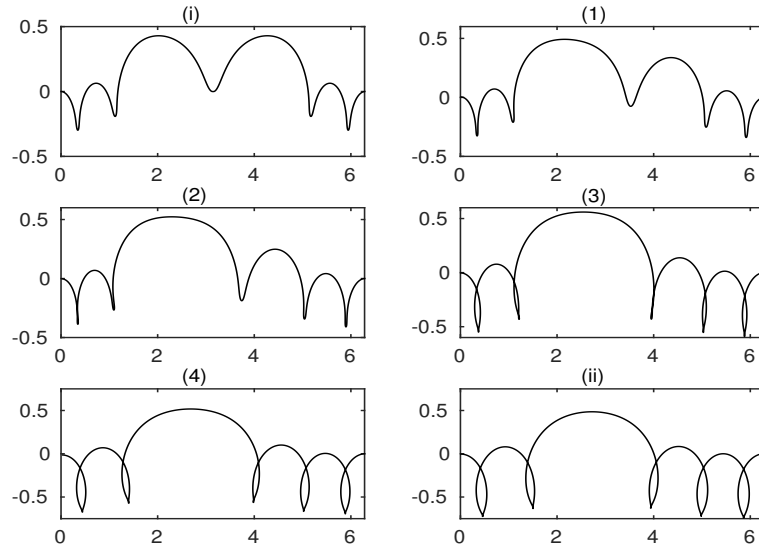
Figure 8.8: Wave profiles for the points indicated in figure 8.7(a). They are plotted in the x-y plane.

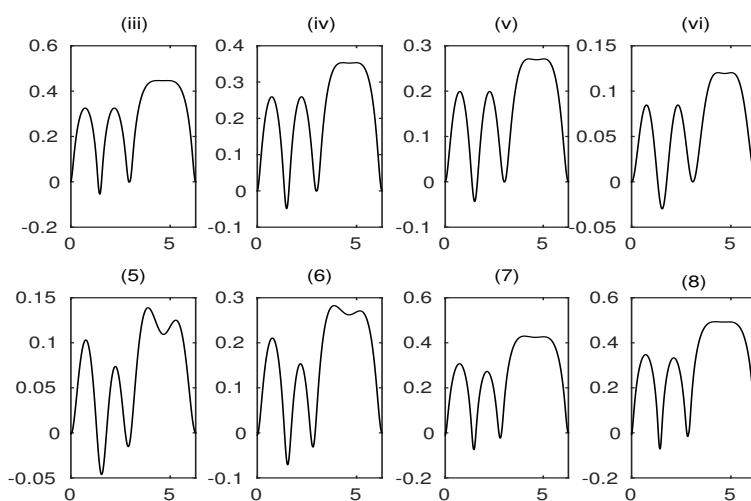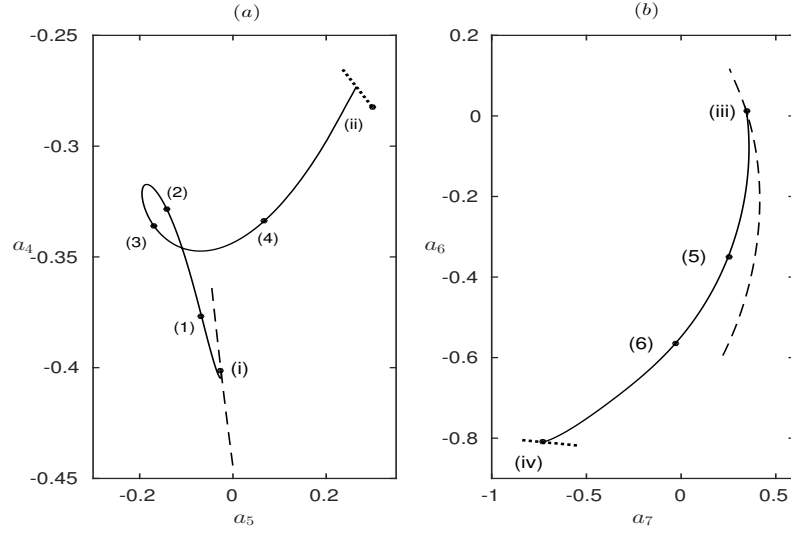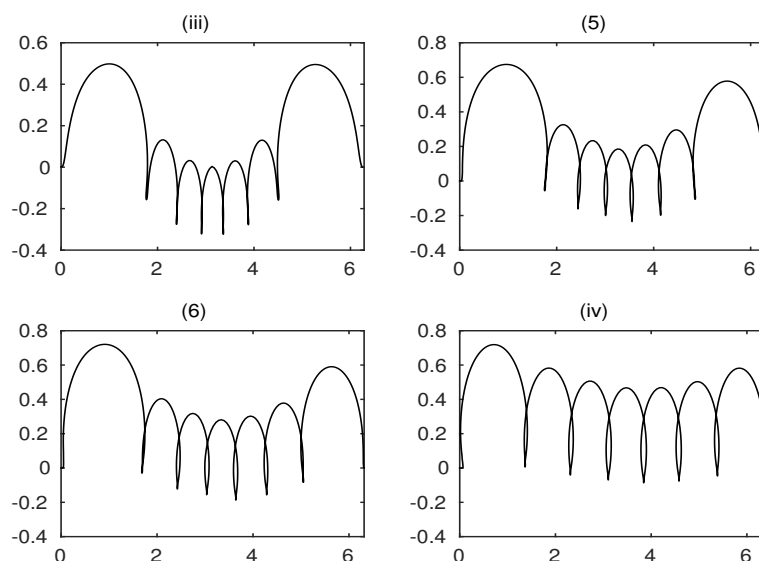Figure 8.9: Wave profiles for the points indicated in figure 8.7(b). They are plotted in the x-y plane.
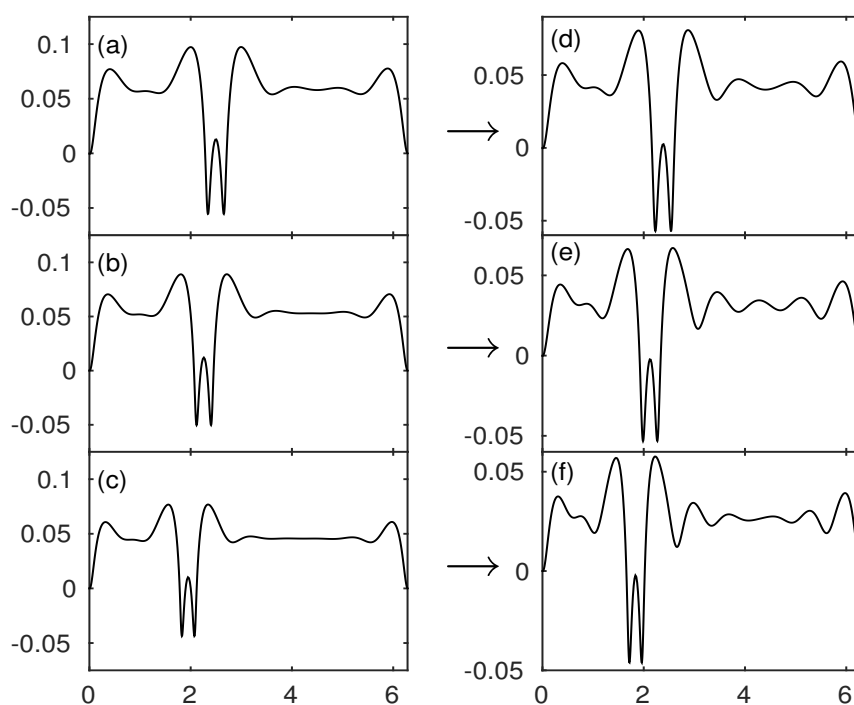

Figure 8.10: Examples of extending the non-symmetric wave (7) from figure 8.6. The value of pq is fixed to be 0.2847 and p/q is equal to (a) 55, (b) 60, (c) 70. These solutions lead to non-symmetric waves with (d) 8 peaks, (e) 9 peaks and (f) 10 peaks respectively. The profiles are plotted in the x-y plane.
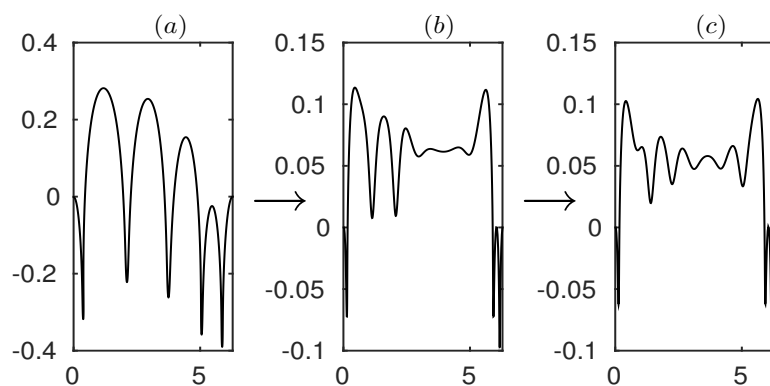
Figure 8.11: Example of extending a non-symmetric wave with 5 peaks. (a) $p = 1.3113$ $q = 0.2110$, (b) $p = 3.8045$ $q = 0.0727$, (c) $p = 3.8045$ and $q = 0.0660$. The profiles are plotted in the x-y plane.

achieved by fixing the value of pq and increasing the value of p/q (as seen in figure 8.3). We apply the approach to those non-symmetric waves presented in Section 8.2.1.1, and observe that a large peak evolves to two ripples with a long flat platform generated in between as shown in figure 8.10(a). We stop at some value of p/q and take the solution as the initial guess. Then by fixing the value of p and varying q, some new waves can be found. We perform our first numerical experiment with the non-symmetric wave presented in figure 8.6(7). Three new kinds of waves are obtained for different values of p/q as presented in figure 8.10(a,b,c). As the value of p/q increases, the number of peaks generated increases. Therefore a further increase of p/q leads to a new solution with more peaks. We have a reason to believe that non-symmetric waves can exist with any integer number of peaks. Although no rigorous proof is provided, the results show very strong numerical evidence. This approach can also be applied to other non-symmetric waves. We take a non-symmetric wave with 5 peaks and $p = 1.29$, $q = 0.2145$ for example. This wave bifurcates from a branch of shifted symmetric waves. Here we do not present the detailed bifurcation structure since it is qualitatively similar to the one with 3 peaks. We fix the value of pq and change p/q to (a) 6.2146 (b) 52.3146 as shown in figure 8.11. Then we use wave (b) as an initial guess and fix the value p to follow the branch where new non-symmetric waves are obtained. A new non-symmetric wave with 9 peaks is presented
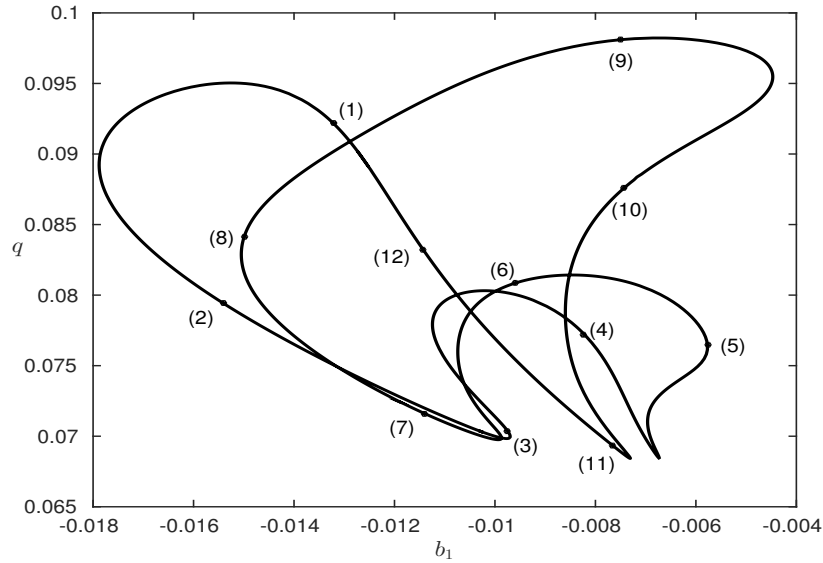
Figure 8.12: The isolated branch of a family of non-symmetric waves plotted in the b_1-q plane. The value of p is fixed to be 3.7560. All the waves from this branch are non-symmetric. Some typical wave profiles are sketched in figure 8.13.

in figure 8.11 (c).

8.2.1.2   Isolated branches of non-symmetric waves

We now focus on the non-symmetric wave with 8 peaks as shown on the top right of figure 8.10. By continuation, we obtain the whole family of solutions and sketch them by using b_1 and q as the parameters in figure 8.12. Upon the branch, the wave tries to balance both sides to recover the symmetry but it fails (see figure 8.13). As a consequence, it has no choice but to rejoin its own branch of non-symmetric waves. The branch of non-symmetric waves is found to be a closed loop which is isolated without the presence of branch of symmetric waves as shown in figure 8.12. Several bifurcation points have been found on this isolated non-symmetric branch, which are marked as (1)-(5) in figure 8.14. The new bifurcation branches (dotted and dash-dotted lines shown in figure 8.14) are also non-symmetric waves. In particular, a simple closed branch which bifurcates from the point (4) or (5) has been observed (dashed curve in figure 8.14). We have not completed the branches which bifurcated

Figure 8.13: Wave profiles for the points indicated in figure 8.12. They are plotted in the physical x-y plane.

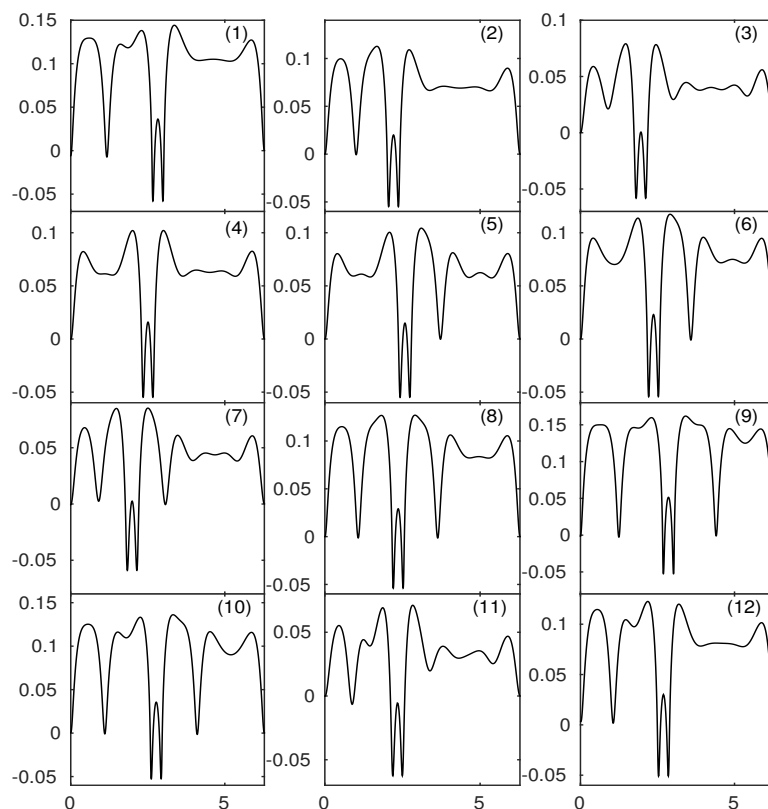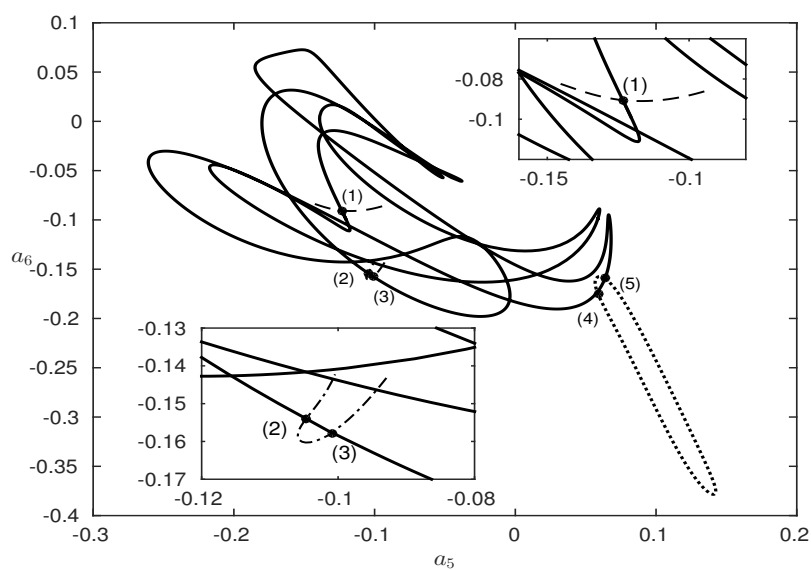Figure 8.14: Other bifurcations occurring on the isolated non-symmetric branch which was presented in figure 8.12. We plot in the a_5-a_6 plane instead of the b_1-q plane to make the bifurcations easier for view.
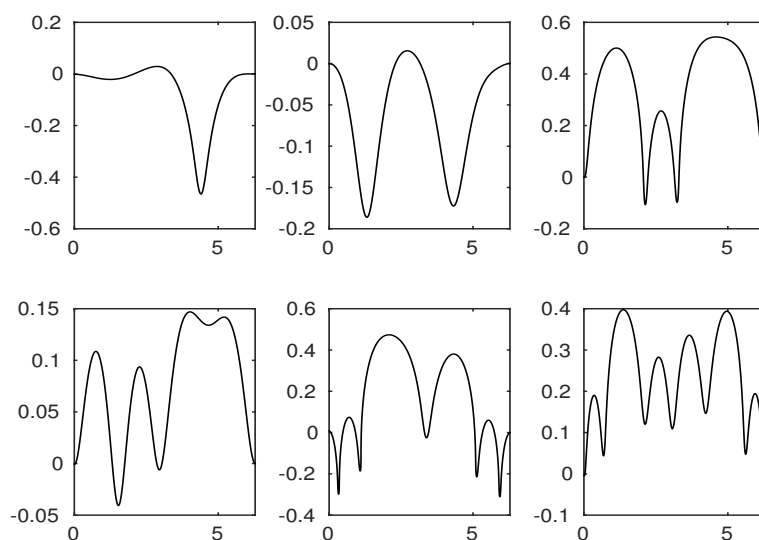
Figure 8.15: Non-symmetric waves in water of finite depth for $h = 3$.

at point (1) and (2) or (3) but we expect that they will form an isolated branch of non-symmetric waves or join a branch of (shifted) symmetric waves. Besides we also investigated the branches arising from the non-symmetric waves with 9 and 10 peaks (figure 8.10(e, f)). The solution structures are qualitatively similar. Isolated non-symmetric branches are also found.

To generalise the results to water of finite depth, we only need to use the solutions in deep water as an initial guess and treat the depth h as a parameter in the continuation method. Without much effort, many different non-symmetric waves are obtained. Some typical profiles for $h = 3$ are plotted in figure 8.15. The existence of non-symmetric waves in water of finite depth is confirmed. However we have not followed the branch to compute the complete bifurcation diagrams since the structures are qualitatively similar to those in deep water.

8.3   Discussion

We started by reproducing the results for 2 peaks and 6 peaks of [40]. By using the same mechanism for symmetry-breaking investigation, we have found new branches

of non-symmetric waves with 3, 4, 5 and 7 peaks. These waves are in general of large amplitudes, and all appear via spontaneous symmetry-breaking bifurcations. An approach which is equivalent to the method of extending the wavelength is introduced to discover more new solutions. Besides we have found isolated closed branches of non-symmetric waves without symmetry breaking involved. It illustrates the fact that the presence of non-symmetric waves can not only be from symmetry-breaking but also in the form of an isolated loop. A future possible work is to study the existence of non-symmetry generalised solitary waves. A future possible work is to find non-symmetric generalised solitary waves. This is introduced in Chapter 9.

Chapter 9

Future possible work

We have already seen non-symmetric solitary flexural-gravity waves in Section 6.3 , non-symmetric solitary gravity-capillary waves in [53] and non-symmetric periodic gravity-capillary waves in Chapter 8 . Can generalised solitary waves exist with non-symmetries? It remains an interesting and open question. This problem seems to be more difficult since the ripples of generalised solitary waves on each side need to be well balanced and remain at the same amplitude. We expect that the answer is positive. A recently obtained result is presented in figure 9.1 .
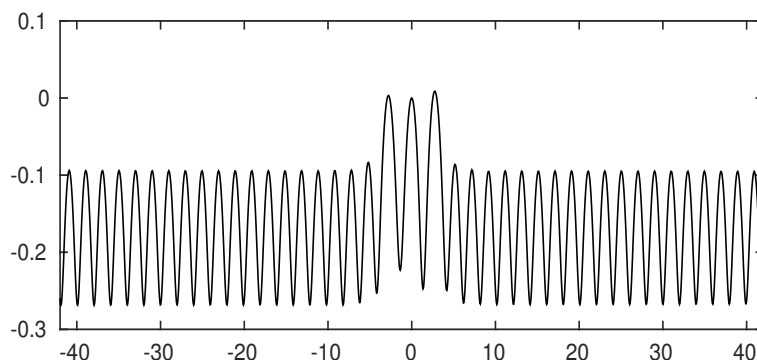
Figure 9.1: A non-symmetric generalised solitary wave profile with $B = 0.28$ where B is the Bond number. Only the main profile is shown.

We continue to work on this problem seriously. Many more new non-symmetric waves are expected to be found.

Appendix A

Derivation of the equations of motion

A.1 Euler's Equations

We consider an inviscid fluid with density $\rho(\mathbf{x}, t)$ and velocity $\mathbf{u}(\mathbf{x}, t)$. V is a control volume with boundary S. Then it satisfies

$$\iiint_V \frac{\partial \rho}{\partial t} \, dV + \iint_S \rho \mathbf{u} \, d\mathbf{S} = 0, \tag{A.1}$$

where the first term is the rate of change of the mass and the second term equals the flux flowing outwards across the boundary, i.e. the direction of $d\mathbf{S}$ is taken to be outwards. By applying the divergence theorem to the double integral, (A.1) becomes

$$\iiint_V \left(\frac{\partial \rho}{\partial t} + \nabla.(\rho \mathbf{u}) \right) \, dV = 0. \tag{A.2}$$

Since V is arbitrarily chosen, the integrand must be pointwise equal to zero, i.e.

$$\frac{\partial \rho}{\partial t} + \nabla.(\rho \mathbf{u}) = 0. \tag{A.3}$$

(A.3) is called the continuity equation or the equation of conservation of mass. With a further assumption on the incompressibility, the continuity equation is simplified as

$$\nabla.\mathbf{u} = 0. \tag{A.4}$$

The rate of change of the momentum can be written as

$$\iiint_V \frac{\partial}{\partial t}(\rho\mathbf{u}) \; dV. \tag{A.5}$$

This quantity is caused by the momentum flowing across the boundary, the pressure effect and the body forces due to the gravitational field whose expressions are respectively given by

$$-\iint_S (\rho\mathbf{u})\mathbf{u} \; d\mathbf{S} - \iint_S p \; d\mathbf{S} + \iiint_V \rho\mathbf{g} \; dV, \tag{A.6}$$

where p is the pressure and $\mathbf{g}$ is the acceleration due to gravity. By using the divergence theorem, (A.6) becomes

$$\iiint_V -\mathbf{u}\nabla.(\rho\mathbf{u}) - \rho\mathbf{u}\nabla.(\mathbf{u}) - \nabla p + \rho\mathbf{g} \; dV. \tag{A.7}$$

We equate (A.5) and (A.7) then their integrands must be identical because of the arbitrary control volume V. It gives

$$\rho\frac{\partial\mathbf{u}}{\partial t} + \mathbf{u}\frac{\partial\rho}{\partial t} + \mathbf{u}\nabla.(\rho\mathbf{u}) + \rho\mathbf{u}\nabla.(\mathbf{u}) = -\nabla p + \rho\mathbf{g}. \tag{A.8}$$

The second term and the third term vanish by using the continuity equation (A.3). The momentum equation finally reads

$$\frac{D\mathbf{u}}{Dt} = -\frac{1}{\rho}\nabla p + \mathbf{g}, \tag{A.9}$$

where $\frac{D\mathbf{u}}{Dt} = \frac{\partial \mathbf{u}}{\partial t} + \mathbf{u}\nabla.\mathbf{u}$ is the material derivative of $\mathbf{u}$. This system of equations are the so-called Euler's equations. We rewrite the gravity as the gradient of a potential Ω,

$$\mathbf{g} = -\nabla\Omega. \tag{A.10}$$

With the help of the following identity

$$(\mathbf{u}.\nabla)\mathbf{u} = (\nabla \times \mathbf{u}) \times \mathbf{u} + \nabla(\frac{1}{2}\mathbf{u}^2), \tag{A.11}$$

the momentum equation (A.9) can be expressed as

$$\frac{\partial \mathbf{u}}{\partial t} + (\nabla \times \mathbf{u}) \times \mathbf{u} + \nabla(\frac{p}{\rho} + \frac{1}{2}\mathbf{u}^2 + \Omega) = 0. \tag{A.12}$$

With a further assumption on irrotationality, i.e. $\nabla \times \mathbf{u} = 0$, we can introduce a potential function ϕ such that

$$\mathbf{u} = \nabla\phi. \tag{A.13}$$

By integrating (A.12) with respect to spatial variables, we derive an integral version of Euler's equation which is called the Bernoulli equation

$$\frac{\partial \phi}{\partial t} + \frac{p}{\rho} + \frac{1}{2}\mathbf{u}^2 + \Omega = B, \tag{A.14}$$

where B on the right hand side is the Bernoulli constant.

A.2 Korteweg-de Vries Equation

In this section, we present the detailed derivation of the famous model for long waves. We start by introducing

$$\widetilde{x} = \frac{x}{l}, \ \ \widetilde{y} = \frac{y}{h}, \ \ \widetilde{\eta} = \frac{\eta}{a}, \ \ \widetilde{t} = \frac{c_0}{l}t \ \text{ and } \ \widetilde{\phi} = \frac{h}{c_0 la}\phi = \frac{c_0}{gla}\phi \qquad (A.15)$$

as the variables. α and β are two parameters defined by

$$\alpha = \frac{a}{h}, \qquad \beta = \frac{h^2}{l^2}. \qquad (A.16)$$

To obtain the fifth order KdV equation, it is required that the coefficient of the fifth order term η_{xxxxx} must be balanced by that of the nonlinear term $\eta\eta_x$ (see [20]). As a result, we have

$$\alpha \sim \beta^2. \qquad (A.17)$$

We first take on the gravity-capillary problem. The governing equations (8.1)-(8.4) are rescaled as

$$\beta\phi_{xx} + \phi_{yy} = 0, \qquad\qquad -1 < y < \alpha\eta, \qquad (A.18)$$

$$\phi_y = 0, \qquad\qquad y = -1, \qquad (A.19)$$

$$\eta_t - \frac{1}{\beta}\phi_y + \alpha\phi_x\eta_x = 0, \qquad\qquad y = \alpha\eta, \qquad (A.20)$$

$$\phi_t + \eta + \frac{1}{2}\left(\alpha\phi_x^2 + \frac{\alpha}{\beta}\phi_y^2\right) - \tau\beta\eta_{xx}\left(1 + \alpha^2\beta\eta_x^2\right)^{-\frac{3}{2}} = B, \qquad y = \alpha\eta, \qquad (A.21)$$

where we have dropped tilde for ease. The boundary condition (A.21) enables us to write

$$\phi(x, y, t) = \sum_{n=0}^{\infty}(1 + y)^n f_n(x, t). \qquad (A.22)$$

We plug this form into equation (A.18) to get

$$f_1 = -0, \tag{A.23}$$

$$f_{n+2} = \frac{-\beta}{(n+2)(n+1)} \frac{\partial^2 f_n}{\partial x^2}. \tag{A.24}$$

Hence

$$\phi = f - \frac{\beta}{2}\beta(y+1)^2 f_{xx} + \frac{\beta^2}{24}(y+1)^4 f_{xxxx} - \frac{\beta^3}{720}(y+1)^6 f_{xxxxxx} + O(\beta^4), \tag{A.25}$$

where $f = f_0(x,t) = \phi(x,-1,t)$. We denote w by the horizontal velocity at the lower solid boundary. It immediately follows that

$$w = f_x. \tag{A.26}$$

By substituting (A.25) into (A.20), it gives

$$\eta_t + w_x - \frac{1}{6}\beta w_{xxx} + \frac{1}{120}\beta^2 w_{xxxxx} + \alpha(\eta w)_x + O(\beta^3) = 0 \tag{A.27}$$

Similarly we use (A.25) in (A.21) and differentiate with respect to x. It gives

$$\eta_x + w_t - \beta(\frac{1}{2}w_{xxt} + \tau\eta_{xxx}) + \frac{1}{24}\beta^2 w_{xxxxt} + \alpha w w_x + O(\beta^3) = 0. \tag{A.28}$$

At the leading order, we have

$$\eta_t + w_x = 0, \tag{A.29}$$

$$\eta_x + w_t = 0. \tag{A.30}$$

Apprently, $w = \eta$ is a solution describing a right-moving wave. Then we search for a solution in the form of

$$w = \eta + \alpha A(x,t) + \beta B(x,t) + \beta^2 C(x,t) + O(\beta^3). \tag{A.31}$$

It follows that (A.27) and (A.28) become

$$\eta_t + \eta_x + \beta(B_x - \frac{1}{6}\eta_{xxx}) + \beta^2(C_x - \frac{1}{6}B_{xxx} + \frac{1}{120}\eta_{xxxxx}) + \alpha(A_x + 2\eta\eta_x) + O(\beta^3) = 0 \tag{A.32}$$

and

$$\eta_x + \eta_t + \beta(B_t - \frac{1}{2}\eta_{xxt} - \tau\eta_{xxx}) + \beta^2(C_t + \frac{1}{24}\eta_{xxxxt} - \frac{1}{2}B_{xxt}) + \alpha(A_t + \eta\eta_x) + O(\beta^3) = 0 \tag{A.33}$$

respectively. We first match the coefficients of α and β in (A.32) and (A.33). It gives the following two solvability conditions

$$A_x + 2\eta\eta_x = A_t + \eta\eta_x, \tag{A.34}$$

$$B_x - \frac{1}{6}\eta_{xxx} = B_t - \frac{1}{2}\eta_{xxt} - \tau\eta_{xxx}. \tag{A.35}$$

We also know from (A.31) that

$$\frac{\partial}{\partial t} + \frac{\partial}{\partial x} + O(\alpha) + O(\beta) = 0. \tag{A.36}$$

Therefore we derive from (A.34) and (A.35) that

$$A = -\frac{1}{4}\eta^2, \tag{A.37}$$

$$B = (\frac{1}{3} - \frac{\tau}{2})\eta_{xx}. \tag{A.38}$$

By substituting (A.37) and (A.38) into (A.32), it yields

$$\eta_t = -\eta_x - \frac{3}{2}\alpha\eta\eta_x - \beta(\frac{1}{6} - \frac{\tau}{2})\eta_{xxx} + O(\beta^2).$$ (A.39)

Using (A.39) to evaluate the time derivatives on the right hand side of (A.35) produces extra terms

$$\frac{1}{36}(1 - 9\tau^2)\eta_{xxxxx}$$ (A.40)

of $O(\beta^2)$ which appears in equation (A.33). By collecting the coefficients of β^2 from (A.32) and (A.33) together with the extra terms (A.40), we obtain the third solvability condition

$$C_x - \frac{1}{6}B_{xxx} + \frac{1}{120}\eta_{xxxxx} = C_t + \frac{1}{24}\eta_{xxxxt} - \frac{1}{2}B_{xxt} + \frac{1}{36}(1 - 9\tau^2)\eta_{xxxxx}.$$ (A.41)

After some elementary algebra, it gives

$$C = \frac{1}{120}(12 - 20\tau - 5\tau^2)\eta_{xxxx}.$$ (A.42)

Finally we substitute (A.37), (A.38) and (A.42) into (A.32) and eliminate the higher order terms. This gives the fifth order KdV equation

$$\eta_t + \eta_x + \frac{3}{2}\alpha\eta\eta_x + \frac{1}{6}\beta(1 - 3\tau)\eta_{xxx} + \frac{1}{360}\beta^2(19 - 30\tau - 45\tau^2)\eta_{xxxxx} = 0.$$ (A.43)

In real variables, it reads

$$\eta_t + c_0\eta_x + \frac{3}{2}\frac{c_0}{h}\eta\eta_x + \frac{c_0 h^2}{6}(1 - 3\tau)\eta_{xxx} + \frac{c_0 h^4}{360}(19 - 30\tau - 45\tau^2)\eta_{xxxxx} = 0.$$ (A.44)

When τ is not close to $\frac{1}{3}$, the fifth derivative term can be discarded so that the equation turns out to be the standard KdV equation.

For the flexural-gravity problem, everything remains the same except the term of surface tension is replaced by the flexural term. (A.18)-(A.20) are still valid but (A.21) is replaced by

$$\phi_t + \eta + \frac{1}{2}\left(\alpha\phi_x^2 + \frac{\alpha}{\beta}\phi_y^2\right) + \sigma\beta^2\eta_{xxxx} = B, \qquad y = \alpha\eta, \tag{A.45}$$

We have used the linear model (2.22) here and $\sigma = \frac{D}{\rho g h^4}$. One may also use other models such as (2.18) or (2.20). However, the expansions in α and β agree up to order of β^2 no matter which model is being used. Therefore the choice among the models makes no difference in deriving the fifth order KdV equation. With the same process as presented earlier, we have

$$\eta_t + \eta_x + \frac{3}{2}\alpha\eta\eta_x + \frac{1}{6}\beta\eta_{xxx} + \beta^2\left(\frac{19}{360} + \frac{\sigma}{2}\right)\eta_{xxxxx} = 0, \tag{A.46}$$

or in real variables

$$\eta_t + c_0\eta_x + \frac{3}{2}\frac{c_0}{h}\eta\eta_x + \frac{1}{6}c_0 h^2\eta_{xxx} + \left(\frac{19}{360} + \frac{\sigma}{2}\right)c_0 h^4\eta_{xxxxx} = 0. \tag{A.47}$$

From (A.46), we note that σ is required to be of $O(1/\beta)$ to balance the last three terms.

Appendix B

Derivation of the time-dependent numerical scheme

In this appendix, we present the details of deriving equations (3.58) and (3.59). We recall that the governing equations (2.3), (3.48), (2.6) and (3.51) under scaling (3.50). In order to compute the unknown free-surface, we introduce a time-dependent conformal map from the physical domain to the lower half plane with horizontal coordinate ξ and vertical coordinate η. Such a method has been used in [30], [10], [29], [5] and [26]. The conformal map can be found by solving

$$y_{\xi\xi} + y_{\eta\eta} = 0 \qquad\qquad \eta < 0, \qquad\qquad \text{(B.1)}$$

$$y(\xi, 0, t) = Y(\xi, t) \qquad\qquad \eta = 0, \qquad\qquad \text{(B.2)}$$

$$y \sim \eta \qquad\qquad \eta \to -\infty, \qquad\qquad \text{(B.3)}$$

where $Y(\xi, t) = \zeta(x(\xi, 0, t), t)$. We define $X(\xi, t) \equiv x(\xi, 0, t)$ on the free-surface.

Then we perform harmonic analysis. By writing $y(\xi, \eta, t) = \widetilde{y}(\xi, \eta, t) + \eta$, (B.1)-(B.3) become

$$\widetilde{y}_{\xi\xi} + \widetilde{y}_{\eta\eta} = 0 \qquad\qquad \eta < 0, \qquad\qquad \text{(B.4)}$$

$$\widetilde{y}(\xi, 0, t) = Y(\xi, t) \qquad\qquad \eta = 0, \tag{B.5}$$

$$\frac{\widetilde{y}}{\eta} \to 0 \qquad\qquad \eta \to -\infty. \tag{B.6}$$

By performing the Fourier transform to (B.4), (B.5) and (B.6), we obtain

$$-k^2 \widehat{\widetilde{y}}(k, \eta, t) + \widehat{\widetilde{y}_{\eta\eta}} = 0 \qquad\qquad \eta < 0, \tag{B.7}$$

$$\widehat{\widetilde{y}}(k, 0, t) = \widehat{Y}(k, t) \qquad\qquad \eta = 0, \tag{B.8}$$

$$\frac{\widehat{\widetilde{y}}}{\eta} \to 0 \qquad\qquad \eta \to -\infty, \tag{B.9}$$

where we denote

$$\widehat{\widetilde{y}}(k) = \mathsf{F}[\widetilde{y}(\xi)] = \int_{-\infty}^{\infty} \widetilde{y}(\xi) e^{-ik\xi} d\xi \tag{B.10}$$

by the Fourier transform of $\widetilde{y}$.

When $k = 0$, we can easily get

$$\widehat{\widetilde{y}}(0, \eta, t) = \text{constant} = \widehat{Y}(0, t). \tag{B.11}$$

When $k \neq 0$, (B.7) is a second-order ordinary differential equation with constant coefficients. The solution is

$$\widehat{\widetilde{y}}(k, \eta, t) = c_1 e^{|k|\eta} + c_2 e^{-|k|\eta}. \tag{B.12}$$

By imposing the boundary condition (B.8) and (B.9), we end up with

$$c_2 = 0, \tag{B.13}$$

$$c_1 = \widehat{Y}(k, t). \tag{B.14}$$

Therefore the Fourier transform of $\widetilde{y}$ can be written as

$$\widehat{\widetilde{y}}(k, \eta, t) = \widehat{Y}(k, t)e^{|k|\eta}. \tag{B.15}$$

Applying the inverse Fourier transform yields

$$\widetilde{y}(\xi, \eta, t) = \int_{-\infty}^{\infty} \widehat{Y}(k, t)e^{|k|\eta}e^{ik\xi}dk. \tag{B.16}$$

Hence

$$y(\xi, \eta, t) = \eta + \int_{-\infty}^{\infty} \widehat{Y}(k, t)e^{|k|\eta}e^{ik\xi}dk. \tag{B.17}$$

$z = x(\xi, \eta, t) + iy(\xi, \eta, t)$ is an analytic function of $\xi + i\eta$ therefore Cauchy-Riemann equations apply, i.e.

$$x_\xi = y_\eta, \tag{B.18}$$

$$x_\eta = -y_\xi. \tag{B.19}$$

We differentiate (B.16) with respect to η and combine with (B.18) to get

$$x_\xi = 1 + \int_{-\infty}^{\infty} \widehat{Y}(k, t)|k|e^{|k|\eta}e^{ik\xi}dk. \tag{B.20}$$

In particular on the free-surface, i.e. $\eta = 0$, we have

$$X_\xi = 1 + \int_{-\infty}^{\infty} \widehat{Y}(k, t)|k|e^{ik\xi}dk \tag{B.21}$$

$$= 1 - \int_{-\infty}^{\infty} i\,\mathrm{sgn}(k)\widehat{Y}(k, t)ike^{ik\xi}dk \tag{B.22}$$

The Hilbert transform is defined as

$$\mathcal{H}[f] = \int_{-\infty}^{\infty} \frac{f(\xi, 0, t)}{\xi' - \xi}d\xi. \tag{B.23}$$

By definition, we immediately have

$$\mathcal{H}[f] = \mathsf{F}^{-1}[i\mathrm{sgn}(k)\mathsf{F}[f]] \tag{B.24}$$

where $\mathsf{F}(f)$ denotes the Fourier transform of f. Using (B.24) in (B.22) yields

$$X_\xi = 1 - \mathcal{H}[Y_\xi]. \tag{B.25}$$

This is a harmonic relation between X and Y. Next we try to do the similar calculations for the complex potential $F = \phi + i\psi$ where ψ is the streamfunction. F is an analytic function in z and $z(\xi + i\eta, t) = x(\xi, \eta, t) + iy(\xi, \eta, t)$ is an analytic function in $\xi + i\eta$. Thus F is also analytic in $\xi + i\eta$, which implies that the complex potential satisfies the Laplace equation whose real part gives

$$\phi_{\xi\xi} + \phi_{\eta\eta} = 0. \tag{B.26}$$

We define $\phi(\xi, 0, t) \equiv \Phi(\xi, t)$ on the free-surface. By using the chain rule, we get

$$\phi_\eta = \phi_x x_\eta + \phi_y y_\eta = \phi_x x_\eta, \tag{B.27}$$

where we have used $\phi_y = 0$ by (2.6). By (B.19),

$$x_\eta = -y_\xi = -\int_{-\infty}^{\infty} \widehat{Y}(k,t)e^{|k|\eta}e^{ik\xi}(ik)dk. \tag{B.28}$$

We note that $e^{|k|\eta}$ decays exponentially as $\eta \to -\infty$ so does x_η. Hence we obtain a new boundary condition by (B.27),

$$\phi_\eta \to 0 \quad \text{as } \eta \to -\infty. \tag{B.29}$$

So the harmonic boundary value problem for ϕ can be defined as

$$\phi_{\xi\xi} + \phi_{\eta\eta} = 0 \qquad\qquad \eta < 0, \tag{B.30}$$

$$\phi(\xi, 0, t) \equiv \Phi(\xi, t) \qquad\qquad \eta = 0, \tag{B.31}$$

$$\phi_\eta \to 0 \qquad\qquad \eta \to -\infty. \tag{B.32}$$

By performing the Fourier transform to (B.30)-(B.32),

$$-k^2\widehat{\phi} + \widehat{\phi}_{\eta\eta} = 0 \qquad\qquad \eta < 0, \tag{B.33}$$

$$\widehat{\phi}(k, 0, t) = \widehat{\Phi}(k, t) \qquad\qquad \eta = 0, \tag{B.34}$$

$$\widehat{\phi}_\eta \to 0 \qquad\qquad \text{as } \eta \to -\infty. \tag{B.35}$$

(B.33) is a second-order ordinary differential equation with constant coefficients with boundary conditions (B.34) and (B.35). As have been seen before, we need to first consider $k = 0$. In this case, the solution is simply

$$\widehat{\phi}(0, \eta, t) = \text{constant} = \widehat{\Phi}(0, t). \tag{B.36}$$

When $k \neq 0$, it is easy to find that

$$\widehat{\phi}(k, \eta, t) = \widehat{\Phi}(k, t)e^{|k|\eta}. \tag{B.37}$$

By performing the inverse Fourier transform, we get

$$\phi = \int_{-\infty}^{\infty} \widehat{\phi}(k, t)e^{|k|\eta}e^{ik\xi}dk. \tag{B.38}$$

Since the streamfunction ψ is the harmonic conjugate of the velocity potential ϕ,

they satisfy the Cauchy-Riemann equations. Then we have

$$\psi_\xi = -\phi_\eta = \int_{-\infty}^{\infty} |k| \widehat{\phi}(k,t) e^{|k|\eta} e^{ik\xi} dk. \tag{B.39}$$

Paricularly on the free-surface, (B.39) becomes

$$\Psi_\xi = \int_{-\infty}^{\infty} (i\,\mathrm{sgn}(k))(ik)\widehat{\Phi}(k,t) e^{ik\xi} dk. \tag{B.40}$$

By using (B.24) in (B.40), we obtain the second harmonic relation

$$\Psi_\xi = \mathcal{H}[\Phi_\xi]. \tag{B.41}$$

Next we need to rewrite the time-evolution equations for Y and Φ. We recall that $Y(\xi,t) \equiv \zeta(x(\xi,0,t),t)$, $\Phi(\xi,t) = \phi(x(\xi,0,t),y(\xi,0,t),t)$ and $\Psi(\xi,t) = \psi(x(\xi,0,t),y(\xi,0,t),t)$. By applying the chain rule, we have the following

$$Y_t = \zeta_x + \zeta_t, \tag{B.42}$$

$$Y_\xi = \zeta_x X_\xi, \tag{B.43}$$

$$\Phi_t = \phi_t + \phi_x X_t + \phi_y Y_t, \tag{B.44}$$

$$\Phi_\xi = \phi_x X_\xi + \phi_y Y_\xi, \tag{B.45}$$

$$\Psi_\xi = \psi_x X_\xi + \psi_y Y_\xi = -\phi_y X_\xi + \phi_x Y_\xi, \tag{B.46}$$

where we have used the Cauchy-Riemann relation in the bottom equation. We substitute (B.42) and (B.43) into (3.48) and get

$$Y_t - \frac{Y_\xi}{X_\xi} X_t + \phi_x \frac{Y_\xi}{X_\xi} = \phi_y. \tag{B.47}$$

Multiplying (B.47) by X_ξ and using (B.46) gives

$$\Psi_\xi = X_t Y_\xi - Y_t X_\xi, \tag{B.48}$$

which is the time-dependent kinematic boundary condition in the mapped plane.

For the dynamic boundary condition, we first compute

$$\kappa = \frac{\zeta_{xx}}{(1 + \zeta_x^2)^{\frac{3}{2}}} = \frac{Y_{\xi\xi} X_\xi - X_{\xi\xi} Y_\xi}{J^{\frac{3}{2}}}. \tag{B.49}$$

where

$$J \equiv X_\xi^2 + Y_\xi^2. \tag{B.50}$$

By using the chain rule, we obtain

$$\kappa_{ss} = \frac{1}{\sqrt{1 + \eta_x^2}} \frac{\partial}{\partial x} \left(\frac{\kappa_x}{\sqrt{1 + \eta_x^2}} \right) = \frac{\kappa_{xx}}{1 + \eta_x^2} - \frac{\eta_x \eta_{xx} \kappa_x}{(1 + \eta_x^2)^2}, \tag{B.51}$$

After some algebra, the pressure exerted by the elastic sheet in (3.51) can be written as

$$M = \kappa_{ss} + \frac{1}{2} \kappa^3 = \frac{1}{2} \left[\frac{\kappa_{\xi\xi}}{J} + \left(\frac{\kappa_\xi}{J} \right)_\xi + \kappa^3 \right]. \tag{B.52}$$

The sum of squares of equation (B.45) and (B.46) gives

$$\Phi_\xi^2 + \Psi_\xi^2 = (\phi_x^2 + \phi_y^2) J. \tag{B.53}$$

$(B.45) \times X_\xi + (B.46) \times Y_\xi$ and $(B.45) \times Y_\xi - (B.46) \times X_\xi$ read

$$\phi_x = \frac{1}{J} (\Phi_\xi X_\xi + \Psi_\xi Y_\xi), \tag{B.54}$$

$$\phi_y = \frac{1}{J} (\Phi_\xi Y_\xi - \Psi_\xi X_\xi). \tag{B.55}$$

We substitute (B.44), (B.52)-(B.55) into (3.51) to get the time-dependent dynamic

boundary condition in the mapped plane

$$\Phi_t = -\frac{\Phi_\xi^2 + \Psi_\xi^2}{2J} - Y - M$$
$$+ \frac{\Phi_\xi}{J}(X_t X_\xi - Y_\xi X_{\xi\xi}) + \frac{\Phi_\xi}{J}(X_t X_\xi + Y_t Y_\xi) + \frac{\Psi_\xi}{J}(X_t Y_\xi - Y_t X_\xi). \quad \text{(B.56)}$$

Next we consider an analytic function z_t/z_ξ in $\xi + i\eta$ which can be written

$$\frac{z_t}{z_\xi} = \frac{x_t x_\xi + y_t y_\xi + i(y_t x_\xi - x_t y_\xi)}{x_\xi^2 + y_\xi^2}. \quad \text{(B.57)}$$

We denote $R(\xi, \eta, t)$, $G(\xi, \eta, t)$ by the real part and the imaginary part of z_t/z_ξ respectively. On the free-surface $\eta = 0$, (B.57) reads

$$R(\xi, 0, t) = \frac{Y_t Y_\xi + X_t X_\xi}{J}, \quad \text{(B.58)}$$

$$G(\xi, 0, t) = \frac{Y_t X_\xi - X_t Y_\xi}{J} = -\frac{\Psi_\xi}{J}, \quad \text{(B.59)}$$

where we have used (B.48) in the second equation above. Furthermore, $G(\xi, \eta, t)$ satisfies the Laplace equation. With the boundary condition at $\eta \to -\infty$, the harmonic boundary value problem for G is defined as the following

$$G_{\xi\xi} + G_{\eta\eta} = 0 \qquad\qquad \eta < 0, \quad \text{(B.60)}$$

$$G = -\frac{\Psi_\xi}{J} \qquad\qquad \eta = 0, \quad \text{(B.61)}$$

$$G_\eta \to 0 \qquad\qquad \eta \to -\infty. \quad \text{(B.62)}$$

After similar calculations using the Fourier transform, as we have seen before, we obtain the harmonic relation

$$R(\xi, 0, t) = \mathcal{H}[\frac{\Psi_\xi}{J}]. \quad \text{(B.63)}$$

From (B.58), (B.59) and (B.63), we derive the expressions for X_t and Y_t

$$X_t = \mathcal{H}[\frac{\Psi_\xi}{J}]X_\xi + (\frac{\Psi_\xi}{J})Y_\xi, \tag{B.64}$$

$$Y_t = \mathcal{H}[\frac{\Psi_\xi}{J}]Y_\xi - (\frac{\Psi_\xi}{J}). \tag{B.65}$$

Combining (B.25), (B.41), (B.48), (B.56), (B.64) and (B.65) gives the free-surface Euler system

$$X_\xi = 1 - \mathcal{H}[Y_\xi], \tag{B.66}$$

$$\Psi_\xi = \mathcal{H}[\Phi_\xi], \tag{B.67}$$

$$Y_t = \mathcal{H}[\frac{\Psi_\xi}{J}]Y_\xi - (\frac{\Psi_\xi}{J}), \tag{B.68}$$

$$\Phi_t = \frac{1}{2}\frac{\Phi_\xi^2 - \Psi_\xi^2}{J} - Y - M + \mathcal{H}[\frac{\Psi_\xi}{J}]\Phi_\xi. \tag{B.69}$$

Given the values of Φ and Y, we can compute X_ξ and Y_ξ using (B.66) and (B.67). Then the values of Y and Φ can be updated via the evolution equations (B.68) and (B.69) using a finite difference method such as the fourth-order Runge-Kutta. We are going to use this method to investigate numerically the instability of flexural-gravity waves. It can be achieved by considering a small perturbation to the steady waves which are used as the initial state of the time-dependent system.

Bibliography

[1] M. G. Blyth and J.-M. Vanden-Broeck. New solutions for capillary waves on fluid sheets. *Journal of Fluid Mechanics*, 507:255–264, 5 2004.

[2] F. Bonnefoy, M. H. Meylan and P. Ferrant. Nonlinear higher-order spectral solution for a two-dimensional moving load on ice. *Journal of Fluid Mechanics*, 621:215–242, 2009.

[3] A. R. Champneys, J.-M. Vanden-Broeck and G. J. Lord. Do true elevation gravity–capillary solitary waves exist? a numerical investigation. *Journal of Fluid Mechanics*, 454(1):403–417, 2002.

[4] B. Chen and P. G. Saffman. Numerical evidence for the existence of new types of gravity waves of permanent form on deep water. *Studies in Applied Mathematics*, 62:1–21, 1980.

[5] W. Choi and R. Camassa. Exact evolution equations for surface waves. *Journal of engineering mechanics*, 125(7):756–760, 1999.

[6] G. D. Crapper. An exact solution for progressive capillary waves of arbitrary amplitude. *Journal of Fluid Mechanics*, 2(06):532–540, 1957.

[7] D. G. Crowdy. Exact solutions for steady capillary waves on a fluid annulus. *Journal of nonlinear science*, 9(6):615–640, 1999.

[8] F. Dias. Capillary–gravity periodic and solitary waves. *Physics of Fluids*, 6(7):2239–2241, 1994.

[9] A. I. Dyachenko, E. A. Kuznetsov, M. D. Spector and V. E. Zakharov. Analytical

description of the free surface dynamics of an ideal fluid (canonical formalism and conformal mapping). *Physics Letters A*, 221(1):73–79, 1996.

[10] A. I. Dyachenko, V. E. Zakharov and E. A. Kuznetsov. Nonlinear dynamics of the free surface of an ideal fluid. *Plasma Physics Reports*, 22:829–840, 1996.

[11] L. K. Forbes. Surface waves of large amplitude beneath an elastic sheet. part 1. high-order series solution. *Journal of Fluid Mechanics*, 169:409–428, 7 1986.

[12] L. K. Forbes. Surface waves of large amplitude beneath an elastic sheet. part 2. galerkin solution. *Journal of Fluid Mechanics*, 188:491–508, 2 1988.

[13] T. Gao and J.-M. Vanden-Broeck. Numerical studies of two-dimensional hydroelastic periodic and generalised solitary waves. *Physics of Fluids*, 26(8):087101, 2014.

[14] T. Gao, Z. Wang and J.-M. Vanden-Broeck. Investigation of symmetry breaking in periodic gravity-capillary waves. *Journal of Fluid Mechanics*, 2016. submitted.

[15] T. Gao, Z. Wang and J.-M. Vanden-Broeck. New hydroelastic solitary waves in deep water and their dynamics. *Journal of Fluid Mechanics*, 788:469–491, 2 2016.

[16] T. Gao, Z. Wang and J.-M. Vanden-Broeck. On asymmetric generalised solitary gravity-capillary waves in finite depth. *Proceedings of the Royal Society A: Mathematical, Physical and Engineering Science*, 2016. submitted.

[17] A. G. Greenhill. Wave motion in hydrodynamics. *American Journal of Mathematics*, pages 62–96, 1886.

[18] P. Guyenne and E. I. Parau. Computations of fully nonlinear hydroelastic solitary waves on deep water. *Journal of Fluid Mechanics*, 713:307–329, 2012.

[19] P. Guyenne and E. I. Părău. Finite-depth effects on solitary waves in a floating ice sheet. *Journal of Fluids and Structures*, 49:242–262, 2014.

[20] J. K. Hunter and J. Scheurle. Existence of perturbed solitary wave solutions to a model equation for water waves. *Physica D: Nonlinear Phenomena*, 32(2):253–268, 1988.

[21] J. K. Hunter and J.-M. Vanden-Broeck. Solitary and periodic gravitycapillary waves of finite amplitude. *Journal of Fluid Mechanics*, 134(1):205–219, 1983.

[22] A. T. Ilichev. Solitary waves in media with dispersion and dissipation (a review). *Fluid dynamics*, 35(2):157–176, 2000.

[23] A. K. Jain. Review of flexible risers and articulated storage systems. *Ocean engineering*, 21(8):733–750, 1994.

[24] W. Kinnersley. Exact large amplitude capillary waves on sheets of fluid. *Journal of Fluid Mechanics*, 77(02):229–241, 1976.

[25] D. J. Korteweg and G. De Vries. Xli. on the change of form of long waves advancing in a rectangular canal, and on a new type of long stationary waves. *The London, Edinburgh, and Dublin Philosophical Magazine and Journal of Science*, 39(240):422–443, 1895.

[26] Y. A. Li, J. M. Hyman and W. Choi. A numerical study of the exact evolution equations for surface waves in water of finite depth. *Studies in Applied Mathematics*, 113(3):303–324, 2004.

[27] M. S. Longuet-Higgins. Capillary–gravity waves of solitary type on deep water. *Journal of Fluid Mechanics*, 200(1):451–470, 1989.

[28] J. R. Marko. Observations and analyses of an intense waves-in-ice event in the sea of okhotsk. *Journal of Geophysical Research: Oceans (1978–2012)*, 108(C9), 2003.

[29] P. A. Milewski, J.-M. Vanden-Broeck and Z. Wang. Dynamics of steep two-dimensional gravity–capillary solitary waves. *Journal of Fluid Mechanics*, 664:466–477, 2010.

[30] P. A. Milewski, J.-M. Vanden-Broeck and Z. Wang. Hydroelastic solitary waves in deep water. *Journal of Fluid Mechanics*, 679:628–640, 6 2011.

[31] P. A. Milewski and Z. Wang. Three dimensional flexural–gravity waves. *Studies in Applied Mathematics*, 131(2):135–148, 2013.

[32] H. Okamoto and M. Shōji. Nonexistence of bifurcation from crapper's pure capillary waves (mathematical analysis of phenomena in fluid and plasma dynamics). 1991.

[33] C. Page and E. I. Pǎrǎu. Hydraulic falls under a floating ice plate due to submerged obstructions. *Journal of Fluid Mechanics*, 745:208–222, 2014.

[34] E. I. Pǎrǎu and F. Dias. Nonlinear effects in the response of a floating ice plate to a moving load. *Journal of Fluid Mechanics*, 460(1):281–305, 2002.

[35] N. Peake. Nonlinear stability of a fluid-loaded elastic plate with mean flow. *Journal of Fluid Mechanics*, 434:101–118, 2001.

[36] P. I. Plotnikov and J. F. Toland. Modelling nonlinear hydroelastic waves. *Philosophical Transactions of the Royal Society A: Mathematical, Physical and Engineering Sciences*, 369(1947):2942–2956, 2011.

[37] L. Rayleigh. The form of standing waves on the surface of running water. *Proceedings of the London Mathematical Society*, 1(1):69–78, 1883.

[38] P. G. Saffman. The superharmonic instability of finite-amplitude water waves. *Journal of Fluid Mechanics*, 159:169–174, 1985.

[39] D. H. Sattinger. Bifurcation and symmetry breaking in applied mathematics. *Bulletin of the American Mathematical Society*, 3(2):779–819, 1980.

[40] C. Shimizu and M. Shōji. Appearance and disappearance of non-symmetric progressive capillary–gravity waves of deep water. *Japan journal of industrial and applied mathematics*, 29(2):331–353, 2012.

[41] V.A. Squire, R. J. Hosking, A. D. Kerr and P. J. Langhorne. Moving loads on ice plates (solid mechanics and its applications), 1996.

[42] V. A. Squire, W. H. Robinson, P. J. Langhorne and T. G. Haskell. Vehicles and aircraft on floating ice. 1988.

[43] G. G. Stokes. On the theory of oscillatory waves. *Trans Cambridge Philos Soc*, 8:441–473, 1847.

[44] T. Takizawa. Deflection of a floating sea ice sheet induced by a moving load. *Cold regions Science and Technology*, 11(2):171–180, 1985.

[45] J. F. Toland. Heavy hydroelastic travelling waves. *Proceedings of the Royal Society A: Mathematical, Physical and Engineering Science*, 463(2085):2371–2397, 2007.

[46] J. F. Toland. Steady periodic hydroelastic waves. *Archive for Rational Mechanics and Analysis*, 189(2):325–362, 2008.

[47] J.-M. Vanden-Broeck. Capillary waves with variable surface tension. *Zeitschrift für angewandte Mathematik und Physik ZAMP*, 47(5):799–808, 1996.

[48] J.-M. Vanden-Broeck. *Gravity-capillary free-surface flows.* Cambridge University Press, 2010.

[49] J.-M. Vanden-Broeck and F. Dias. Gravity-capillary solitary waves in water of infinite depth and related free-surface flows. *Journal of Fluid Mechanics*, 240:549–557, 6 1992.

[50] J.-M. Vanden-Broeck and J. B. Keller. A new family of capillary waves. *Journal of Fluid Mechanics*, 98(01):161–169, 1980.

[51] J.-M. Vanden-Broeck and E. I. Părău. Two-dimensional generalized solitary waves and periodic waves under an ice sheet. *Philosophical Transactions of the Royal Society A: Mathematical, Physical and Engineering Sciences*, 369(1947):2957–2972, 2011.

[52] Z. Wang. *Hydroelastic Analysis of High-Speed Ships.* Department of Naval Architecture and Offshore Engineering, Technical University of Denmark, 2000.

[53] Z. Wang, J.-M. Vanden-Broeck and P.A. Milewski. Asymmetric gravity–capillary solitary waves on deep water. *Journal of Fluid Mechanics*, 759:R2, 2014.

[54] Z. Wang, J.-M. Vanden-Broeck and P. A. Milewski. Two-dimensional flexural–gravity waves of finite amplitude in deep water. *IMA Journal of Applied Mathematics*, 78:750–761, 2013.

[55] J. T. Wilson. *Moving loads on floating ice sheets.* 1958.

[56] J. R. Wilton. On ripples. *The London, Edinburgh, and Dublin Philosophical Magazine and Journal of Science*, 29(173):688–700, 1915.

[57] V. E. Zakharov. Stability of periodic waves of finite amplitude on the surface of a deep fluid. *Journal of Applied Mechanics and Technical Physics*, 9(2):190–194, 1968.

[58] J. A. Zufiria. Non-symmetric gravity waves on water of infinite depth. *Journal of Fluid Mechanics*, 181:17–39, 1987.

[59] J. A. Zufiria. Weakly nonlinear non-symmetric gravity waves on water of finite depth. *Journal of Fluid Mechanics*, 180:371–385, 1987.